CI&CEQ

ISSN 1451 - 9372 (Print)
ISSN 2217 - 7434 (Online)
OCTOBER-DECEMBER 2025
Vol.31, Number 4, 249-339

Chemical Industry & Chemical Engineering Quarterly

SERBIA
Belgrade
AChE

The AChE Journal for Chemical Engineering,
Biochemical Engineering, Chemical Technology,
New Materials, Renewable Energy and Chemistry

www.ache.org.rs/ciceq

Journal of the
Association of Chemical Engineers of
Serbia, Belgrade, Serbia

Chemical Industry &
Chemical Engineering
CI&CEQuarterly

EDITOR-In-Chief

Vlada B. Veljković
Faculty of Technology, University of Niš, Leskovac, Serbia
E-mail: veljkovicvb@yahoo.com

ASSOCIATE EDITORS

Srđan Pejanović
Department of Chemical Engineering, Faculty of Technology and Metallurgy, University of Belgrade, Belgrade, Serbia

Dunja Sokolović
Faculty of Technical Sceinces, University of Novi Sad, Serbia

Ivona Radović
Faculty of Technology and Metallurgy, University of Belgrade, Serbia

EDITORIAL BOARD (Serbia)

Đorđe Janaćković, Ivanka Popović, Viktor Nedović, Goran Nikolić, Sanja Podunavac-Kuzmanović, Siniša Dodić, Zoran Todorović, Olivera Stamenković, Marija Tasić, Jelena Avramović, Jasna Canadanovic-Brunet, Ivana Karabegović

ADVISORY BOARD (International)

Dragomir Bukur
Texas A&M University, College Station, TX, USA

Milorad Dudukovic
Washington University, St. Luis, MO, USA

Jiri Hanika
Institute of Chemical Process Fundamentals, Academy of Sciences of the Czech Republic, Prague, Czech Republic

Maria Jose Cocero
University of Valladolid, Valladolid, Spain

Tajalli Keshavarz
University of Westminster, London, UK

Zeljko Knez
University of Maribor, Maribor, Slovenia

Igor Lacik
Polymer Institute of the Slovak Academy of Sciences, Bratislava, Slovakia

Denis Poncelet
ENITIAA, Nantes, France

Ljubisa Radovic
Pen State University, PA, USA

Peter Raspor
University of Ljubljana, Ljubljana, Slovenia

Constantinos Vayenas
University of Patras, Patras, Greece

Xenophon Verykios
University of Patras, Patras, Greece

Ronnie Willaert
Vrije Universiteit, Brussel, Belgium

Gordana Vunjak Novakovic
Columbia University, New York, USA

Dimitrios P. Tassios
National Technical University of Athens, Athens, Greece

Hui Liu
China University of Geosciences, Wuhan, China

FORMER EDITOR (2005-2007)

Professor Dejan Skala
University of Belgrade, Faculty of Technology and Metallurgy, Belgrade, Serbia

FORMER ASSOCIATE EDITORS

Milan Jakšić, *ICEHT/FORTH, University of Patras, Patras, Greece*
Jonjaua Ranogajec, *Faculty of Technology, University of Novi Sad, Novi Sad, Serbia*

Journal of the
Association of Chemical Engineers of
Serbia, Belgrade, Serbia

Chemical Industry &
Chemical Engineering
CI&CEQuarterly

Vol. 30 Belgrade, October-December 2024 No. 4

Chemical Industry & Chemical Engineering Quarterly (ISSN 1451-9372) is published quarterly by the Association of Chemical Engineers of Serbia, Kneza Miloša 9/I, 11000 Belgrade, Serbia

Editor:
Vlada B. Veljković
veljkovic@yahoo.com

Editorial Office:
Kneza Miloša 9/I, 11000 Belgrade, Serbia
Phone/Fax: +381 (0)11 3240 018
E-mail: shi@ache.org.rs
www.ache.org.rs

For publisher:
Ivana T. Drvenica

Secretary of the Editorial Office:
Slavica Desnica

Marketing and advertising:
AChE Marketing Office
Kneza Miloša 9/I, 11000 Belgrade, Serbia
Phone/Fax: +381 (0)11 3240 018

Publication of this Journal is supported by the Ministry of Education, Science and Technological Development of the Republic of Serbia

Subscription and advertisements make payable to the account of the Association of Chemical Engineers of Serbia, Belgrade, No. 205-2172-71, Komercijalna banka a.d., Beograd

Technical Editor:
Marija B. Tasić

Journal manager:
Aleksandar B. Dekanski

Printed by:
Faculty of Technology and Metallurgy, Research and Development Centre of Printing Technology, Karnegijeva 4, P.O. Box 3503, 11120 Belgrade, Serbia

Abstracting/Indexing:
Articles published in this Journal are indexed in *Thompson Reuters* products: *Science Citation Index - Expanded*™ - access *via Web of Science*®, part of *ISI Web of Knowledge*℠

CONTENTS

The activities of the Association of Chemical Engineers of Serbia are supported by:

MINISTRY OF SCIENCE,
TECHNOLOGICAL DEVELOPMENT
AND INNOVATION
OF REPUBLIC OF SERBIA

Faculty of Technology and
Metallurgy, University of Belgrade

Faculty of Science, University of Novi Sad

ITNMS
Institute for Technology of Nuclear
and Other Mineral Raw Materials,
Bekgrade

Faculty of Technology,
University of Novi Sad

Institute of Chemistry, Technology and Metallurgy,
University of Belgrade

Faculty of Technical Sciences
University of Novi Sad

Faculty of Technology,
University of Niš, Leskovac

Faculty of Technical Sciences,
University of Priština, Kosovska Mitrovica

IMS Institute, Belgrade

DCP HEMIGAL
Leskovac

Elixir Prahovo

CI&CEQ
Chemical Industry & Chemical Engineering Quarterly

Available online at
Association of the Chemical Engineers of Serbia *AChE*
www.ache.org.rs/CICEQ

Chem. Ind. Chem. Eng. Q. 31 (4) 249−256 (2025) CI&CEQ

SOYBEAN OIL PYROLYSIS IN A CONTINUOUS BENCH-SCALE REACTOR FOR LIGHT OLEFIN PRODUCTION

VINICYUS RODOLFO WIGGERS[1]

ROBSON GIL DE SOUZA RAMOS[1]

GABRIEL HENRIQUE WIENHAGE[1]

TUANNE GOMES PORTO[1]

ANTÓNIO ANDRÉ CHIVANGA BARROS[2]

LUANA MARCELE CHIARELLO[1]

[1]Department of Chemical Engineering, Regional University of Blumenau, Blumenau, SC, Brazil

[2]Instituto Superior Politecnico de Tecnologias e Ciencias, Luanda, Angola

Article Highlights

- Study of temperature's impact on light olefin production in continuous soybean oil pyrolysis
- The temperatures were varied from 500 to 600 °C in a constant feeding mass flow
- Ethene and propene formation are intensified with temperature
- The oxygen removal from the triglyceride also increases with temperature

Abstract

This study investigated the gas yield and its composition in different operation temperatures, giving special attention to light olefin production and oxygen content in soybean oil pyrolysis. The experiments were conducted in a continuous bench-scale reactor at steady state and isothermal conditions. Temperatures ranged from 500 to 600 °C with constant feeding mass flow. The resulting bio-oil exhibited high acid and iodine indices, as expected. Biogas samples were collected and submitted to gas chromatography to determine the chemical composition. The results revealed that ethene and propene formation are intensified with temperature, reaching more than 30% values in the gas phase. Additionally, higher temperatures led to increased oxygen removal from the triglyceride.

Keywords: cracking; ethene, propene; renewables; triglycerides; pyrolysis.

SCIENTIFIC PAPER

UDC 66.096.5:66.023:665.335.2

In 2019, the global energy matrix primarily consisted of non-renewable sources such as coal, oil, and natural gas, accounting for over 84% of the energy matrix [1]. By 2021, renewable energy sources reached a total of approximately 6.7% [2].

The increasing energy demand, driven by a new phase of economic growth, particularly in developing nations, has outstripped available energy resources. Consequently, biomass emerges as a promising renewable energy option, primarily due to its abundant supply of agricultural, industrial, and household waste [3]. In the search for sustainable energy sources, biomasses that are edible are frequently considered. This fact can lead to a food versus energy competition. However, this practice aligns with circular economy principles by closing the loop between consumption and production, minimizing the environmental footprint. Additionally, waste biomass, used cooking oils, and non-edible oils might create new markets for byproducts and reduce the dependence on petroleum advancing renewable sources goals without compromising food security [4].

Waste-to-energy technologies are frequently acknowledged as a viable solution for both energy production and waste management [5]. Notably, thermal conversion processes such as incineration [6], pyrolysis [7], and gasification [8] have gained

---

Correspondence: V.R. Wiggers, Department of Chemical Engineering, Regional University of Blumenau, Blumenau, SC, Brazil.
E-mail: vwiggers@furb.br

Paper received: 26 February, 2024
Paper revised: 20 September, 2024
Paper accepted: 23 October, 2024

https://doi.org/10.2298/CICEQ240226033W

prominence in this regard.

Thermal cracking, also known as pyrolysis, has emerged as one of the main potential processes to convert biomass into liquid fuels [9,10]. Thermal cracking involves the thermal degradation of biomass at high temperatures, ranging from 400 °C to 700 °C, in the absence of oxygen, with or without catalysts [11–13]. The pyrolysis of triacylglycerols involves breaking the carbon chains of animal or vegetable oils by increasing the system's temperature, resulting in solid, liquid, and gaseous phases [14]. The solid phase is basically coke with a high C/H ratio. By increasing the temperature, the reaction leads to the formation of low molecular weight organic products. These products are converted to CO_2, H_2, CO, CH_4, and C_2-C_4 hydrocarbons at high temperatures and increase gas production [15]. The organic liquid product, frequently called bio-oil, is composed mainly of hydrocarbons, which can be fractionated [16,17]. The yield and composition of the products obtained in the cracking process depend highly on the raw material [18] and operational conditions, especially the temperature-residence time combination. An elevated temperature with a long residence time will promote the formation of gaseous products, while a low temperature and a long residence time will favor coke formation. Finally, a moderate temperature with a short residence time will yield a higher liquid product [19].

The ongoing global economic growth indicates a substantial rise in demand for raw materials in the chemical industry, thereby requiring a rise in the production of basic petrochemicals derived from petroleum naphtha, particularly ethene, and propene, which are the most widely used olefins in industrial applications [20]. They serve as building blocks for petrochemical chains, serving as precursors for plastics, fibers, elastomers, solvents, paints, adhesives, and various other products widely utilized by society today [21,22].

It is estimated that 400 million tons of olefins are produced annually, using one billion tons of hydrocarbons as raw materials through processes such as Fluid Catalytic Cracking (FCC), steam cracking, and dehydrogenation, among others [23]. Among the compounds in the olefin group, ethene is one of the most significant importance to the industry. It is an unsaturated hydrocarbon comprising two carbon atoms bonded by a double bond. Due to the double bond between its carbons, it is a highly reactive compound that can participate in distinct reactions, converted into other compounds through halogenation, hydration, oxidation, alkylation, oligomerization, and polymerization reactions. It is the most important olefin in the petrochemical chain, with its leading derivatives including polyethylene, ethylene oxide, ethylene glycol, dichloroethane, ethylbenzene, and linear α-olefins, among others [2020].

Propene is an unsaturated hydrocarbon composed of three carbon atoms, with two of them bonded by a double bond. It can be obtained through various processes, mainly thermal cracking and FCC [24]. Propene is the second most important raw material in the petrochemical industry and serves as a building block for an entire production chain, generating various products such as polypropylene, acrylonitrile, propylene oxide, cumene, and acrylic acid, among others. It is primarily obtained from a non-renewable source, such as petrochemical naphtha [25].

In the literature, there are many works regarding the pyrolysis of triglycerides [18,26–30], and most of them focus on bio-oil yield and characterization. The gas phase has not received much attention regarding chemical composition, especially in C_2-C_4 identification and quantification, generally being grouped in lumps [31–33]. The main objective of this study is to evaluate the influence of temperature on the yield and composition of the gaseous fraction produced in the thermal cracking of refined soybean oil. Soybean oil was chosen as an abundant source of triglycerides around the world. This study becomes relevant due to the addition of experimental data on producing light olefins through the pyrolysis of soybean oil.

MATERIALS AND METHODS

Thermal cracking experiments

For the execution of thermal cracking experiments, a bench-scale reactor was used, operating in a continuous regime under steady-state and isothermal conditions [34,35]. The stainless-steel auger reactor has a positive displacement pump responsible for constant and continuous feeding to the reactor (Figure 1). The reactor consists of a cylindrical tube with internal thread, built-in stainless steel tubes measuring 955 mm in length and 25 mm in internal diameter, whose screw geometric dimensions can be seen in detail in [36]. The section comprises four control loops to maintain the reactor at a constant temperature. Each loop consists of 2 kW electric resistances. Before biomass feeding, water was passed through the reactor to produce steam and purge the oxygen. The feed contains only soybean oil, so during the processing only the feedstock is inside the reactor that works with pressure slightly above atmospheric pressure, avoiding the entrance of oxygen. After each experiment, water is passed again to purge the remaining biogas, followed by high-temperature airflow to burn the formed coke, as a reactor cleaning procedure.

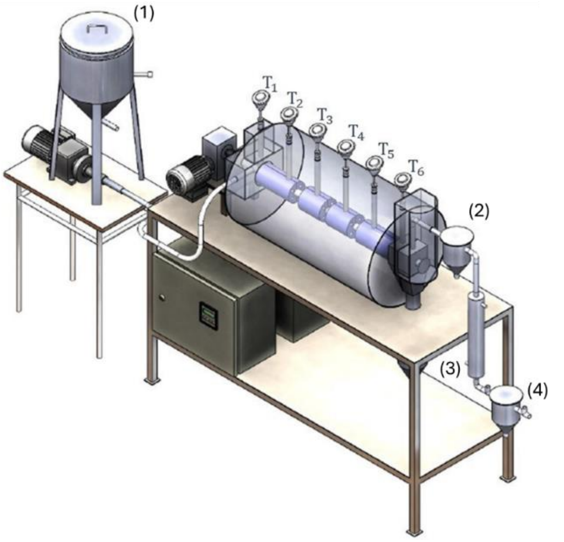

Figure 1. 3-D schematic view of the pyrolysis reactor. (1) - Feedstock reservoir; (2) - First bio-oil reservoir; (3) - Condenser; (4) - Second bio-oil reservoir.

Experimental runs were conducted at five different temperatures: 500, 525, 550, 575, and 600 °C, with a fixed mass flow rate of 300 g/h, in triplicate. The commercial refined soybean oil from the COAMO was obtained in 900 mL PET bottles from a local supplier and stored at room temperature (25 °C).

Soybean oil was fed to the thermal cracking reactor for one hour. Eq. (1) was used to calculate the average reactor temperature for each experiment.

$$\bar{T}_{reactor} = \frac{T_2 + T_3 + T_4 + T_5}{4} \qquad (1)$$

where $\bar{T}_{reactor}$ is the average temperature of the reactor and $\bar{T}_2$ to $\bar{T}_5$ are the average temperatures registered at thermocouples 2 to 5, respectively.

The volumetric flow of biogas generated during the reaction was measured to close the system's mass balance. A silicone hose connected to the reactor's outlet was inserted into a graduated inverted cylinder filled with water. The volumetric flow rate of the biogas was determined by measuring the time it took for the gas to displace the liquid in the cylinder. At least three samples of biogas were collected during the experiment using 60 mL syringes, which were connected to a 3-way valve and immediately taken for chromatographic analysis to determine the chemical composition. After each experiment, the mass of the produced bio-oil was measured, and physical-chemical analyses were carried out to characterize the obtained products.

Biogas composition

For the analysis of non-condensable gases, a Shimadzu® GC-17A gas chromatograph was used, equipped with a 60/80 Carboxen 1000 column (5 m x 2 mm stainless steel tubing). H_2, O_2, and N_2 were determined by thermal conductivity detection (TCD), while CH_4, C_2H_4, and C_2H_6 were detected using flame ionization detection (FID). CO and CO_2 were determined through methanation and FID, as described by Beims *et al.* [36].

For the analytical determination of C_3H_6, C_3H_8, C_4H_{10}, and C_4H_8, a gas chromatograph with FID detector, model 7890B from Agilent Technologies, was used, together with a capillary column, Stabilwax (30 m x 0.25 mm x 0.25 µm). The initial oven temperature was set at 28 °C (15 min) - 1 °C/min until 35 °C (2 min), followed by 30 °C/min until 100 °C (0 min), with a total run time of 32 min. The injector temperature was set at 250 °C, the helium gas flow rate at 2.2 mL/min, and the injection volume at 1 µL of the pure sample with a split ratio of 100:1.

Bio-oil characterization

Bio-oil collected in the reservoirs was analyzed regarding specific gravity, acid, and iodine indexes [37–39], and carbon number in the carbon chain. The methodology is described below.

Tests to determine the specific gravity were carried out in bio-oil samples produced in the reactor. The method is based on NBR-7148, being carried out at room temperature with the aid of a pycnometer, and calibrated volumetric glassware, to determine the relationship sample mass/volume. The Acid Index (AI) is defined as the amount (in mg) of potassium hydroxide required to neutralize one gram of the sample. The AI test was conducted to compare the acid content present in each bio-oil produced. The test for determining the acid index test was carried out according to the standards established by ASTM D 974/2008. A 2g sample was placed in a 125 mL Erlenmeyer flask, and 25 mL of solvent (isopropanol) was added. Two drops of phenolphthalein indicator were then added to this mixture, followed by titration with a potassium hydroxide solution (0.1 mol/L) until a pink color appeared. The acid index was calculated using the Eq. (2).

$$AI = (V_2 V_1) C_{KOH} 56,\ 1/m \qquad (2)$$

where IA is the acid number (mg KOH/g sample), V_2 is the volume spent in sample titration (ml), V_1 is the volume spent on blank titration (mL) and m is the mass of the sample (g).

Following EN14111, the Iodine Index (II) was used for samples of the raw material and bio-oil obtained from the reaction. The II is directly related to the degree of unsaturation in the sample, with a higher iodine index indicating a greater number of double bonds (unsaturations) present in the oil.

The methodology consists of adding between 0.13 and 0.15 g of the sample to a 500 mL Erlenmeyer flask containing 20 mL of solvent solution (cyclohexane and glacial acetic acid, 1:1). Then, 25 mL of Wijs solution (commercial) is added, the flask is sealed, and the mixture is left in a dark environment for 1 hour. The same procedure is performed for the blank sample. After the reaction time is complete, 20 mL of KI (100 g/L) and 150 mL of distilled water are added. Titration is then carried out with sodium thiosulfate until the endpoint (from pale yellow to transparent). Next, 2 mL of starch solution is added, and the titration is continued until the solution becomes fully transparent. The II can then be calculated using Eq. (3):

$$II = 12.69N\left(V_2V_1\right) \tag{3}$$

where *II* is the iodine index of the sample (g I2/100 g sample), *N* is the normality of the sodium thiosulfate, *V1* is the volume of the blank (mL), *V2* is the volume of the solution with the sample (mL), and *m* is the mass of the sample (g). The carbon number analysis was conducted on a Shimadzu® gas chromatograph (GC), model GC-2010 with AOC-5000 autoinjector and flame ionization detector (FID), the RTX-1 capillary column (30 m 0.32 mm x 3.00 µm) with helium gas flow of 1 mL/min. The initial heating of the oven was 50 °C and remained for 5 min. Afterward, a rate of 5 °C/min was applied up to 280 °C, remaining at this temperature for 12 min. The injector temperature was 250 °C, and the detector temperature was 280 °C. The split was 1:100.

The identification of carboxylic acid and ester compounds was carried out using gas chromatography coupled to mass spectrometry (GC-MS) on Shimadzu GC-MS equipment (QP 2010 Plus) with a capillary column with RTX-5 with AOC-20i automatic injector. In addition to the NIST 08 Spectro library, standards of n-alkanes and fatty acid methyl esters (FAME) were injected to compare and identify compounds. The oven temperature was programmed to 50 °C (2 min), heating at 5 °C/min until 280 °C (12 min). Helium was used as carrier gas with a constant 1 mL/min flow. The injector temperature was 250 °C, and the injection volume was 0.2 µL (pure sample) with a split ratio of 1:200.

Mass balance of cracking products

The liquid and gas fraction yields were calculated according to the equations already reported by Beims et al. [26,36]. The coke fraction is calculated by balance, the difference between the gas and liquid fractions. The coke on the reactor walls is removed during the cleaning process after each experimental run. The cleaning process involves feeding air into the heated reactor, promoting controlled burning. Eqs (4–7) were used to calculate the fractions of bio-oil, biogas, and coke.

$$m_{SO} = m_{BO} + m_{BG} + m_{coke} \tag{4}$$

$$X_{BO} = \frac{m_{BO}}{m_{SO}} \tag{5}$$

$$X_{BG} = \frac{m_{BG}}{m_{SO}} \tag{6}$$

$$X_{coke} = 1 - X_{BO} - X_{BG} \tag{7}$$

where X_{BO}, X_{BG}, and X_{coke} are, respectively, the mass fractions of bio-oil, biogas, and coke, respectively.

RESULTS AND DISCUSSION

Pyrolysis experiments of refined soybean oil were carried out with a material feed ($\dot{m}_{SO}$), varying between 301 and 315 g/h. The operating time was fixed at 1 hour and the temperature ($\bar{T}_{reactor}$) varied between 500 and 600 °C. As the reaction temperature increases, there is a reduction in the yield of liquid fractions. This fact can be explained by the tendency of fragmentation of the initial molecule, leading to the formation of compounds with smaller molecular chains and, consequently, a higher gaseous fraction. Table 1 presents the actual resulting operational conditions, the mass yields of crude bio-oil ($\dot{m}_{BO}$) produced, and the volumetric flow of non-condensable gases ($\dot{V}_{BG}$) obtained during the experiments. It demonstrates that the conversion of soybean oil into non-condensable gases increases as the reaction temperature advances. At the same time, in the opposite direction, there is a reduction in the yield of the liquid fraction. The results showed that the highest amount of bio-oil produced (224 g/h) was obtained at T-500, while the highest flow of non-condensable gases (147.6 L/h) was achieved at T-600. On the other hand, the experiment carried out at T-600 showed a lower bio-oil yield (99.2 g/h) compared to the experiment at T-500. Likewise, the lowest flow of non-condensable gases (39.7 L/h) was recorded in the experiment at T-500.

The results of the physicochemical analyses of bio-oil are shown in Table 2. The reaction temperature influenced the increase in the acidity index of the produced bio-oil, indicating the presence of fatty acids (saturated and unsaturated) and short-chain carboxylic acids in the final product. The high acidity can be explained by breaking C-C bonds rather than

Table 1. Experimental data on the thermal cracking of refined soybean oil.

Run[1]	$\bar{T}_{reactor}$ [2] (°C)	$\dot{m}_{SO}$ [3] (g/h)	$\dot{m}_{BO}$ [4] (g/h)	$\dot{V}_{BG}$ [5] (L/h)	$\overline{MM}$[6] (g/mol)	ρ_{BG} [7] (g/L)	$\dot{m}_{BG}$ [8] (g/h)	x_{BG} [9] (%)	x_{BO} [10] (%)	x_{coke} [11] (%)
T-500	$501.8^{\pm6.7}$	$303.4^{\pm1.6}$	$224.0^{\pm7.0}$	$39.7^{\pm3.6}$	$32.0^{\pm2.1}$	$1.3^{\pm0.1}$	$52.0^{\pm5.8}$	$17.1^{\pm1.8}$	$73.8^{\pm2.6}$	$9.1^{\pm2.3}$
T-525	$527.6^{\pm3.7}$	$303.2^{\pm0.9}$	$207.7^{\pm7.5}$	$49.2^{\pm5.7}$	$29.9^{\pm0.9}$	$1.2^{\pm0.0}$	$60.2^{\pm7.9}$	$19.9^{\pm2.7}$	$68.5^{\pm2.6}$	$11.6^{\pm4.8}$
T-550	$551.2^{\pm3.1}$	$301.0^{\pm0.8}$	$190.9^{\pm9.1}$	$67.7^{\pm3.8}$	$28.9^{\pm0.3}$	$1.2^{\pm0.0}$	$80.1^{\pm5.3}$	$26.6^{\pm1.7}$	$63.4^{\pm3.1}$	$10.0^{\pm1.4}$
T-575	$575.1^{\pm1.8}$	$309.3^{\pm4.5}$	$151.5^{\pm9.8}$	$108.2^{\pm6.2}$	$27.6^{\pm1.5}$	$1.1^{\pm0.1}$	$121.9^{\pm1.2}$	$39.4^{\pm0.3}$	$49.0^{\pm3.7}$	$11.6^{\pm4.0}$
T-600	$602.0^{\pm2.5}$	$315.1^{\pm3.2}$	$99.2^{\pm18.8}$	$147.6^{\pm4.4}$	$25.7^{\pm1.0}$	$1.1^{\pm0.0}$	$155.3^{\pm10.4}$	$49.3^{\pm2.8}$	$31.5^{\pm5.6}$	$19.3^{\pm8.4}$

[1]Experiment run; [2]Average reactor temperature; [3]Soybean oil mass flow rate; [4]Bio-oil mass flow rate; [5]Biogas volumetric flow; [6]Average molecular mass of bio-oil; [7]Specific mass of biogas; [8]Biogas mass flow; [9]Composition of the biogas fraction; [10]Composition of the bio-oil fraction; [11]Coke fraction composition.

decarbonylation and decarboxylation reactions. The values for the iodine index represent the number of unsaturated compounds, indicating a high concentration of olefins, typical in cracking processes.

Table 2. Results of the physicochemical analyses of the acidity index (IA), iodine index (II), and specific mass (ρ_{BO}) of the crude bio-oil samples.

Run	IA (mg KOH/g)	II (g I_2/100 g)	$\rho_{BO}^{22^oC}$(kg/m³)
T-500	$101.9^{\pm2.4}$	$184.9^{\pm16.2}$	$895.4^{\pm3.7}$
T-525	$120.8^{\pm5.6}$	$213.2^{\pm43.6}$	$896.3^{\pm8.4}$
T-550	$127.5^{\pm9.7}$	$249.7^{\pm71.8}$	$894.8^{\pm3.7}$
T-575	$123.6^{\pm8.9}$	$341.1^{\pm3.6}$	$891.6^{\pm3.9}$
T-600	$120.9^{\pm5.5}$	$310.3^{\pm30.6}$	$902.2^{\pm8.9}$

Figure 2 presents the compound distribution of bio-oils according to the carbon number in the chain. High temperatures lead to a higher concentration of lighter compounds, while lower temperatures result in a bio-oil with heavier ones. Figure 3 presents the GC-MS chromatograms for bio-oils obtained and the fatty acid identification. The peak intensity of identified fatty acids (palmitic, eicosanoic, stearic, oleic, and linoleic acids) reduces with temperature due to the advance of decarbonylation and decarboxylation reactions resulting in oxygen removal. The comparison with an n-alkanes standard sample shows that bio-oils have a wide range distribution of compounds according to the chain length. Furthermore, the acidity and the presence of olefins in high concentrations in the bio-oil produced indicates that it requires further treatment before being used as a source of fuels and chemicals.

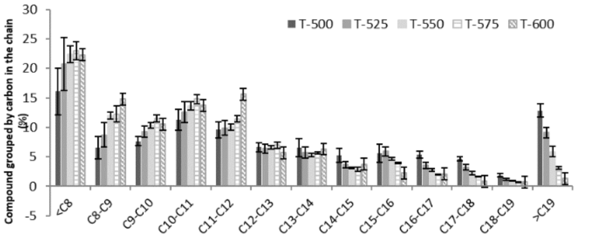

Figure 2. Distribution of compounds in bio-oils according to carbon number.

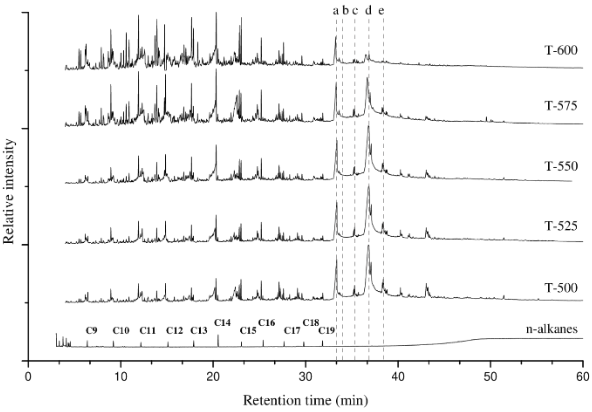

Figure 3. GC-MS profiles for n-alkane standard and bio-oil samples at T-500, T-525, T-550, T-575 and T-600. Peaks: (a) palmitic acid, (b) eicosanoic acid, (c) stearic acid, (d) oleic acid and (e) linoleic acid.

Table 1 also shows the influence of the reaction temperature on the products' yield, showing a tendency towards a reduction in the production of bio-oil and an increase in the flow of non-condensable gases with the increase in temperature. During cracking experiments, gaseous samples collected were submitted to chromatography to determine the molar and mass composition, presented in Table 2. With these data, the average molecular mass and density (ρ) of the bio-gas were determined, and was possible to quantify the mass yield of bio-gas and close the mass balance of the experiments, which data are also presented in Table 1. The average molecular weight decreases, and bio-gas yield increases with temperature. Also, it is possible to note that coke and gas have a significant yield at T-600. The presence of CO and CO_2 confirms the oxygen removal during pyrolysis. The hydrogen concentrations on a mass basis are not relevant. Ethene and propene concentrations are significant.

When analyzing the gaseous phase product, a significant variation in the concentrations of some components was observed with the increase in the reaction temperature. Methane (CH_4), ethene (C_2H_4), propene (C_3H_6), and hydrogen (H_2) increased in concentration with reaction temperature. Ethane (C_2H_6), carbon monoxide (CO), and carbon dioxide (CO_2) showed a reverse trend because of the increased concentration of light hydrocarbons resulting from more intensive cracking. As presented by Asikin-Mijan *et al.* [40], CO and CO_2 are formed by decarbonylation and decarboxylation reactions, respectively. The formation

Table 3. Molar (m) and mass (w) composition of non-condensable gases (%).

Run	CO	CH_4	CO_2	C_2H_4	C_2H_6	C_3H_6	H_2	Others*
	(m/w)	(m/w)	(m/w)	(m/w)	(m/w)	(m/w)	(m/w)	
T-500	$25.5^{\pm5.7}/22.5^{\pm5.9}$	$9.0^{\pm2.2}/4.6^{\pm1.4}$	$14.2^{\pm1.0}/19.7^{\pm2.1}$	$22.9^{\pm2.0}/20.2^{\pm2.9}$	$11.1^{\pm0.7}/10.5^{\pm1.3}$	$6.6^{\pm6.2}/8.9^{\pm8.3}$	$2.4^{\pm0.4}/0.1^{\pm0.1}$	$8.2^{\pm10.5}/12.8^{\pm15.7}$
T-525	$23.1^{\pm1.1}/21.7^{\pm1.6}$	$12.0^{\pm0.9}/6.4^{\pm0.7}$	$10.7^{\pm0.1}/15.8^{\pm0.6}$	$29.3^{\pm1.0}/27.5^{\pm1.6}$	$12.8^{\pm0.7}/12.9^{\pm0.5}$	$6.9^{\pm1.8}/9.7^{\pm2.6}$	$1.8^{\pm0.4}/0.1^{\pm0.0}$	$3.4^{\pm3.8}/5.9^{\pm6.2}$
T-550	$20.6^{\pm1.7}/19.9^{\pm1.8}$	$14.5^{\pm0.4}/8.0^{\pm0.2}$	$9.1^{\pm0.5}/12.6^{\pm1.5}$	$31.8^{\pm0.4}/30.9^{\pm0.4}$	$12.9^{\pm0.5}/13.4^{\pm0.6}$	$7.9^{\pm1.1}/11.5^{\pm1.6}$	$2.0^{\pm0.2}/0.1^{\pm0.0}$	$1.3^{\pm1.4}/1.7^{\pm1.6}$
T-575	$20.5^{\pm0.4}/20.8^{\pm0.8}$	$15.4^{\pm1.0}/8.9^{\pm0.2}$	$8.3^{\pm0.1}/13.3^{\pm0.8}$	$31.7^{\pm1.9}/32.2^{\pm0.4}$	$9.5^{\pm0.7}/10.3^{\pm0.3}$	$8.7^{\pm1.6}/13.1^{\pm1.8}$	$5.5^{\pm5.5}/0.4^{\pm0.4}$	$0.5^{\pm0.1}/0.9^{\pm0.3}$
T-600	$18.4^{\pm1.2}/20.1^{\pm2.0}$	$15.4^{\pm1.1}/9.6^{\pm0.4}$	$7.5^{\pm0.4}/12.8^{\pm1.1}$	$29.7^{\pm1.9}/32.4^{\pm1.0}$	$8.6^{\pm0.6}/10.1^{\pm0.5}$	$8.2^{\pm1.9}/13.4^{\pm2.7}$	$11.9^{\pm3.5}/0.9^{\pm0.3}$	$0.4^{\pm0.1}/0.8^{\pm0.2}$

* C_3H_8, C_4H_8, and C_4H_{10} were not detected in biogas at different temperatures.

of CO and CO_2 results in the release of the radicals R and R’, which undergo several subsequent reactions to form hydrocarbons in the C1-C5 range. The variation in the concentration of the mentioned components with the reaction temperature suggests that the high temperature favors the formation of large amounts of methane. On the other hand, the opposite trend exhibited by ethane indicates that hydrogen transfer reactions such as hydrogenation are more favorable at low temperatures. The elimination of hydrocarbon radicals and the dehydrogenation reactions for forming ethene from ethane or ethyl radicals may be favored at high temperatures. These results agree with the study performed by Idem et al. [41] and suggest that temperature is an important factor influencing the chemical reactions involved in the thermal cracking of soybean oil. With the molar composition of the bio-gas, it is possible to estimate its molecular weight and quantify its mass produced.

Table 4 brings the calculated mass flow of CO and CO_2, the calculated mass flow of oxygen, and its percentual removal according to the feeding mass flow of soybean oil. The mass flow of CO and CO_2 continues to increase with temperature as a result of deoxygenation reactions occurrence. However, the intensity of cracking also increases with temperature and leads to an improvement in light hydrocarbon formation resulting in a decrease in the concentration of CO and CO_2 in the gas phase.

It was also observed that the oxygen removal reactions continue to occur with temperature, reaching a value of ~10% at T-600. Since soybean oil has oxygen content varying in the range of 10–13% [42], pyrolysis can achieve high oxygen removal values at elevated temperatures.

Table 4. Mass flow of CO $(\dot{m}_{CO})$, CO2 $(\dot{m}_{CO_2})$, the calculated mass flow of oxygen in biogas $(\dot{m}_{O-BG})$ and its percentual ratio related to the feeding mass flow $(\dot{m}_{SO})$.

Run	$\dot{m}_{CO}$ (g/h)	$\dot{m}_{CO_2}$ (g/h)	$\dot{m}_{O-BG}$ (g/h)	$\dot{m}_{SO}$ (g/h)	$\frac{\dot{m}_{O-BG}}{\dot{m}_{SO}}$ (%)
T-500	$11.3^{\pm1.1}$	$10.4^{\pm0.3}$	$14,0^{\pm0,9}$	$303.4^{\pm1.6}$	4,6
T-525	$13.0^{\pm1.7}$	$9.5^{\pm1.0}$	$14,3^{\pm1,7}$	$303.2^{\pm0.9}$	4,7
T-550	$15.9^{\pm0.4}$	$11.1^{\pm1.2}$	$17,1^{\pm1,1}$	$301.0^{\pm0.8}$	5,7
T-575	$25.3^{\pm0.9}$	$16.2^{\pm1.0}$	$26,3^{\pm1,3}$	$309.3^{\pm4.5}$	8,4
T-600	$31.1^{\pm1.1}$	$19.8^{\pm0.7}$	$32,2^{\pm1,2}$	$315.1^{\pm3.2}$	10,2

CONCLUSION

The investigation shows that the composition of the gas phase must be carefully determined once the overall mass balance depends on it. The analyses confirm that operational conditions, especially temperature, directly influence ethene and propene yields in the gas phase. At a temperature of 600 ºC, biogas production approaches nearly 50%, with more than 30% of ethene on a mass basis. Additionally, the oxygen removal in the form of CO and CO_2 increases with temperature, reaching high levels of oxygen removal.

ACKNOWLEDGEMENTS

The authors are grateful to the Regional University of Blumenau (FURB) and the Instituto Superior Politecnico de Tecnologias e Ciencias. This work was supported by the Foundation for Research Support and Innovation of Santa Catarina State (FAPESC) and the Conselho Nacional de Desenvolvimento Científico e Tecnológico (CNPq no 302903/2023-2). This study was financed in part by the Coordenação de Aperfeiçoamento de Pessoal de Nível Superior e Brasil (CAPES) Finance Code 001.

REFERENCES

[1] M. Heydari, A. Heydari, M. Amini, Int. J. Eng. Appl. Sci. 9 (2023) 167–173. https://ssrn.com/abstract=4515903.

[2] O.O. Yolcan, Innov. Green Dev. 2 (2023) 100070. https://doi.org/10.1016/j.igd.2023.100070.

[3] T. Li, J. Wang, H. Chen, W. Li, P. Pan, L. Wu, G. Xu, H. Chen, Energy Convers. Manage. 287 (2023) 117085. https://doi.org/10.1016/j.enconman.2023.117085.

[4] J. Tomei, R. Helliwell, Food versus fuel. Going beyond biofuels. Land Use Policy, 56 (2016). http://dx.doi.org/10.1016/j.landusepol.2015.11.015.

[5] T.C. Floriani, L.M. Chiarello, T.G. Porto, V.R. Wiggers, J. Solid Waste Technol. Manage. 48 (2022) 270–279. https://doi.org/10.5276/JSWTM/2022.270.

[6] B.E. Piske, F. Lopes, J. Utzig, V.R. Wiggers, Renewable Energy Power Qual. J. 21 (2023) 154–159. https://doi.org/10.24084/repqj21.255.

[7] L. Chiarello, T. Porto, A. Barros, E. Simionatto, V. Botton, V. Wiggers, Angolan Miner. Oil Gas J. 1 (2020) 1–5.

https://doi.org/10.47444/amogj.v1i1.1.

[8] T.G. Porto, W.O. Tavares, F. Lopes, D. Vênancio, G.H. Wienhage, L.M. Chiarello, V.R. Wiggers, Angolan Miner. Oil Gas J. 2 (2021) 28–31. https://doi.org/10.47444/amogj.v2i2.5.

[9] Y. Shirazi, S. Viamajala, S. Varanasi, Appl. Energy 179 (2016) 755–764. https://doi.org/10.1016/j.apenergy.2016.07.025.

[10] D.G. Lima, V.C.D. Soares, E.B. Ribeiro, D.A. Carvalho, É.C.V. Cardoso, F.C. Rassi, K.C. Mundim, J.C. Rubim, P.A.Z. Suarez, J. Anal. Appl. Pyrolysis, 71, 987, 2004. https://doi.org/10.1016/j.jaap.2003.12.008.

[11] L.M. Chiarello, T.G. Porto, G.H. Wienhage, V. Botton, V.R. Wiggers, in Handbook of Biomass Valorization for Industrial Applications, Shahid-ul-Islam, A.H. Shalla, S.A. Khan Eds., Wiley (2022) p. 107–128. https://doi.org/10.1002/9781119818816.ch6.

[12] S. Czernik, V Bridgwater, Energy Fuels 18 (2004) 590–598. https://doi.org/10.1021/ef034067u.

[13] G. Menshhein, V. Costa, L. M. Chiarello, D.R. Scharf, E.L. Simionato, V. Botton, H.F. Meier, V.R. Wiggers, L. Ender, Renewable Energy 142 (2019) 561–568. https://doi.org/10.1016/j.renene.2019.04.136.

[14] V.R. Wiggers, R.F. Beims, L. Ender, E.L. Simionatto, H.F. Meier, in Frontiers in Bioenergy and Biofuels, E. Jacob-Lopes, L.Q. Zepka Eds., InTech Open (2017) p. 524. http://doi.org/10.5772/65498.

[15] X. Hu, M. Gholizadeh, J. Energy Chem. 39 (2019) 109–143. https://doi.org/10.1016/j.jechem.2019.01.024.

[16] T. Stedile, R.F. Beims, L. Ender, D.R. Scharf, E.L. Simionatto, H.F. Meier, V.R. Wiggers, Brazilian J. Chem. Eng. 36 (2019) 573–585. https://doi.org/10.1590/0104-6632.20190361s20170466.

[17] G. Menshhein, V. Costa, L.M. Chiarello, D.R. Scharf, E.L. Simionato, V. Botton, H.F. Meier, V.R. Wiggers, L. Ender, Data Brief 25 (2019) 104325. https://doi.org/10.1016/j.dib.2019.104325.

[18] T. Stedile, L. Ender, H.F. Meier, E.L. Simionatto, V.R. Wiggers, Renewable Sustainable Energy Rev. 50 (2015) 92–108. https://doi.org/10.1016/j.rser.2015.04.080.

[19] A. V. Bridgwater, Chem. Eng. J. 91 (2003) 87–102. https://doi.org/10.1016/S1385-8947(02)00142-0.

[20] L. Zhang, R. Gao, L. Wang, C. Zhang, K. Jun, S. K. Kim, T. Zhao, H. Wan, G. Guan, Chem. Eng. J. 471 (2023) 1–14. https://doi.org/10.1016/j.cej.2023.144611.

[21] M. Felischak, T. Wolff, L. Alvarado Perea, A. Seidel-Morgenstern, C. Hamel, Chem. Eng. Sci. 210 (2019) 1–9. https://doi.org/10.1016/j.ces.2019.115246.

[22] S. Wang, L. Zhang, P. Wang, X. Liu, Y. Chen, Z. Qin, M. Dong, J. Wang, L. He, U. Olsbye, W. Fan, Chem 8 (2022) 1376–1394. https://doi.org/10.1016/j.chempr.2022.01.004.

[23] V. Zacharopoulou, A. Lemonidou, Catalysts 8 (2017) 1–19. https://doi.org/10.3390/catal8010002.

[24] A. Payne, G. Garcia-Garcia, P. Styring, Green Chem. 25 (2023) 4029–4057. https://doi.org/10.1039/D2GC04721G.

[25] V. Zacharopoulou, A.A. Lemonidou, Mater. Today Proc. 5 (2018) 27511–27516. https://doi.org/10.1016/j.matpr.2018.09.070.

[26] R.F. Beims, V. Botton, L. Ender, D.R. Scharf, E.L. Simionato, H.F. Meier, W.R. Wiggers, Fuel 217 (2018) 175–184. https://doi.org/10.1016/j.fuel.2017.12.109.

[27] A. Goldbach, H. Meier, V. Wiggers, L. Chiarello, A. Barros, Chem. Ind. Chem. Eng. Q. 28 (2022) 1–8. https://doi.org/10.2298/CICEQ200810010G.

[28] M.A. Mohamed, Int. J. Res. Appl. Sci. Eng. Technol. (2017) 2971–2976. https://doi.org/10.22214/ijraset.2017.11410.

[29] E.S. Ramos, D. Zimmermann, R.F. Beims, L.M. Chiarello, V. Botton, E.L. Simionato, V.R. Wiggers, Environ. Prog. Sustainable Energy 39 (2020) 1–6. https://doi.org/10.1002/ep.13441.

[30] T. Kraiem, A.B. Hassen, H. Belayouni, M. Jeguirim, Sci. Pollut. Res., 24, 9951, 2017. https://doi.org/10.1007/s11356-016-7704-z.

[31] B. Periyasamy, Fuel, 158, 479, 2015. https://doi.org/10.1016/j.fuel.2015.05.066.

[32] C. Rabbat, S. Awad, A. Villot, Y. Andres, Waste Biomass Valorization 14 (2023) 2061–2083. https://doi.org/10.1007/s12649-022-01989-2.

[33] V. Botton, D.R. Scharf, E.L. Simionato, V.R. Wiggers, L. Ender, H.F. Meier, A.A. Chivanga Barros, Quim. Nova 35 (2012) 677–682. https://doi.org/10.1590/S0100-40422012000400004.

[34] M. Konig, L.M. Chiarello, L. Curbani, V. Botton, V.R. Wiggers, L. Ender, Ind. Crops Prod. 201 (2023) 1—7. https://doi.org/10.1016/j.indcrop.2023.116931.

[35] R.F. Beims, V. Botton, L. Ender, D.R. Scharf, E.L. Simionato, H.F. Meier, W.R. Wiggers, Data Brief 17 (2018) 442–451. https://doi.org/10.1016/j.dib.2018.01.054.

[36] M.J. Suota, E.L. Simionatto, D.R. Scharf, H.F. Meier, V.R. Wiggers, Energy Fuels 33 (2019) 9886–9894. https://doi.org/10.1021/acs.energyfuels.9b01971.

[37] G. H. Wienhage, E. S. Ramos, L. M. Chiarello, V. Botton, V. R. Wiggers, Angolan Miner. Oil Gas J. 2 (2021) 21–27. https://doi.org/10.47444/amogj.v2i2.4.

[38] A.S. Matheus, A.P.S. Francisco, P. Francisco, N. Manuela, A.A.C. Barros, Chem. Eng. Technol. 45 (2022) 1835–1841. https://doi.org/10.1002/ceat.202200171.

[39] N. Asikin-Mijan, H. V. Lee, J. C. Juan, A. R. Noorsaadahb, Y. H. Taufiq-Yap, RSC Advances. 7 (2017) 46445–46460. https://doi.org/10.1039/c7ra08061a.

[40] R.O. Idem, S.P.R. Katikaneni, N.N. Bakhshi, Energy Fuels 10 (1996) 1150–1162. https://doi.org/10.1016/S0140-6701(97)82785-3.

[41] F. Yu, L. Gao, W. Wang, G. Zhang, J. Ji, J. Anal. Appl. Pyrolysis 104 (2013) 325–329. https://doi.org/10.1016/j.jaap.2013.06.017.

VINICYUS RODOLFO WIGGERS[1]
ROBSON GIL DE SOUZA RAMOS[1]
GABRIEL HENRIQUE WIENHAGE[1]
TUANNE GOMES PORTO[1]
ANTÓNIO ANDRÉ CHIVANGA BARROS[2]
LUANA MARCELE CHIARELLO[1]

[1]Department of Chemical Engineering, Regional University of Blumenau, Blumenau, SC, Brazil

[2]Instituto Superior Politecnico de Tecnologias e Ciencias, Luanda, Angola

NAUČNI RAD

PIROLIZA SOJINOG ULJA U KONTINUALNOM LABORATORIJSKOM REAKTORU ZA DOBIJANJE LAKIH OLEFINA

U ovoj studiji je istraživan prinos gasa i njegov sastav pri različitim radnim temperaturama. Posebna pažnja posvećena je proizvodnji lakih olefina i sadržaju kiseonika pirolizom sojinog ulja. Eksperimenti su sprovedeni u kontinualnom laboratorijskom reaktoru u stacionarnim i izotermnim uslovima. Temperature su se kretale od 500 do 600 °C sa konstantnim protokom mase. Dobijeno bio-ulje je pokazalo visoke kiselinske i jodne brojeve, kao što se i očekivalo. Uzorci biogasa su sakupljeni i podvrgnuti gasnoj hromatografiji radi određivanja hemijskog sastava. Rezultati su otkrili da se formiranje etena i propena intenzivira sa temperaturom, dostižući više od 30% vrednosti u gasnoj fazi. Pored toga, više temperature su dovele do povećanog uklanjanja kiseonika iz triglicerida.

Ključne reči: krekovanje; eten; propen; obnovljivi izvori energije; trigliceridi; piroliza.

CI&CEQ
Chemical Industry & Chemical Engineering Quarterly

Available online at
Association of the Chemical Engineers of Serbia *AChE*
www.ache.org.rs/CICEQ

Chem. Ind. Chem. Eng. Q. 31 (4) 257–276 (2025) CI&CEQ

ADVANCEMENTS IN PHYTOMASS-DERIVED ACTIVATED CARBON FOR APPLICATIONS IN ENERGY STORAGE SYSTEMS

KALYANI PALANICHAMY[1]
BANUPRABHA THAKKU RANGACHARI[2]
SRIDHAR JAYAVEL[3]
ARAVIND DHANDAPANI[4]
VARAGUNAPANDIYAN NATARAJAN[5]

[1]Department of Chemistry, DDE, Madurai Kamaraj University, Madurai, Tamil Nadu, India
[2]Department of Chemistry, Mary Matha College of Arts and Science, Periyakulam, Tamil Nadu, India
[3]Department of Biotechnology, DDE, Madurai Kamaraj University, Madurai, Tamil Nadu, India
[4]University Science Instrumentation Centre, Madurai Kamaraj University, Madurai, Tamil Nadu, India
[5]Department of Chemical Engineering, King Khalid University, Abha, Saudi Arabia

REVIEW PAPER

UDC 661.183.2:544:662.63

Article Highlights

- Covers the cost-effective methods for the production of activated carbon from agricultural wastes
- Highlights the market potentials of phytomass-derived activated carbon in the energy sector
- Methods to enhance the performance of PAC electrodes on supercapacitors are featured
- Discussed the need for a sustainable bioeconomy

Abstract

Phytomass i.e. plant biomass-derived active carbon is a versatile electrode material for energy devices owing to its natural and ubiquitous abundance, variety, ecocentrism, and unique physical properties. This article intricately reviews the recent advancements in phytomass-derived activated carbon (PAC), chiefly for the supercapacitor electrodes and notably, phytomass including different parts of the plants limited to, stem, leaf, flower, seed, fruit, and root for deriving PACs bestowed with excellent electrochemical performance have been considered. Advancement in the preparation of activated from phytomass, important facts associated with synthesis, and physical and electrochemical attributes have also been elaborated, which is expected to furnish a fruitful direction towards advocating supercapacitors – the green energy packs. The surface of PAC is usually decorated with organic functional moieties containing heteroatoms like O, and/or S/N (referred to as self-doped heteroatoms). The synergy of these heteroatoms in enhancing the pseudocapacitance of the PAC electrodes in supercapacitors has also been featured. Further, the review provokes insights on strategies, prominent challenges, prospects, imminent opportunities, and hopeful trends in support of AC from various plant parts that may power our energy-based society, and scientific industries and in establishing a sustainable energy sector as well by harnessing nature's potential.

Keywords: activated carbon; phytomass; heteroatoms; supercapacitors; self-doped heteroatoms; circular bioeconomy.

The thinning of the ozone layer, the rise in global temperatures, and the depletion of natural resources apparently lead to significant environmental challenges to the highest degree and pose severe threats to societal safety issues. In our current landscape, we witness a confluence of rapid wealth and energy expansion amidst the alarming rise in pollution levels, culminating in the decline of both public health and environmental well-being. The escalation in the utilization of fossil fuels and natural resources during industrial and post-industrial advancements might be the underlying cause for the aforementioned issues. Hence, we have been attempting hard to find substitute

---

Correspondence: S. Jayavel, Department of Biotechnology, DDE, Madurai Kamaraj University, Madurai-625021, Tamil Nadu, India.
E-mail: jsridharbiotech@mkuniversity.ac.in
Paper received: 26 May, 2024
Paper revised: 6 September, 2024
Paper accepted: 7 November, 2024

https://doi.org/10.2298/CICEQ240526034P

green avenues for generating less-polluting energy and accordingly, many research institutions have come together to promote renewable, green, and clean energy technologies for replacing conventional energy resources. One alternative approach to address the exponentially growing demand for wealth and energy alongside increasing pollution and its detrimental effects on public and environmental health is the paradigm transition towards a "sustainable and circular bio-economy". A circular bio-economy is sustainably designed to minimize waste, make the most of existing resources, and reduce environmental impacts. Thus, the hunt for eco-friendly and low-cost materials is becoming more evident for example, through the use of renewable resources.

In the array of alternative energy sources, biomass has evolved into an essential and integral component of ecosystems. As a result, biomass assumes a crucial role as a renewable energy source [1], holding substantial promise for the generation of biofuels used in transportation, electricity, and heating applications [2]. The significance of green energies and a closer focal point on biomass will be an instrument for future energy security and sustainable development based on circular bio-economy. With the recent scientific discoveries and inventions exploiting this inexpensive, abundant, and natural biomass, promising technologies have been developed and are proposed to be capable of generation of electricity, heat, and bio-based liquid fuels. Speaking of biomass, by definition, it refers to a blend of naturally occurring substances sourced from plants like shrubs, trees, algae, and crops, encompassing all materials with an organic matrix, excluding plastics and similar products derived from petrochemicals and fossil materials [3]. The most important categories of the sources of biomass are [4]: residues from agriculture and forestry, residues from animals, algal biomass, crops grown in aquatic environments, municipal solid waste (excluding metals and plastics) and residues from waste streams (excluding metals and plastics).

According to reports, the global biomass reserves for land and aquatic ecosystems are estimated at approximately 1.8 trillion tons and 4 billion tons, respectively. The total biomass in the world, particularly in the energy viewpoint has a prospective production capability of 33,000 EJ; corresponding to more than 80 times the annual energy utilization in the world [5]. So, biomass has attracted many researchers to use it as an alternative energy resource.

Nevertheless, as we witness in the modern age of renewable and sustainable energy, the quest for green alternatives to conventional power sources is more pressing than ever. As the world grapples with environmental challenges and seeks to reduce its carbon footprint, innovative technologies are emerging. One such technology revolves around supercapacitors, devices with the potential to revolutionize energy storage. These supercapacitors, often seen as the missing link in the transition to clean energy, rely on advanced materials. One promising avenue involves harnessing the potential of phytomass-derived activated carbon (PAC), a natural resource that presents a sustainable and environmentally friendly solution. Hence, the present review on PAC for supercapacitor applications is motivated by several unique aspects of the plants used and their potential contributions to energy storage technologies, as mentioned below.

Novelty of materials: The paper highlights the use of underutilized plant materials as sources of activated carbon (AC). These materials are not traditionally recognized for their potential in energy applications, making the study significant in exploring new biomass resources.

Sustainability: The focus on phytomass aligns with the growing interest in sustainable energy solutions. Utilizing waste plant materials for AC production supports a circular bioeconomy, reducing reliance on fossil fuels and synthetic materials.

Performance Metrics: The review can emphasize the electrochemical performance of many PACs, which demonstrated impressive capacitance values. This performance showcases the viability of these materials for supercapacitor applications.

Suggest potential improvements, such as scaling up production, enhancing surface functionality, or combining with other materials to create hybrid supercapacitors.

Environmental Impact: By promoting the use of waste phytomass, the research contributes to environmentally friendly practices in energy storage. The synthesis processes are typically less energy-intensive and do not involve harsh chemicals, making them more sustainable compared to conventional carbon sources.

Uniqueness of plants with reference to supercapacitors

Chemical composition: The unique chemical makeup of the selected plants contributes to the formation of AC with desirable properties. The presence of lignin and cellulose in these plants enhances the structural integrity and porosity of the resulting carbon.

Morphological characteristics: The natural morphology of the leaves aids in creating a hierarchical porous structure during activation, which is crucial for maximizing surface area and improving ion transport in supercapacitors.

Abundance, accessibility, and sustainable future: Plants are widely available, which means their use as carbon sources can help in waste reduction and provide a low-cost alternative for AC production.

Thus, the review aims to communicate the innovative use of phytomass for AC production, highlighting its sustainability, performance, and the unique characteristics of the plants involved. This can drive further research and innovation in the field of supercapacitors, promoting the development of eco-friendly energy storage solutions and its role in advancing the green energy agenda.

Having put forth the context of biomass-based energy sources, the authors of this comprehensive review have organized the current knowledge on the topic for the convenience of readers interested in energy matters under the following sub-topics: applications of carbon, classification of biomass, biomass as a sustainable source for AC, preparation of AC from biomass waste materials, key factors for enhancing capacitance with plant-derived materials, impact of physical characteristics of plants derived ACs on the key metrics of the supercapacitors, state-of-the-art and prospects of PAC as electrode materials in supercapacitors, state-of-the-art and prospects of PAC as electrode materials in supercapacitors, impact of self-doped heteroatoms on the specific capacitance/pseudo capacitance of biomass-based AC, summary, perspectives, and future challenges and future outlook on the plant-based AC materials for future energy storage devices.

This review encompasses the latest insights and findings from open literature over 15 years, offering an in-depth exploration of the significance and promising prospects associated with PAC as a sustainable and effective material for supercapacitor electrodes. Turning to the focal point of the present review article, it is interesting to note that the abundance of phytomass resources and the environmentally-friendly activation processes make it an attractive alternative to conventional carbon sources in diverse fields, and simultaneously, their unique porous structure and high surface area offer excellent charge storage capabilities, paving the way for advanced energy storage solutions. Thus, waste phytomass should be viewed as unmapped zero-cost capital of essential environmental services and not as garbage at all.

Applications of carbon

Carbon materials have been playing key roles for human beings: for instance, since the pre-historical age, charcoal has been used as a source of heat and as adsorbent/scavenger, as soot in black ink, natural graphite powder as pencil leads, graphite electrodes for many electrical based devices and chemical production, for the development of communication techniques, carbon blacks for reinforcing tires, conductive carbon rods/inks/powders and carbon blacks for supporting the improvement of primary batteries, thin graphite flakes in membrane switches for making control panels and computers, an admixture of graphite and fluorine has been used for enhancing the performance of primary batteries.

Classification of biomass

Biomass can be categorized based on its diversity, quantity, and compositional characteristics, depending on the intended purpose and scope only, as there are no theoretical and practical ways of classifying the same. Also, according to the origin, function, and final products, generally biomass is categorized into two groups: (1) based on the ecological classifications or the specific vegetation types present in nature and (2) based on the use and purpose of biomass (e.g., as feedstock and derived carbon). Category (1) is the most adopted classification, which consequently splits biomass as: woody biomass and timber resources, herbaceous plant biomass, biomass derived from aquatic ecosystems, biomass from animal and human waste sources, mixtures of various biomass components. Classification of biomass into groups, varieties, and species is given in Table 1 [6].

Table 1. Classification of biomass.

S. No.	Biomass group	Varieties and species
1.	Wood and woody biomass	Angiospermous or gymnospermous; coniferous or deciduous; stems, lumps, pellets, branches, foliage, bark, chips, briquettes, sawdust, and others from various wood species.
2.	Herbaceous biomass	Grasses and flowers (alfalfa, arundo, bamboo, banana, brassica, cane, cynara, miscanthus, switchgrass, timothy, others); straws (barley, bean, flax, corn, mint, oat, rape, rice, rye, sesame, sunflower, wheat, others); other residues (fruits, shells, husks, hulls, pits, pips, grains, seeds, coir, stalks, cobs, kernels, bagasse, food, fodder, pulps, cakes, etc.).
3.	Aquatic biomass	Macroalgae (blue, green, blue-green, brown, red) or microalgae; seaweed, kelp, lake weed, water hyacinth, marine or freshwater algae etc.
4.	Animal and human waste biomass	Bones, meat-bone meal; various manures, etc.
5.	Biomass Mixtures	Several substrates belonging to different classes, mentioned above, present in mixed forms.

Biomass as a renewable source for AC

Presently, biomass is the major energy resource in the globe (the role of biomass is about 70%) which provides the world's overall energy and energy in just beginning countries demand [7]. Subsequently, abundant agricultural discards/wastes/refuse would also be generated. As such these wastes might have no trade and industry value and would only present discarding problems. Burning of biomass wastes contributes tremendously to environmental pollution, and thus leads to polluted air, water, and land. This process also releases large amounts of CO_2 (together with dust particles) into the atmosphere, the main contributor to global warming. But alternative and astute thinking has offered a scientific solution to consume these secondary, inexpensive, and renewable sources for conversion into a valued-added product namely AC for countless applications. Hence, harnessing these cost-free waste materials is anticipated to be an efficient process, wherein their transformation into AC not only adds economic value but also aids in cutting waste disposal expenses. Significantly, this approach offers a potentially economical and environmentally friendly substitute for the current high-cost commercial AC powders. It is noteworthy that the utilization of biomass wastes as raw material (precursor) for AC production has witnessed an uptick in recent years, driven by the aforementioned considerations regarding AC. The selection of biomass resources for carbon production is guided by their cost, availability and their potential to be renewed into extremely porous carbon powders through carbonization for diverse and appealing applications.

Various types of biomass materials are being used as preparatory materials in producing AC powders. It is interesting to note that the chemical composition of biomass includes cellulose, hemicellulose (includes galactans, mannans, xylans, and arabinogalactans), lignin, starch (includes amylopectin and amylase), minor organic components, inorganic matters, fluid matters and elements such as Ca, Mg, K, Na, N, Cl, S and P [8], which may sometimes be present in a highly modified form in the surface of the AC produced.

The agricultural by-products consist of the main extent of cellulose and hemicellulose, while the rest includes ash, lignin, and nitrogenous compounds [9] and these residues can be an excellent source of energy.AC are much cheaper than metal oxides and conducting polymers for Science and Industrial applications and they have much larger specific surface area than the others. In recent times, there has been a growing fascination with the fabrication and manipulation of diverse nanostructured carbon materials, particularly for potential applications like supercapacitors. Presently, cellulose materials sourced from forestry, agricultural, and agro-industrial residues are gaining attention due to their ready availability and rich content. These cellulose-based wastes accumulate in significant quantities annually, typically managed through environmentally harmful methods such as burning or landfill disposal. However, transforming them into high-value products like AC is increasingly regarded as the preferable and environmentally conscious alternative.

Plants having more than 50% lignin contents are good precursors of porous carbon while cellulose and hemicelluloses release carbon monoxide, carbon dioxide, and water upon carbonization and form micropores. These micropores are very important in the performance of electrodes. Many researchers have used different precursors, such as fruit-derived materials, tree-derived materials, and other biomass-derived materials, to manufacture biomass-based porous carbon materials.

Generally, the pore size distribution, connectivity, and hydrophilicity determine the capacitance of the porous carbon materials, since they play a vital role in influencing the energy density and ion diffusion process of the active materials [10].

The manufacture of AC out of waste materials exemplifies the extraction of high-value products from inexpensive sources, concurrently addressing the issue of waste disposal [11]. Consequently, there is a significant emphasis on developing processes for the recycling of these waste materials. These carbon-rich wastes serve as excellent raw materials for AC production. This category of waste encompasses a diverse range of materials, including switch grass, poplar trees, sugarcane bagasse, sawdust, brewer's spent grains, stems, husks, leaves, stalks, shells, and peels from cereals such as corn, wheat, rice, sorghum, and barley, among others, as we saw in Table 1.

Preparation of AC from biomass waste materials

Carbon activation can be accomplished through three methods, namely: physical activation [12], chemical activation [12], and steam pyrolysis/activation [13]. A bird's eye view of the various activation methodologies has been provided below.

Physical activation

Physical or thermal activation stands out as a widely employed technique for generating ACs from biomass precursors. This process can be manifested either as a single-step or a dual-step procedure [14]. However, the prevalent approach involves a dual-step sequence wherein the carbonization of dried samples occurs at temperatures ranging from 400 to 700 °C, resulting in the formation of biochar. Subsequently, activation takes place using oxidizing gases such as air, steam, CO_2, or their combinations [15], conducted at elevated temperatures of approximately 800–1100 °C to facilitate burn-off. The biochar derived from carbonization typically exhibits a surface area of less than 300 m^2/g [16]. This limited adsorption capacity and surface area are attributed to the pores obstructed by tarry substances, necessitating their removal through activation with oxidizing gases.

In the single-step approach, carbonization and activation take place simultaneously at a temperature maintained within the range of 600–800°C [17]. Comparable to the double-stage method, this single-stage process involves carbonizing the dry sample up to a particular temperature, after which the biochar can be further heated for a preferred duration simply by switching from inert gas to oxidizing gas. Despite sharing similarities with the dual-stage process, the single-step technique proves to be more practical as it eliminates the need for a cooling phase post-carbonization, leading to reduced physical effort, lower electrical utilization, cost savings, and a shorter working time [16]. Physical activation, integral to this process, not only widens the thin pores on the surface of the biochar but also generates new pores simultaneously, thereby enhancing the porosity and surface area of the carbonaceous porous structure. However, it is worth noting that physical activation may yield a comparatively lower carbon output and lower quality of AC compared to what chemical activation (described below) could offer, mainly due to the superior activation temperature and comprehensive activation time involved in the procedure [14].

In the realm of physical activation, commonly employed activating agents include steam and CO_2. Air (oxygen), on the other hand, is less favored as an activation agent due to the exothermic character of the reactions involved, potentially leading to excessive burning on both the internal and external surfaces of the biochar, thereby resulting in reduced yield [18]. Both steam and CO_2 exhibit similar maximum BET surface areas, capable of reacting with carbon to generate surface areas that can attain up to 1000 m^2/g or even higher. Despite their procedural similarities, the mechanisms and reactions involved in steam and CO_2 activation differ slightly. Notably, at temperatures next to activation, steam is expected to react four times faster with carbon than CO_2 [16]. Consequently, steam activation allows AC to attain a high surface area within a relatively short period.

Activation using CO_2 creates further new pores rather than the expansion of existing narrow pores, whereas steam activation prioritizes the widening of micropores from the onset of the activation process, eventually developing mesopores and macropores. This strategy ensures a more extensive and diverse distribution of pores in the resulting ACs [19]. The physical activation of cellulosic materials typically yields microporous AC. Even at an accelerated activation rate, steam activation tends to yield a higher percentage of mesoporous and microporous structures, while CO_2 activation favors higher microporosity. The preference for CO_2 activation stems from its cleanliness, ease of gas handling, and the ability to control the activation procedure still at high temperatures up to 800 °C due to its gradual reaction rate [20]. Various raw materials, including rice husk, rice straw, corn cob, corn hulls, peanut hulls, pecan shells, coconut shells, and almond shells have been used as raw materials to produce AC materials by physical activation method [21,22].

Chemical activation

In the single-stage approach, carbonization is omitted, and the dried sample undergoes activation as its primary step, involving interaction with dehydrating agents such as NaOH, KOH, $ZnCl_2$, and H_3PO_4 [23]. Conversely, the dual-stage process involves the carbonization of the dried sample to produce biochar within the temperature range of 400 - 600 °C before the subsequent chemical activation [14]. The three forms of chemical activations are [24], namely: basic activation, acidic activation, neutral activation.

In chemical activation, the precursor i. e. the dried phytomass sample is mixed with definite amounts of active agents such as KOH, NaOH, H_2SO_4, HNO_3, H_3PO_4, $ZnCl_2$, $CaCl_2$, Na_2SO_4, and K_2CO_3 [25]. The activating agent functions as a dehydrating agent, preventing the formation of tar and excluding volatile substances in the process. This dual action serves to augment the yield of ACs and lowers the carbonization temperature in comparison to the physical activation method [26].

Chemical activation primarily serves to increase the diameter of fine pores and generate new pores, thereby enhancing the adsorptive capability of the carbonized product [27]. In contrast to physical activation, chemical activation boasts various advantages, including a lower conversion temperature, shorter activation time, higher carbon yield, and greater specific surface area and porosity. Utilizing activating agents such as phosphoric acid facilitates the formation of both micro and mesopores in the resultant carbon structure. The mesopore fraction in the AC is predominantly influenced by the production conditions and the biopolymer composition of the cellulosic material.

Steam pyrolysis/activation

There is also an alternative one-step treatment method, referred to as steam-pyrolysis according to the findings of Fan *et al.* [28]. In this process, the raw sample is either heated at moderate temperatures (500–700 °C) in the presence of pure steam or heated at 700–800 °C under the influence of regular steam. The samples undergo heating at a rate of 10 °C/min until reaching a final temperature of 700 °C, 750 °C, or 800 °C, where they are held for 1 or 2 hours in the continuous flow of steam [29]. The resulting ACs may exhibit a high pore volume, and their activation burn-off or mass loss due to the activation process is determined [13].

Key factors for enhancing capacitance with plant-derived materials

For preparing AC, the most advantageous parts of the plant are typically the stems, barks, and leaves. This is due high carbon content in stems and leaves. This is crucial because performance is closely related to its high carbon content, high surface area, and porous structure. These aspects can help in achieving the high surface area needed for effective charge storage in supercapacitors. Further, stems and leaves are more readily available and easier to process. They also tend to have a more uniform structure, which can result in more consistent activation and higher-quality carbon [30,31].

Furthermore, certain specific structures in phytomass-derived carbons are expected to enhance the capacitance suitable for advanced supercapacitor applications. The features, though not exhaustive, are specified below.

Hierarchical porous structure and surface area. Porous carbon materials derived from plants with a hierarchical structure containing micropores, mesopores, and macropores have been extensively studied for supercapacitor electrodes [32]. The interconnected porous framework provides a high surface area for electrolyte ion adsorption and short ion diffusion paths, leading to high capacitance [33].

Nitrogen doping. Increasing the nitrogen content in plant-derived porous carbons is key to improving their supercapacitor performance [33]. Nitrogen doping introduces pseudocapacitance and enhances wettability and conductivity [32]. Bamboo shoot-derived carbons with 3.0 at % N showed a high capacitance of 412 F/g [33].

Biomass precursor selection. The choice of plant biomass precursor affects the properties of the phytomass-derived carbon. For instance, bark-based carbons exhibit a unique flower-like 3D vertical nanosheet structure with excellent electronic transport and high surface area [34]. Daylily flower-derived AC also showed promising electrochemical behavior [35].

3D nanostructured carbons from seaweed. Seaweed-based 3D nanostructured carbons exhibit high surface area, conductivity, and pseudocapacitance [36].

Activation methods. Chemical activation methods like KOH treatment can significantly increase the surface area and porosity of plant-derived carbons. To cite, *Broussonetia papyrifera* stem bark activated with KOH had a BET surface area of up to 1212 m^2/g and a pore size of 3.8 nm, leading to a capacitance of 320 F/g [32].

It is also important to understand that in addition to the above factors, adequate water supply during the plant growth phase is essential for optimal plant health in general. It is also understood that water stress can lead to stunted growth and reduced biomass quality and quantity, which negatively impacts the properties of the carbon produced by these plants. Hence, the growth environments that enhance capacitance in supercapacitors involve a combination of optimal soil conditions, environmental factors, appropriate plant species, effective post-growth treatments, and sufficient water availability. Thus, it is important to consider these elements collectively that contribute to the development of high-performance carbon materials suitable for supercapacitor applications. So, selecting appropriate plant precursors and optimizing the activation process can produce high-performance ACs for advanced energy storage applications.

Impact of physical characteristics of plants derived ACs on the key metrics of the supercapacitors

Physical properties like the specific surface area, pore size, and pore volume distribution of AC derived from plants significantly impact the key metrics of supercapacitor performance [37] as follows:

Specific surface area (SSA). High SSA (>2000 m^2/g) enhances capacitance (C), energy density (E) and power density (P). Low SSA (<1000 m^2/g) may limit performance.

Pore size distribution. Micro-pores (<2 nm). enhance electrochemical double-layer capacitance (EDLC) and increase energy density (E). Meso-pores (2–50 nm) facilitate ion transport and diffusion and improve power density (P). Macro-pores (>50 nm) enhance electrolyte accessibility and wetting, and increase capacitance (C).

Pore volume distribution. High pore volume (>0.5 cm^3/g) enhances capacitance (C) and energy density (E).

The factors mentioned below influence key metrics of the supercapacitors: capacitance (C) directly related to SSA and pore volume; energy density (E) influenced by SSA, pore size, and pore volume; power density (P) affected by pore size, pore volume, and conductivity; cycling stability influenced by pore structure, surface functionality, and conductivity; electrolyte accessibility impacted by pore size, pore volume, and surface wettability.

By tailoring the specific surface area, pore size, and pore volume distribution of plant-derived AC, we can optimize supercapacitor performance for specific applications.

Key characteristics: high lignin content enhances thermal stability and surface area; low ash content reduces impurities and improves conductivity; well-developed pore structure increases surface area and ion transport, high carbon content improves conductivity and electrochemical performance; oxygen-containing functional groups enhances pseudocapacitance and wettability.

Several reviews on plant-based ACs are available in the literature and one such review involves the narration of ultrahigh-specific surface area porous carbon materials, mesoporous carbon materials, hierarchical porous carbon materials, and phytomass, plant biomass-derived active carbon materials are the most common types of carbon materials from diverse types of plants and they can be prepared by using different methods [38]. Preparation methods are: pyrolysis (thermal decomposition in the absence of oxygen to produce AC), chemical activation (treatment with chemicals like KOH, NaOH, or H_3PO_4 to enhance surface area and porosity); physical activation (treatment with steam or CO_2 to develop pore structure and surface area). By selecting the right plant part and preparation method, we can produce high-performance AC for supercapacitors. This understanding can lead to the development of new plant biomass-derived materials with enhanced performance, increased adoption in commercial supercapacitors, integration with other energy storage technologies (e.g., batteries), scalable and cost-effective production methods, expanded applications in fields like electronics, transportation, and renewable energy systems.

The present review paper thus aims to further refine our understanding of the value and potential of plant biomass-derived AC for supercapacitor applications, thereby driving further research and innovation in this field.

State-of-the-art and prospects of PACas electrode materials in supercapacitors

The progress in electrochemical energy storage gadgets from usual, green, and costless materials coupled with large electrochemical performance is the actual, valid, and demanding vision of the energy advocates in the present scenario of the energy crisis of late. In favor of these perspectives, carbon-based materials viz: ACs, carbon aerogels, graphene, carbon nanotubes and carbon nanofibers, carbon-metal oxide composites and other classes of materials such as polymer composites and hybrid metal oxide-conductive polymer materials have been proposed as electrode materials for energy storage gadgets such as supercapacitors, lithium-ion batteries, etc.

The ultimate electrochemical performance and output of supercapacitors is an interplay between several criteria such as the type/nature of the electrolyte used, physicochemical features of the electrode material, hardware, or configuration of the cell assembly. Of these, the commercial success of supercapacitors depends on the electrode materials and hence plays a prime role in serving as a vital ingredient in energy storage devices in general, since the electrochemical capability of the cell is very much prejudiced by the surface features of the electrode substance like large mesopores, high surface area, etc. [39].

Recent high-performing supercapacitors use porous ACs as electrodes and one of the best resources for generating AC powders and that too in large mass are the renewables or plant biomass (phytomass) wastes. So, any inexpensive phytomass with high carbon content, low inorganics, and ash may serve as raw materials for the production of ACs [40].

As we saw, carbon materials such as ACs, carbon aerogels, graphites, carbon nanofibers, carbon nanotubes, and metal oxide-carbon composites have actively been investigated for the use of electrode materials for energy storage devices. The selection of electrode materials is mainly done based on their working temperature range, accessibility, non-toxicity, high chemical stability, and easy processability. Out of many investigated, ACs are widely used because of their variable pore structure, large surface area, and variety of precursors available for their production along with reduced CO_2 emissions. The important goal will be obviously to increase the amount of energy and power with stable electrochemical performance. Simultaneously, carbon materials with desirable, structural, morphological, chemical, and electrochemical features would be the likely choice of electrodes. Hence carbon, which has been obtained by simple pyrolysis of phytomass precursors might have a huge prospective in many applications and devices.

Moreover, phytomass wastes are comparatively cheaper for obtaining AC powders and hence are viewed as a viable raw precursor for the synthesis of ACs resulting in electrochemical performance and good cycling efficiency in supercapacitors. Considering the versatility of the phytomass materials, the final products of thermal processing or pyrolysis or activation viz., phytomass carbon or phytochar, are among the electrode materials well suited for energy devices.

Thus, effectually and eventually perceiving the importance and value of PAC, diverse research groups are devoting time and funds for impeccable research to the valuable application of the same as electrode potentials in electrochemical energy systems like supercapacitors and LIBs. While numerous raw materials have been investigated for AC preparation in previous studies, researchers continue to seek out novel materials based on their availability and suitability for producing AC specifically designed for capacitor applications.

Thus, in this review paper, as already stated, detailed literature on the various categories of PACs applied as electrode materials in capacitors/supercapacitors are discussed that may cater to the needs of our society, scientific industries, and sustainable energy sector as well as harnessing nature's potential. Interesting reports on the above subject have been consolidated, which would provide us with the background and details about the electrochemical execution of phytomass-derived carbon potentials.

It is well established that the pore size distribution of PAC highly depends upon the plant parts used [41] and AC with more structural, textural (micropores, mesopores, or macropores) and chemical properties as precursors have excellent electrochemical features [42]. Nevertheless, in the present review article, noteworthy recent literature available on plant biomass, i.e., PAC, which includes different parts of the plants such as stems, leaves, flowers, seeds, fruits, and roots are considered and under the following titles, we discuss these categories of phytomass for deriving active carbon with excellent performance. Further, the important facts related to the synthesis methods and physical and electrochemical features of PACs are elaborated in the following sub-sections.

Phytomass carbon from stems (straw)

Stems or straw are the middle portion of a plant that transmits organic matter during photosynthesis and also incorporates water/salts from roots. Hence the ion content is larger in straw/stem. To make straw/stem AC, carbonizing at elevated temperatures has been commonly applied [43,44].

By simple KOH activation, tobacco stem-based ACs (TS-ACs) were prepared. Their use as electrodes in EDLC was evaluated by Xia *et al* [43]. The surface area of the derived ACs differs over a wide range i.e. between 1472.8 and 3326.7 m^2/g. While the ratio of tobacco stem to KOH is improved, the mesoporosity has been reported to be enhanced significantly. In 1 M $LiPF_6$-DEC/DMC/EC electrolyte solution, a high specific capacitance value of 190 F/g at 1 mA/cm^2 was found. Through this work, the novel use of TS as an important energy storage material has been identified.

Sudhan *et al.* [44] have detailed the production of AC from rice straw using a simple and straightforward process involving carbonization followed by chemical activation. Employing KOH as the chemical activator resulted in the creation of disordered micro and mesopores on the carbon, yielding a high specific surface area of approximately 1007 m^2/g, as established by N_2 adsorption-desorption and TEM analysis indicated the formation of ultra-fine carbon nanoparticles around 5 nm in size because of chemical activation and carbonization. A remarkable specific capacitance of 332 F/g in the three-electrode aqueous electrolyte was exhibited, with a specific capacitance retention of 99% after 5000 cycles. Furthermore, a symmetric supercapacitor device fabricated from the AC displayed a high specific capacitance of 156 F/g and a notable energy density of 7.8 Wh/kg in 1M H_2SO_4. The use of 1-ethyl-3-methyl imidazolium tetrafluoroborate [EMIM][BF_4] ionic liquids resulted in a cell voltage of 2.5 V in the symmetric device, accompanied by a specific capacitance of 80 F/g and an impressive energy density of 17.4 Wh/kg. In a non-aqueous electrolyte, the charged device powered a red LED for more than 5 minutes after a 20-second charging period.

Xueliang *et al* [45] have prepared AC from wheat straw by activating with KOH which resulted in honeycomb-like structures and explored the same for EDLC performance. The capacitance value was 251 F/g in the methyltriethylammonium tetrafluoroborate/acetonitrile electrolyte system. In the report, the authors converse the relations between surface area, scan rate, pore diameter, and specific capacitance. Tian *et al* [46] have reported AC with flute-type micropores (FTMAC) prepared from the cotton stalk using KOH as an activating agent. TEM images at different magnifications are shown in Fig. 1. A controlled pore structure with a high specific surface area of 1964 m^2/g and a pore volume of 1.03m^3/g is exhibited. The FTMAC-based electrode was observed to deliver a high specific capacitance of 254 F/g in 1M

H_2SO_4 electrolyte at a current density of 0.2 A/g. Also, featuring 221 F/g at a current density of 10 A/g, showing a good rate capacity with 87% retention and capacitance retention of 96% at a current density of 1 A/g, representing long cyclic stability even after 10000 charging and discharging cycles.

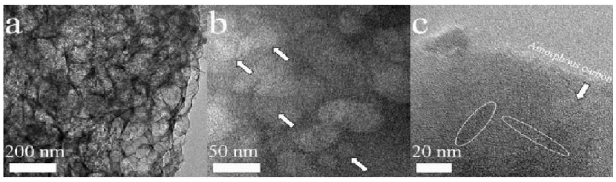

Figure 1. TEM of the sample at various magnifications [46].

Wang *et al* [47] utilized cornstalk to create porous carbon sheets under ambient air atmosphere. These carbon sheets exhibit an extremely thin structure, approximately 4.6 nm thick, facilitating efficient electrolyte ion transfer and diffusion due to the abundance of pores. Moreover, with a significant specific surface area of 1588 m^2/g, numerous active sites were generated, aided by substantial oxygen doping, resulting in pseudo-capacitance. These carbon sheets demonstrate a notable specific capacitance of 407 F/g at 1 A/g in a three-electrode setup.

Yan *et al.* utilized waste lotus stems, characterized by their low cost and environmental friendliness, to fabricate nitrogen-doped porous carbon materials designated as LS-NCs for supercapacitor applications [48]. The overall nitrogen content, comprising pyridine nitrogen (N-6) and pyrrolic/pyridinic (N-5) contents amounted to 94.7%, significantly enhancing conductivity. SEM images illustrating the distinctive structure are presented in Fig. 2.

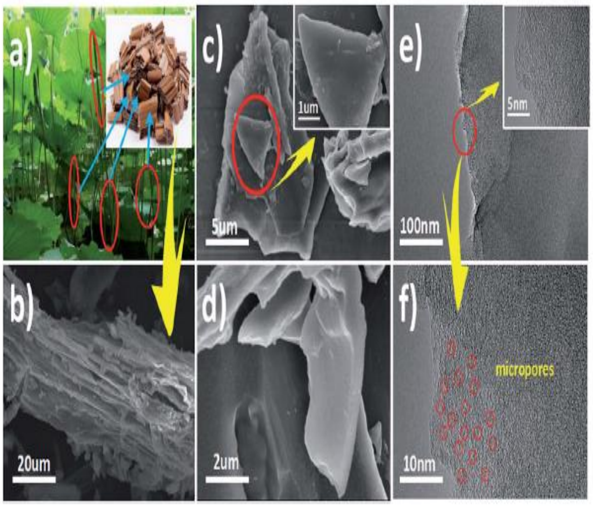

Figure 2. (a) Photo of Lotus stem (b) SEM of lotus stem (c, d) SEM of LS-NC-600 (e, f), SEM of LS-NC-600 [48].

The LS-NCs achieved an impressive specific surface area of 1322 m^2/g, showcasing outstanding electrochemical performance with a specific capacitance of 361 F/g at a current density of 0.5 A/g. Notably, the porous carbons exhibited exceptional cycling stability, retaining 96% of the specific capacitance after 5000 cycles. The unique structure derived from abundant waste lotus stems positions them as an environmentally friendly and cost-effective material for high-performance supercapacitors.

Wang *et al* prepared well-structured porous carbon sheets from fresh clover stems under air atmosphere [49]. A facile potassium chloride salt-sealing procedure was applied as shown in Fig. 3. Porous carbon sheets thus obtained acquired a high specific surface area of 2244 m^2/g and rich pore structures, which provide fast ion diffusion channels and abundant storage active sites. A high specific capacitance of 436 F/g at 1 A/g was tapped. Tremendous rate capacities with capacitance retaining 290 F/g at 50 A/g were established. Moreover, a high specific capacitance of 420 F/g at 0.5 A/g was delivered by the assembled symmetric supercapacitor. An excellent energy density of 58.4 Wh/kg and good cycling stability of 99.4% capacitance retention at 5 A/g after 30,000 cycles were displayed.

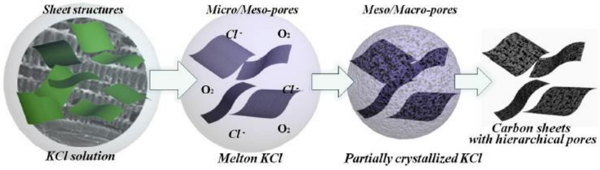

Figure 3. Illustration of the formation of carbon sheets [49].

Phiri *et al* utilized willow wood and prepared highly porous willow-based carbon [50], as shown in Fig. 4. It had a pore volume of 1.45 cm^3/g and a high surface area of ~2800 m^2/g, exhibiting 394 F/g as the specific capacitance at a current density of 1 A/g. A good cycling stability, retaining ~94% capacitance after 5000 cycles at a current density of 5 A/g was displayed in 6 M KOH electrolyte. Using 1M Na_2SO_4 electrolyte, an excellent rate performance like a high working voltage of 1.8 V was exhibited in a symmetrical two-electrode full-cell setup.

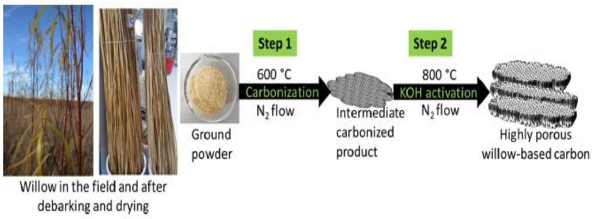

Figure 4. Diagram showing the synthesis of willow-derived derived AC [50].

Compilation of phytomass precursors sourced from plant stems/straws and utilized in synthesizing electrode materials for capacitors is presented in Table 2.

Table 2. Phytomass precursors as stem/straw of plant for the synthesis of electrode materials.

S. No	Precursor	Activation	Electrolyte	S_{BET} (m^2/g)	Specific capacitance (F/g)	Reference
1	Tobacco stem	KOH	1 M $LiPF_6$-EC/DMC/DEC	3326	190	[43]
2	Rice straw	KOH	1 M H_2SO_4 $EMIMBF_4$	1007	332 80	[44]
3	Wheat straw	KOH	$MeEt_3NBF_4$/AN	2316	251	[45]
4	Cotton stalk	KOH	1 M H_2SO_4	1964	254	[46]
5	Cornstalk	NaCl, KCl	1 M H_2SO_4	1588	407	[47]
6	Lotus stem	KOH	6 M KOH	1322	360	[48]
7	Clover stems	KCl	1 M H_2SO_4	2244	436	[49]
8	Willow wood	KOH	6 M KOH	2800	394	[50]

Phytomass carbon from leaves

Five types of AC were prepared from waste tea-leaves by Peng *et al* [51] using KOH as activating agent. XRD patterns show a broad diffraction peak positioned at 43°, corresponding to the (100) diffractions of graphitic carbon with the amorphous character, as shown in Fig. 5. Specific surface area lies from 2245 m^2/g to 2841 m^2/g. Five ACs prepared showed the highest specific capacitance of 330 F/g at a current density of 1 A/g in an aqueous KOH electrolyte.

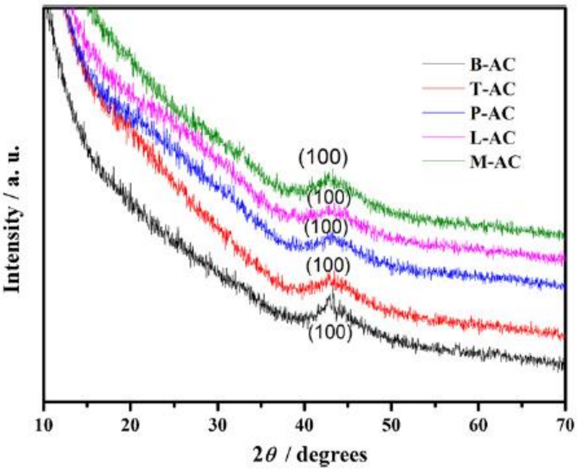

Figure 5. XRD of the five types of ACs [51].

Jain *et al* [52] utilized eucalyptus leaves biomass for preparing electrode material with organic functional groups and high BET surface area as shown in Fig. 6. Environmentally friendly materials like CH_3COONa, graphite foil, etc., are used in supercapacitors. Three to fourfold enhancement in capacitive performance was observed by adding HQ (hydroquinone) into CH_3COONa. Excellent cyclic behavior was displayed for over 10000 cycles with redox additive.

Lotus leaf biomass was used to fruitfully produce AC with a high specific surface area. Carbonization and KOH activation was employed by Qu *et al* [53]. Lotus leaf porous carbon has been reported to have exhibited an appreciable performance when calcined at 800°C. The specific capacitance of 379 F/g and 298 F/g were tapped at 1 A/g and 20 A/g respectively. Good cycling stability was also displayed after 5000 cycles and was reported to reach a capacitance retention rate of 90%.

Ahmed *et al*. [54] investigated AC derived from neem leaves in conjunction with a gel polymer electrolyte (GPE) containing $LiClO_4$ salt in EC:PC (1:1 v/v.) incorporated into a PVdF-HFP solution. The resulting low-cost AC exhibited a regular pore size of 2.51 nm and a specific surface area of 705 m^2/g. A GPE film was prepared using the solution-cast technique. The ionic conductivity and electrochemical stability window of the GPE ($LiClO_4$/EC:PC/PVdF-HFP) at room temperature were determined, affirming the suitability of the GPE meant for EDLC fabrication. The specific capacitance of the fabricated cell was evaluated through various characterization techniques such as cyclic voltammetry (CV), electrochemical impedance spectroscopy (EIS), and charge-discharge tests, with the observed values presented in Table 3.

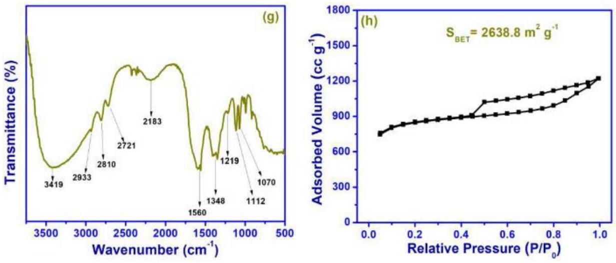

Figure 6. FTIR spectra and N_2 adsorption-desorption isotherm studies of the eucalyptus leaves carbon sample [52].

Table 3. Values of Specific capacitance using CV, EIS, and CD.

Techniques	Specific Capacitance (F/g)
CV (at 10mV/s)	68
EIS (at 10 mHz)	57
Charge-discharge (at 1 mA/cm^2)	74

Wang *et al* [55] prepared porous carbon from waste celtuce leaves by pyrolysis in argon flow at 600 °C, following activation using KOH. Porous carbon thus prepared has a large pore volume of 1.88 cm^3/g and a very high specific surface area of 3404 m^2/g. GCD curves at different current densities and CV at various scan rates are shown in Fig.S1 (Supplementary material). The specific capacitance of 421 and 273 F/g in two and three-electrode systems were respectively obtained in KOH aqueous electrolyte.

Li et al. [56] derived AC from fallen (dried) leaves of *Fraxinus chinensis* which are synthesized by the activation of both KOH and K_2CO_3 (scheme shown in Fig. S2). The specific capacitance reached up to 242 F/g (0.3 A/g, 6 M KOH) in a two-electrode system. Better cycling stability with nearly no reduction in capacitance was reported even after 2000 cycles.

Fan et al [57] derived porous carbons from the nettle leaf (scheme shown in Fig. S3) and have been found to possess high specific surface area (1951 m^2/g), huge total pore volume (up to 1.374 cm^3/g), and high content of oxygen and nitrogen heteroatom doping (up to 17.85 at% shared). A superior specific capacitance of 163 F/g at 0.5 A/g in an ionic liquid electrolyte (EMIM.BF_4) with a capacitance retention as high a value of 67.5% at 100 A/g was demonstrated. Also, a low capacitance loss of just 8% after 10000 cycles was projected.

To have a quick comparison, various phytomass precursors from leaves employed to synthesize electrode materials for capacitors are shown in Table 4.

Table 4. Phytomass precursors as leaf waste of plant for synthesizing carbon electrode materials for capacitors.

S.No	Precursor	Activation	Electrolyte	SBET (m^2/g)	Specific capacitance (F/g)	Reference
1	Waste tea leaves	KOH	2 M KOH	2245-2841	330	[51]
2	Eucalyptus leaves	KOH	CH_3COONa		208	[52]
			CH_3COONa + HQ	2639	685	
			Na_2SO_4			
			Na_2SO_4 + HQ		173	
					377	
3	Lotus leaf	KOH	6 M KOH	2488	379	[53]
4	Neem leaves	$ZnCl_2$	1 M $LiClO_4$ in EC/PC	705	68	[54]
5	Celtuce leaves	KOH	2 M KOH	3404	421	[55]
6	Fallen leaves	KOH/K_2CO_3	6 M KOH	2869	242	[56]
7	Nettle leaves	KOH	EMIM BF_4	1951	163	[57]

Phytomass carbon from flowers

Khan *et al* [58] used withered rose flowers for synthesizing activated porous carbons (mentioned as RDPC) through a simple two-step method of carbonization and chemical activation utilizing KOH/KNO_3. RDPC thus prepared has an enhanced specific surface area of 1980 m^2/g. This study has shown the HR-TEM and SAED (selected area electron diffraction) images of the obtained RDC (a–c) and RDPC (d–f) samples at different resolutions. RDPC exhibited an appreciable electrochemical activity as a supercapacitor electrode (6M KOH as the electrolyte) including ultrahigh SC exhibiting 350 F/g at 1 A/g.

Porous carbon nanosheets were synthesized by Veerakumar *et al* [49] by the carbonization of *Bougainvillea spectabilis* through physical and chemical activations. Carbon powders prepared from paper flowers (paper flower carbon - PFC) showed a maximum surface area of up to 1801 m^2/g with an assailable porous graphitic carbon layer arrangement. This feature warrants potential application in energy storage (and dye removal). In 1M H_2SO_4 aqueous electrolyte, potentiostatic and galvanostatic measurements using a three-electrode cell were carried out demonstrating a specific capacitance of 118, 109.5, 101.7, 93.6, and 91.2 F/g at 1, 2, 4, 8 and 12 A/g respectively. In Fig. S4, EIS spectra of the PFC-700 and PFC-800 modified electrodes are shown and also EIS before and after 1000 cycles are displayed.

Paulownia flower AC (a-PFCs) show suitable pore size distributions, maximum specific surface areas, super hydrophilicity, and partial graphitization phase, which are all necessary for achieving high electrochemical behavior as supercapacitor electrodes. (Chang et al) [60]. XRD and FTIR spectra graphs are displayed in Fig. S5. The symmetric supercapacitor offers a superior specific capacitance of 297 F/g at a reasonable current density (1 A/g in 1 M H_2SO_4 electrolyte).

Chen *et al* [61] worked on the elm flower-based AC (ELAC). It had a pore volume of 0.88 cm^3/g, N and S contents, and a surface area of 2048.6 m^2/g. ELAC displayed a specific capacitance of 275 F/g at a current density (1 A/g) and retained a capacitance of 216 F/g at 20 A/g only because of N and S functional groups. CV of ELAC-1, ELAC-2, and ELAC-3 at various scan rates and comparison of ELAC-x at a scan rate of 2 mV/s is shown in Fig. S6.

Wu *et al* [52] worked on Albizia flowers and obtained a total pore volume of 1.47 cm^3/g with a high specific area (2758 m^2/g). More self-doped N contents and unique porous microrod features were observed. The resulting porous carbon micro rods demonstrated a notable specific capacitance of 406 F/g at 0.5 A/g (335 F/g at 10 A/g) in 6 M KOH electrolyte, along with a commendable rate capability of 86%.

Sivachidambaram *et al* [63] prepared AC from *Borassus flabellifer* flower (BFF). Employing different activation temperatures (600, 700, 800, and 900 °C) and H_3PO_4 as an activating agent, the AC was prepared. This study has used 1M KOH electrolyte, the Asian palmyra palm's CV at various scan rates of BFF-6, BFF-7, BFF-8, and BFF-9 samples are shown. Table S1 lists the phytomass precursors from various flowers of plants employed to synthesize carbon electrode materials for capacitors.

Phytomass carbon from seeds

Elmouwahidi *et al* [64] prepared AC from argan seed shells by KOH activation. Due to the hindrance of the surficial carboxylate groups towards electrolyte distribution into the pores, the O-rich AC exhibited a low capacitance of 259 F/g. Owing to well-evolved micro and mesoporosity, the pseudo capacitance effects of N functionalities, N-rich AC showed the highest capacitance of 355 F/g in 1 M H_2SO_4 as electrolyte.

Sunflower seed shell containing nanoporous carbons was prepared and used as electrode material in capacitors [65]. Activation temperatures and ratio of KOH determine the pore structure of the carbons, as well known. The capacitive performance of these carbons (in 30 wt. % KOH electrolyte) is observed to be much better so the carbon from sunflower seed shells was made as a superior electrode material for capacitors.

Hu *et al* [66] investigated the capacitance features of pistachio shells char activated by KOH. AC showed ideal capacitive behaviors at an extensive range of scan rates and possessed excellent reversibility and high power properties in aqueous electrolytes (0.5 M H_2SO_4, 0.5 M Na_2SO_4, and 1M $NaNO_3$).

Olivares-Marin *et al.* [67] investigated the activation of cherry stones using KOH. The precursor, carbonized at temperatures ranging from 800 to 900 °C, yielded carbons with average pore sizes around 0.9–1.3 nm and substantial specific surface areas ranging from 1100 to 1300 m2/g. Consequently, the samples exhibited high capacitances at low current density, reaching up to 230 F/g in a 2M H_2SO_4 (aqueous electrolyte) and 120 F/g in the aprotic medium 1M $(C_2H_5)_4NBF_4$/acetonitrile.

Kalyani and Anitha [68] investigated AC derived from jackfruit seeds and reported superior specific capacitance as elevated as 316 and 203 F/g respectively in 1M H_2SO_4 and 1M Na_2SO_4 electrolytes (scan rate of 10mV/s). SEM image of jack fruit seed is displayed in Fig. S7. Also, it showed excellent electrochemical cycle stability in 1M H_2SO_4 with 93% capacitance retention at the end of 500 cycles. Kalyani *et al* [69] worked on papaya seeds using $ZnCl_2$ (activating agent) and got the specific capacitance of 472 F/g in 1M H_2SO_4 electrolyte, as calculated from CV. Hence the biomass of papaya seeds represents a burgeoning and ever-green source of carbon for capacitor electrodes.

A list of phytomass precursors from seeds employed to synthesize carbon electrode materials for capacitors is given in Table S2.

Phytomass carbon from fruits

Guardia *et al* [70] proposed residue valorization as the well-organized approach to attain a cost-effective circular economy and the scheme is shown in Fig. S8. Hydrothermal carbonization of apple bagasse and apple waste after juice and cider production as a precursor is projected. An electrochemical capacitance of 290 F/g and a specific surface area of 2000 m^2/g are reported. Excellent performance makes them very promising for energy storage in supercapacitors.

Ranaweera *et al* [71] have worked with an orange peel-based electrode (KOH electrolyte). 100% capacitance retention during 5000 cycles was reported. The work explains that bio-waste can be easily changed into an efficient and high-performance energy storage device by using a carefully designed electrode/electrolyte system.

KOH-activated pineapple crown waste [72] possesses a pore volume of 0.362 m^3/g, a surface area of 700 m^2/g, and a pore diameter of 22 nm. Pineapple crown-derived carbon electrode exhibits a good fiber structure with a diameter of 42–73 nm. SEM of the MN700 sample at 1000X, 5000X, and 40000X magnifications is presented in Fig. S9. The observed specific capacitance was as high as 150 F/g, thereby proving the excellent electrochemical properties of supercapacitor cells.

Vinayagam *et al* [73] have worked on *Syzygium cumini* fruit shells (SCFS) for the fabrication of symmetric supercapacitors. Carbonization at 700 °C in the N_2 atmosphere and CO_2 activation at 700 °C in the N_2 atmosphere were employed to get AC. Enhanced electrochemical performance in a three-electrode configuration is shown by SCF-AC. An innovative and environmentally safe approach with good porosity in AC for energy storage behavior is planned.

Elaiyappillai *et al* [74] explored *Cucumis melo* (Cm) fruit peel's electrochemical studies with 1M aqueous KOH. The novel fabricated Cm-based AC electrode (Cm-900) exhibits a superior specific capacitance value of 404 F/g at 1 A/g. Highly porous Cm-900 electrode may prove as an excellent candidate for high-performance supercapacitors.

A list of phytomass precursors from fruits, employed to synthesize carbon electrode materials for capacitors is given in Table S3.

Phytomass carbon from roots of plants

Vinayagam *et al* [73] have worked on *Chrysopogon zizanioides* roots (CZR) employing carbonization at 700 ºC in the N_2 atmosphere and CO_2 activation at 700 ºC in the N_2 atmosphere. The CZR-AC obtained showed enhanced electrochemical performance in three-electrode configurations with high specific capacitance data.

Wang *et al* [75] used tamarisk roots as a carbon precursor to successfully fabricate an innovative tamarisk root-based honeycomb-like porous carbon (TRHPC). Simple activation and carbonization approach and mixed hybrid activators containing NaCl and $ZnCl_2$ are employed. TRHPC shows good electrochemical properties with a high specific capacitance of 293 F/g at 0.5 A/g. High-rate performances with 61.5% capacitance retention from 0.5 to 50 A/g were reported.

Guo *et al*. [76] produced 3D hierarchical porous carbon by facile carbonization followed by chemical activation taking soybean roots (SRs) as the carbon precursor. The scheme of the work is shown in Fig. S10. High specific surface area (2143 m^2/g), good electrical conductivity coupled with unique 3D hierarchical porosity offered excellent electrochemical performance as an electrode material for supercapacitors. Superior cycling stability i.e. 98% capacitance retention after 10000 cycles at 5 A/g, high capacitance (276 F/g at 0.5 A/g) was obtained. A good rate capability in a symmetric two-electrode supercapacitor setup in 6M KOH was demonstrated.

Table S4 lists phytomass precursors from the root employed to synthesize carbon electrode materials for capacitors.

Effects/influence of self-doped heteroatoms on the specific capacitance/pseudo capacitance of PAC

The effects of self-doped heteroatoms on the specific capacitance or pseudo capacitance of PAC have been a recent subject of interest in the area of energy storage and supercapacitor development. We all know that the PAC refers to the AC materials obtained from renewable biomass precursors such as agricultural waste, wood, or other plant-based materials. These materials are carbonized and activated to generate porous structures with high surface area. Numerous chemical active principles present in the plant precursors get ruptured into organic functional moieties during carbonization and chemical activation processes and these organic functionalities containing O, and/or N/S, or even P will usually be terminated on the carbon surface or incorporated into the carbon structure. These heteroatoms are hence called *self-doped* heteroatoms in the context of PAC and can significantly impact the performance of supercapacitor electrodes [77].

It is known from the literature on the electrochemistry of phytomass-derived AC that the occurrence of oxygen boosts up the polarity of the carbon surface, thus making it hydrophilic, representing it more reversible in electrochemical environments and nitrogen in the sample boosts the capacitance by improving electrical conductivity [64,78], while the presence of sulfur favors adsorption and transfer of electrolyte ions [69,70] and further extends the interlayer spacing in the carbon structures to deliver copious electrochemical active sites. Moreover, the existence of heteroatoms enhances the wettability of the carbon electrode, which in turn may improve the electrochemistry of the electrode [81] via introducing pseudo-capacitance.

As we know, sulfur belongs to the chalcogen group along with oxygen, and the functionalization with sulfur-containing groups is anticipated to be an important approach in tuning carbon chemistry. Organic functional groups containing sulfur mediate carbon chemistry in multiple ways depending on their oxidation states and thus show potential influences in biomass conversion [82], heavy metal recovery [83], and supercapacitors [84]. Carbon materials usually react with H_2SO_4 (as an electrolyte), and the surface will be grafted with sulfonate [85].

Recently, the importance of sulfur-based functional groups in AC has been perceived to enhance the electrochemical performance, and hence sulfur-doped carbon materials are being studied as supercapacitor electrodes [86]. The sulfur self-doped carbons with a high content of sulfur were mainly prepared by sulfur-containing chemicals or by adding extrinsic sulfur sources [86,87]. Gu et al used polythiophene to produce sulfur-containing AC for double-layer capacitors [88]. Ma et al applied sucrose with $MgSO_4$ to produce S-doped carbon fiber [89] and Liu *et al*. employed glucose with sublimed sulfur to acquire sulfur-doped carbon spheres [90].

Doping can be sorted into two types: external and self-doping. Self-doping occurs when heteroatoms are naturally incorporated into the carbon structure during the activation process, typically from the biomass feedstock itself and heteroatom doping involves introducing atoms of elements other than carbon into the carbon lattice. Common heteroatoms used for doping include nitrogen (N), sulfur (S), oxygen (O), and phosphorus (P). It is interesting to note that the PAC has enormous sulfur contents and it is this fact that attracted the present authors to focus on this subject for the supercapacitor electrodes. Also, there have been a few research reports about the utilization of plant wastes with a high content of intrinsic sulfur to prepare sulfur self-doped carbons [91,92]. Because of the substantial amounts of intrinsic sulfur in phytomass, the element sulfur would be self-doping in the structures of phytomass during the thermal treatment process. Surprisingly, these reports on carbon materials for supercapacitors do not seem to have considered the role of self-doped sulfur in the electrochemical performance of the final products but focus only on the pore structures instead and the effects of electrolytes used. Nevertheless, the influence of sulfur has not been clear and hence it is worth studying.

Noteworthy effects of self-doped heteroatoms on PAC in supercapacitor electrodes have been summarized below.

Enhanced capacitance: The presence of self-doped heteroatoms can facilitate additional pseudocapacitance in the AC electrode, leading to enhanced overall electrochemical capacitance. Redox reactions taking place with the S-, O-, and N-containing organic functionalities on the carbon surface strongly show the contribution of huge Faradaic pseudocapacitance coupled with electrochemical double-layer charging capacitance.

The presence of active heteroatoms enhances the capability of charge storage in the material, resulting in higher specific capacitance and improved energy storage performance.

Enhanced electrical conductivity and electrochemical stability: Self-doped N-atoms can contribute towards increased electrical conductivity and the structural stability of the AC, making it more resistant to degradation during charge-discharge cycles. This enhanced stability ensures the longevity and cycling performance of the supercapacitor electrode. The presence of self-doped heteroatoms can modify the surface chemistry of the AC. This can influence the adsorption of electrolyte ions and improve the overall performance of the supercapacitor. S favors the adsorption and transfer of electrolyte ions as well and further extends the interlayer spacing of the carbon structure to offer ample electrochemical active sites, influencing the overall electrochemical performance.

Tailored surface chemistry: Different self-doped heteroatoms are present as specific surface functional groups on the AC, which can modify its surface chemical properties like wettability, hydrophilicity/hydrophobicity, etc., as stated earlier. This tailored surface chemistry can influence the adsorption of electrolyte ions, leading to improved ion diffusion kinetics and faster charge-discharge rates.

Improved pore configuration: The presence of self-doped heteroatoms can also influence the pore organization of carbon materials. This may lead to the formation of additional micropores or mesopores, which can increase the surface area and provide more active sites for charge storage.

Environmentally friendly and cost-effective: Utilizing PAC with self-doped heteroatoms is generally considered more environmentally friendly than traditional methods that rely on external chemical doping methods, which often involve harmful chemicals. Also, PAC is abundant, renewable, and of zero cost compared to other carbon sources. AC with self-doped heteroatoms can be an economical way to develop the performance of supercapacitor electrodes without significantly increasing production costs.

However, it is essential to note that the % content and specific effects of heteroatoms in PAC can change depending on the source of phytomass, the choice of the activation process, and the intended application of the AC. Extensive research and characterization are therefore necessary to understand the precise impact of heteroatoms on the properties and application of AC materials and performance.

Having observed the diverse effects and benefits arising from the self-doped heteroatoms within the porous phytomass AC, it is imperative to probe into the underlying mechanisms responsible for the observed pseudo-capacitance and the resultant enhancement in overall capacitance. This investigation extends to understanding how these heteroatoms interact in acid, neutral, and alkaline environments as electrolytes. The authors of this research have undertaken a comprehensive analysis of these interactions, and the detailed findings will be presented in a subsequent publication.

In our exploration, we leverage both our empirical insights gained through extensive research with various porous ACs and insights extracted from the existing body of literature. The existing theoretical model establishes a direct correlation between the specific surface area of AC and the expected specific capacitance. However, the practical scenario unfolds with more intricacies, challenging this simplistic perspective. Surprisingly, certain ACs boasting seemingly modest surface areas exhibit a notably higher specific capacitance than counterparts with larger surface areas. This intriguing divergence is underpinned by the presence of a substantial fraction of the surface area concealed within the micropores of the AC particles, rendering it inaccessible to the electrolyte ions employed in electrochemical assessments [93]. Thus, it becomes evident that an effective assessment of capacitance, encompassing both capacitance and pseudo capacitance, necessitates a nuanced consideration of factors such as pore size distribution, overall surface area, the presence of organic functional groups, and electrical conductivity within the AC structure.

Summary, perspectives, and future challenges

From the preceding sections, it is certain that over the past few years, global attention has been devoted to developing electrochemical supercapacitors as a complementary or alternative power source to batteries for their multifarious applications including electric/hybrid vehicles, electronic equipment, computer memory backup, etc. Despite many types of carbon materials being presently employed as supercapacitor electrode materials including ACs, carbon nanotubes, carbon nanofibers, and graphene sheets, ACs with an array of exceptional characteristics like porous structure and excellent surface composition and good chemical stability have attracted boundless research interest in the same.

In the present energy scenario, zero-cost plant biomass (i. e. phytomass) for producing low-cost-active carbons merits consideration. Hence from the above viewpoints, the authors have summarized to date the significant progress realized with the AC-based electrode materials for supercapacitors, specifically derived from various parts of plants as the precursor choices, which are apparently the zero-cost and eco-benevolent resources. Undeniably the reference works presented here follows the concept of circular bioeconomy. As said earlier, the overall electrochemical performance of supercapacitors is an interplay between the choice of carbon precursors, activation methodologies, carbon textural properties (specific surface area, morphology, porosity, and pore-size distribution), electrical conductivity, the presence of huge and variable electrochemically active surface composition (organic functional moieties - highly functionalized surface) that imparts hydrophilic-hydrophobic propensity, multiple and versatile green-natural options of selecting phytomass are available to us that allows the preparation of multifunctional carbon powders for the desired applications [94]. A diagram illustrating the interaction between the characteristics of the electrode material and the functionality of the capacitor has been provided in Fig. S11.

Hence the discussion made in this consolidated report provides impetus for the global researchers and would also complement the values of phytomass and its preparation, features, and applications for augmenting the existing literature. Nevertheless, there are still unsettled debates regarding the role and mechanism of the self-doped heteroatoms (intrinsic S, O, and N) present surficial on the AC and their synergy towards contributing to the improved performance of supercapacitors (pseudocapacitance), and hence this fact is inviting global research. No doubt doping carbon materials with other active heteroatoms will portray the better performance of supercapacitors but because of the foregoing explanation, it can now be stated that carbon materials can be selected with self-doped heteroatoms especially with sulfur, to witness more application ranges soon.

Undeniably, the virtues of PACs mentioned herein pave clear ways to fabricate or engineer commercially viable AC-based materials meant for numerous innovative applications for instance in electrocatalysis, photocatalysis, microfluidic devices, biosensors, up-to-the-minute energy storage devices, and much more in this manner enhancing future research. While PAC exhibits numerous parameter advantages and impressive performance, the available representative results and comparisons can portray certain challenges and perspectives of the study.

Some of the focal challenges to further root its share in the renewable energy market are the gap in the technological innovations to increase productivity, reducing the cost of production/supercapacitor fabrication, scalability, and consistency in material quality, and thus remains to be addressed. Nevertheless, these challenges present opportunities for additional research and development in this field, prompting endeavors to focus on creating additional user-friendly and cost-efficient technologies across a variety of scales. This, in turn, aims to attract increased investment in the energy sector. Looking forward still further to the challenges, the synthesis of PAC can be optimized by exploring innovative activation techniques and combining it with other nanomaterials to enhance its properties like energy density and cycle stability of the energy storage devices. Additionally, collaborative efforts between academia and industry can accelerate the integration of this material into practical supercapacitor devices.

As we pass toward a sustainable future, PAC holds great promise in shaping the landscape of energy storage technology. By harnessing the potential of this green-natural resource, scientists and engineers can contribute significantly to the advancement of renewable energy systems. We encourage further exploration of this fascinating yet indispensable field and anticipate groundbreaking developments in the pursuit of greener and more efficient supercapacitors - the gold capacitors or the power caches. It is hoped that this review will encourage more and more researchers to engage themselves in the fabrication of high-performance supercapacitors to face the current energy dilemma.

Future outlook on the plant-based AC materials for future energy storage devices

The future outlook for plant biomass-derived AC in energy storage devices, particularly supercapacitors, is promising due to the following key factors.

Sustainability and environmental impact. Utilizing plant biomass for AC production supports sustainable practices by repurposing agricultural waste and reducing reliance on fossil fuel-derived materials. This aligns with global efforts to transition to greener energy solutions and minimize environmental impact.

High performance metrics. Research indicates that ACs derived from specific plant materials can achieve high specific surface areas and favorable pore size distributions. These characteristics enhance the capacitance and energy density of supercapacitors. For instance, ACs from certain plants have demonstrated capacitance values exceeding 400 F/g, making them competitive with traditional materials.

Advancements in material science. Ongoing innovations in material science are likely to improve the performance of plant biomass-derived ACs. Techniques such as chemical activation and nitrogen doping can further enhance the electrochemical properties of these materials, leading to better energy storage capabilities.

Integration with renewable energy. As the demand for renewable energy sources increases, the need for efficient energy storage solutions becomes critical. Plant biomass-derived AC can play a vital role in stabilizing energy supply from intermittent renewable sources, such as solar and wind, by providing reliable storage options.

Research and development support. There is a growing focus on research and development in the field of supercapacitors, with significant investments from governments and private sectors. This support is aimed at discovering next-generation materials and optimizing existing technologies, which will likely benefit the development of plant biomass-derived ACs.

Potential for hybrid systems. The development of hybrid energy storage systems that combine supercapacitors with batteries could enhance overall performance. Plant biomass-derived ACs could serve as effective electrodes in these hybrid systems, improving energy density while maintaining rapid charge and discharge capabilities. In summary, the distinctive characteristics of plant biomass-derived AC, along with continuous advancements in material science and a growing emphasis on sustainable energy solutions, make these materials highly promising for future energy storage applications. Their incorporation into supercapacitors and hybrid systems has the potential to greatly enhance the efficiency and reliability of energy storage technologies, facilitating the transition to a more sustainable energy future.

CONCLUSION

PAC represents remarkable sustainable and efficient energy storage advancements in the development of supercapacitors. It harnesses the potential of organic waste, offers excellent porosity and electrical conductivity, and aligns with the principles of ecocentrism. As the world seeks cleaner and more sustainable energy solutions, PAC emerges as a ray of hope, exemplifying the ingenious ways we can harness Nature's potential for green energy. While there are significant opportunities, researchers and engineers must address challenges related to performance optimization, durability, scalability, and environmental considerations to unlock the full potential of these materials in the energy storage landscape. With further research and development, this technology may have a pivotal role in the transition to a more sustainable and eco-friendly energy future. Collaborative efforts across academia, industry, and policymakers will be essential in driving this technology move forward. In conclusion, the authors have investigated additional phytomass beyond those discussed in this review for various multifunctional applications. Readers can refer to references [95-99] for further details and gain insight into the vast potential for exploring numerous other phytomass in the future.

ACKNOWLEDGEMENTS

The authors extend their appreciation to the Deanship of Research and Graduate Studies at King Khalid University for funding this work through Large Research Project under grant number RGP2/242/45. The authors extend their sincere thanks to the administration of Madurai Kamaraj University, Madurai for their unwavering support and encouragement, which made is possible to undertake this work.

ABBREVIATIONS

PAC	Phytomass-derived activated carbon
AC	Activated carbon
EJ	Exajoule
BET	Brunauer-Emmett-Teller
3D	Three Dimension
SSA	Specific surface area
EDLC	Electrochemical double-layer capacitance
DEC/DMC/EC	Diethyl carbonate / Dimethyl carbonate / ethylene carbonate
LIBs	Lithium ion batteries
TEM	Tunnelling electron microscopy
LED	Light emitting diode
FTMAC	Activated carbon with flute type micropores
LS-NCs	Lotus stem - Nitrogen doped carbon
SEM	Scanning electron micrograph
GPE	Gel polymer electrolyte
EC:PC	Ethylene carbonate : propylene carbonate
PVdF-HFP	Poly(vinylidene fluoride-co-hexafluoropropylene)
CV	Cyclic voltammetry
EIS	Electrochemical impedance spectroscopy
HQ	Hydroquinone
RDPC	Withered rose flowers activated porous carbons
HR-TEM	High resolution - tunnelling electron microscopy
SAED	Selected area electron diffraction
SC	Supercapacitance or supercapacitor
ELAC	Elm flower-based AC
PFC	Paper flower carbon
BFF	Borassus flabellifer flower
SCFS	Syzygium cumini fruit shells
Cm	Cucumis melo
CZR	Chrysopogon zizanioides roots
TRHPC	Tamarisk root-based honeycomb-like porous carbon
SRs	Soybean roots

REFERENCES

[1] P. Lauri, P. Havlík, G. Kindermann, N. Forsell, H. Böttcher, M. Obersteiner, Energy Policy 66 (2014) 19–31. https://doi.org/10.1016/j.enpol.2013.11.033.

[2] V. Lebaka, in Biofuel Technologies, V. Gupta, M.G. Tuohy Eds., Springer, Berlin (2013), p. 223. https://doi.org/10.1007/978-3-642-34519-7_9.

[3] P. McKendry, Bioresour. Technol. 83 (2002) 47–54. https://doi.org/10.1016/S0960-8524(01)00119-5.

[4] M. Kaltschmitt, in Renewable Energy from Biomass, M. Kaltschmitt, N.J. Themelis, L.Y. Bronicki, L. Söder, L.A. Vega Eds., Springer, New York (2013) p. 1393. https://doi.org/10.1007/978-1-4614-5820-3_924.

[5] WBA, WBA Global bioenergy statistics 2018, Summary Report, World Bioenergy Association, www.worldenergy.org (2018). https://www.worldbioenergy.org/uploads/181017%20WBA%20GBS%202018_Summary_hq.pdf.

[6] S.D. Vassilev, L. Andersen, C. Vassileva, T. Morgan, Fuel 94 (2012) 1–33. https://doi.org/10.1016/j.fuel.2011.09.030.

[7] J. Popp, S. Kovács, J. Oláh, Z. Divéki, E. Balázs, New Biotechnol. 60 (2021) 76–84. https://doi.org/10.1016/j.nbt.2020.10.004.

[8] A. Tursi, Biofuel Res. J. 22 (2019) 962–979. https://doi.org/10.18331/BRJ2019.6.2.3.

[9] T.H. Kim, H. Kwak, T.H. Kim, K.K. Oh, Energies 13 (2020) 352. https://doi.org/10.3390/en13020352.

[10] T. Temesgen, Y. Dessie, E. Tilahun, L.T. Tufa, B.A. Gonfa, T.A. Hamdalla, C.R. Ravikumar, H.C. Ananda Murthy, ACS Omega, 9 (2024) 30725–30736. https://doi.org/10.1021/acsomega.4c03123.

[11] J. Amrita, S.K. Tripathi, Mater. Sci. Eng., B 183 (2014) 54–61. https://doi.org/10.1016/j.mseb.2013.12.004.

[12] S.J. Allen, L. Whitten, G. McKay, Dev. Chem. Eng. Miner. Process. 6 (1998) 231–261. https://doi.org/10.1002/apj.5500060501.

[13] O. Ioannidou, A. Zabaniotou, Renewable Sustainable Energy Rev. 11 (2007) 1966–2005. https://doi.org/10.1016/j.rser.2006.03.013.

[14] W. Ao, J. Fu, X. Mao, Q. Kang, C. Ran, Y. Liu, H. Zhang, Z. Gao, J. Li, G. Liu, J. Dai, Renewable Sustainable Energy Rev. 92 (2018) 958–979. https://doi.org/10.1016/j.rser.2018.04.051.

[15] E. Menya, P.W. Olupot, H. Storz, M. Lubwama, Y. Kiros, Chem. Eng. Res. Des. 129 (2017) 271–296. https://doi.org/10.1016/j.cherd.2017.11.008.

[16] N.A Rashidi, S. Yusup, J. Cleaner Prod. 129 (2017) 271–296. https://doi.org/10.1016/j.jclepro.2017.09.045.

[17] H. Lee, K. An, S. Park, B. Kim, Nanomaterials 9 (2019) 608. https://doi.org/10.3390/nano9040608.

[18] Z. Z. Chowdhury, S.B.A. Hamid, R. Das, M.R Hasan, S.M. Zain, K. Khalid, M.N. Uddin, BioResources 8 (2013) 6523–6555. https://doi.org/10.15376/biores.8.4.6523-6555.

[19] P.G. García, Renewable Sustainable Energy Rev. 82 (2018) 1393–1414. http://dx.doi.org/10.1016/j.rser.2017.04.117.

[20] A. El-Naggar, A.H. El-Naggar, S.M. Shaheen, B. Sarkar, S.X. Chang, D.C. W. Tsang, J. Rinklebee, Y.S. Ok, J. Environ. Manage. 241 (2019) 458–467. https://doi.org/10.1016/j.jenvman.2019.02.044.

[21] A. Aworn, P. Thiravetyan, W. Nakbanpote, J. Anal. Appl. Pyrolysis 82 (2008) 279–285. https://doi.org/10.1016/j.jaap.2008.04.007.

[22] S. Balci, T. Dogu, H. Yucel, J. Chem. Technol. Biotechnol. 60 (1994) 419–426. https://doi.org/10.1002/jctb.280600413.

[23] M.A. Yahya, Z. Al-Qodah, C.Z. Ngah, Renewable Sustainable Energy Rev. 46 (2015) 218–235. https://doi.org/10.1016/j.rser.2015.02.051.

[24] M.I. Din, S. Ashraf, A. Intisar, Sci. Prog. 100 (2017) 299–312. https://doi.org/10.3184/003685017X14967570531606.

[25] A. Ahmad, H.M. Al-Swaidan, A.H. Alghamdi, J. Chem. Soc. Pak. 37 (2015) 1081–1087. https://jcsp.org.pk/PublishedVersion/da1050bc-8125-4cdc-ac13-985f52ab3159Manuscript%20no%202,%20Final%20Gally%20Proof%20of%2010561%20(Hassan%20Mohammed%20Al-Swaidan).pdf.

[26] O.A. Ekpete, M. Horsfall, J.N.R, Res. J. Chem. Sci. 3 (2011) 10–17. https://www.researchgate.net/publication/281212790_Preparation_and_characterization_of_activated_carbon_derived_from_fluted_pumpkin_stem_waste.

[27] V.K. Gupta, D. Pathania, S. Sharma, P. Singh, J. Colloid Interface Sci. 401 (2013) 125–132. https://doi.org/10.1016/j.jcis.2013.03.020.

[28] M. Fan, W. Marshall, D. Daugaard, R.C. Brown, Bioresour. Technol. 93 (2004) 103–107. https://doi.org/10.1016/j.biortech.2003.08.016.

[29] V. Minkova, M. Razvigorova, E. Bjornbom, R. Zanzi, T. Budinova, N. Petrov, Fuel Process Technol. 70 (2001) 53–61. https://doi.org/10.1016/S0378-3820(00)00153-3.

[30] J. Li, Y.Gao, K. Han, J. Qi, M. Li, Z. Teng, Sci Rep 9 (2019) 17270. https://doi.org/10.1038%2Fs41598-019-53869-w.

[31] S.Ghosh, R. Santhosh, S. Jeniffer, V. Raghavan, G. Jacob, K. Nanaji, P. Kollu, S. K. Jeong, A. N. Grace, Sci Rep 9 (1) (2019). https://doi.org/10.1038/s41598-019-52006-x.

[32] N. Kumar, S.B. Kim, S.Y. Lee, S.J. Park, Nanomaterials (Basel) (2022) 12(20) 3708. https://doi.org/10.3390%2Fnano12203708.

[33] .Yu, N. Fu, J. Zhao, R. Liu, F. Li, Y. Du, Z Yang, ACS Omega (2019). https://pubs.acs.org/doi/10.1021/acsomega.9b01916.

[34] M.I.A. Abdel Maksoud, R.A. Fahim, A.E. Shalan, M.A. Elkodous, S.O. Olojede, A.I. Osman, C. Farrell, H. Al-Muhtase, A.S. Awed, A.H. Ashour, D.W. Rooney, Environ Chem Lett 19 (2021) 375–439. https://doi.org/10.1007/s10311-020-01075-w.

[35] B. Arumugam, G. Mayakrishnan, S.K.S. Manickavasagam, S.C. Kim, R. Vanaraj, Crystals 13 (7) (2023), 1118. https://doi.org/10.3390/cryst13071118.

[36] M. Li, Y. Fang, J. Li, B. Sun, J. Du, Q. Liu, Mater Lett, 318 (2022) 132182. https://doi.org/10.1016/j.matlet.2022.132182.

[37] K. Dujearic-Stephane, M. Gupta, A. Kumar, V. Sharma, S. Pandit, P. Bocchetta, Y. Kumar, J Compos Sci, 5(3) (2021) 66. https://doi.org/10.3390/jcs5030066.

[38] T.Temesgen, E.T. Bekele, B.A. Gonfa, L.T. Tufa, F.K. Sabir, S. Tadesse, Y. Dessie, J EnergyStorage 73 (2023) 109293, 1–23. https://doi.org/10.1016/j.est.2023.109293.

[39] J. Zhao, A. Burke, J. Energy Chem. 59 (2021) 276–291. https://doi.org/10.1016/j.jechem.2020.11.013.

[40] K. Mensah-Darkwa, C. Zequine, P.K. Kahol, R.K Gupta, Sustainability 11 (2019) 1–22. https://doi.org/10.3390/su11020414.

[41] Y. Zhang, S. Liu, X. Zheng, X. Wang, Y. Xu, H. Tang, F. Kang, Q.H. Yang, J. Luo, Adv. Funct. Mater. 27 (2016) 1–8. https://doi.org/10.1002/adfm.201604687.

[42] X. He, P. Ling, J. Qiu, M. Yu, X. Zhang, C. Yu, M. Zheng, J. Power Sources 240 (2013) 109–113. http://dx.doi.org/10.1016/j.jpowsour.2013.03.174.

[43] X. Xia, H. Liu, L. Shi, Y. He, J. Mater. Eng. Perform. 21 (2012) 1956–1961. https://doi.org/10.1007/s11665-011-0101-3.

[44] N. Sudhan, K. Subramani, M. Karnan, N. Ilayaraja, M. Sathish, Energy Fuels 31 (2016) 977–985. http://dx.doi.org/10.1021/acs.energyfuels.6b01829.

[45] L. Xueliang, H. Changlong, C. Xiangying, S. Chengwu, Microporous Mesoporous Mater. 131 (2010) 303–309. http://dx.doi.org/10.1016/j.micromeso.2010.01.007.

[46] X. Tian, H. Ma, Z. Li, S. Yan, L. Ma, F. Yu, G. Wang, X. Guo, Y. Ma, C. Wong, J. Power Sources 359 (2017) 88–96. https://doi.org/10.1016/j.jpowsour.2017.05.054.

[47] C. Wang, D. Wu, H. Wang, Z. Gao, F. Xu, K. Jiang, J. Mater. Chem. A 6 (2017) 1244–1254. https://doi.org/10.1039/C7TA07579K.

[48] S. Yan, J. Lin, P. Liu, Z. Zhao, J. Lian, W. Chang, L. Yao, Y. Liu, H. Lin, S. Han, RSC Adv. 8 (2018) 6806–6813. https://doi.org/10.1039/C7RA13013A.

[49] C. Wang, D. Wu, H. Wang, Z. Gao, F. Xu, K. Jiang, J. Power Sources 363 (2017) 375–383. http://dx.doi.org/10.1016/j.jpowsour.2017.07.097.

[50] J. Phiri, J. Dou, T. Vuorinen, P.A.C. Gane, T.C. Maloney, ACS Omega 4 (2019) 18108–18117. https://doi.org/10.1021/acsomega.9b01977.

[51] C. Peng, X. Yan, R. Wang, J. Lang, Y. Oub, Q. Xue, Electrochim. Acta 87 (2013) 401–408. https://doi.org/10.1016/j.electacta.2012.09.082.

[52] D. Jain, J. Kanungo, S.K. Tripathi, J. Alloys Compd. 832 (2020) 1–13. https://doi.org/10.1016/j.jallcom.2020.154956.

[53] S. Qu, J. Wan, C. Dai, T. Jin, F. Ma, J. Alloys Compd. 751 (2018) 107–116. https://doi.org/10.1016/j.jallcom.2018.04.123.

[54] S. Ahmed, M. Parvaz, R. Johari, M. Rafat, Mater. Res. Express 5 (2018) 1–10. http://doi.org/10.1088/2053-1591/aab924.

[55] R. Wang, P. Wang, X. Yan, J. Lang, C. Peng, Q. Xue, Activated carbon Appl. Mater. Interfaces 4 (2012) 5800–5806. https://doi.org/10.1021/am302077c.

[56] Y. T. Li, Y. T. Pi, L. M. Lu, S. H. Xu, T.Z. Ren, J. Power Sources 299 (2015) 519–528. https://doi.org/10.1016/j.jpowsour.2015.09.039.

[57] W. Fan, H. Zhang, H. Wang, X. Zhao, S. Sun, J. Shi, M. Huang, W. Liu, Y. Zheng, P. Li, RSC Adv. 9 (2019) 32382–32394. https://doi.org/10.1039/C9RA06914C.

[58] A. Khan, R.A. Senthil, J. Pan, Y. Sun, X. Liu, Batteries Supercaps 3 (2020) 731–737. https://doi.org/10.1002/batt.202000046.

[59] P. Veerakumar, T. Maiyalagan, B. Gnana Sundara Raj, K. Guruprasad, Z. Jiang, K.C. Lin, Arab. J. Chem. 13 (2020) 2995–3007. https://doi.org/10.1016/j.arabjc.2018.08.009.

[60] J. Chang, Z. Gao, X. Wang, D. Wu, F. Xu, X. Wang, Y. Guo, K. Jiang, Electrochim. Acta 157 (2015) 290–298. https://doi.org/10.1016/j.electacta.2014.12.169.

[61] H. Chen, F. Yu, G. Wang, L. Chen, B. Dai, S. Peng, ACS Omega 3 (2018) 4724–4732. https://doi.org/10.1021/acsomega.8b00210.

[62] F. Wu, J. Gao, X. Zhai, M. Xie, Y. Sun, H. Kang, Q. Tian, H. Qiu, Carbon 147 (2019) 242–251. https://doi.org/10.1016/j.carbon.2019.02.072.

[63] M. Sivachidambaram, J.J. Vijaya, L.J. Kennedy, R. Jothiramalingam, H.A. Al-Lohedan, M.A. Munusamy, E. Elanthamilan, J.P. Merlin, New J. Chem. 41 (2017) 3939–3949. https://doi.org/10.1039/C6NJ03867K.

[64] A. Elmouwahidi, Z. Zapata-Benabithe, F. Carrasco-Marın, C. Moreno-Castilla, Bioresour. Technol. 111 (2012) 185–190. https://doi.org/10.1016/j.biortech.2012.02.010.

[65] X. Li, W. Xing, S. Zhuo, J. Zhou, F. Li, S.Z. Qiao, G.Q. Lu, Bioresour. Technol. 102 (2011) 1118–1123. https://doi.org/10.1016/j.biortech.2010.08.110.

[66] C.C. Hu, C.C. Wang, F.C. Wu, R.L. Tseng, Electrochim. Acta 52 (2007) 2498–2505. http://dx.doi.org/10.1016/j.electacta.2006.08.061.

[67] M. Olivares-Marin, J.A. Fernandez, M.J. Lazaro, C. Fernandez-Gonzalez, A. Macias-Garcia, V. Gomez-

Serrano, F. Stoeckli, T.A. Centeno, Mater. Chem. Phys. 114 (2009) 323–327. https://doi.org/10.1016/j.matchemphys.2008.09.010.

[68] P. Kalyani, A. Anitha, Int. J. Res. Eng. Technol. 3 (2014) 225–238. http://dx.doi.org/10.15623/ijret.2014.0309036.

[69] P. Kalyani, A. Anitha, A. Darchen, Int. J. Eng. Sci. Res. Technol. 4 (2015) 110–122. https://www.ijesrt.com/Old_IJESRT/issues%20pdf%20file/Archives-2015/January-2015/16_OBTAINING%20ACTIVATED%20CARBON%20FROM%20PAPAYA%20SEEDS%20FOR%20ENERGY%20STORAGE%20DEVICES.pdf.

[70] L. Guardia, L. Suárez, N. Querejeta, R.R. Madrera, B. Suárez, T.A. Centeno, ACS Sustain. Chem. Eng. 7 (2019) 17335–17343. http://dx.doi.org/10.1021/acssuschemeng.9b04266.

[71] C.K. Ranaweera, P.K. Kahol, M. Ghimire, S.R. Mishra, R.K. Gupta, C 3 (2017) 1–17. https://doi.org/10.3390/c3030025.

[72] E. Taer, A. Apriwandi, Y.S. Ningsih, R. Taslim, Agustino, Int. J. Electrochem. Sci. 14 (2019) 2462–2475. http://dx.doi.org/10.20964/2019.03.17.

[73] M. Vinayagam, R.S. Babu, A. Sivasamy, A.L. Ferreira de Barros, Biomass Bioenergy 143 (2020) 1–8. http://dx.doi.org/10.1016/j.biombioe.2020.105838.

[74] E. Elaiyappillai, R. Srinivasan, Y. Johnbosco, P. Devakumar, K. Murugesan, K. Kesavan, P.M. Johnson, Appl. Surf. Sci. 486 (2019) 527–538. https://doi.org/10.1016/j.apsusc.2019.05.004.

[75] Y. Wang, L. Zhao, H. Peng, X. Dai, X. Liu, G. Ma, Z. Lei, Ionics 25 (2019) 4315–4323. https://link.springer.com/article/10.1007/s11581-019-02966-x.

[76] N. Guo, M. Li, Y. Wang, X. Sun, F. Wang, R. Yang, Activated carbon Appl. Mater. Interfaces 8 (2016) 33626–33634. https://doi.org/10.1021/acsami.6b11162.

[77] A. Gopalakrishnan, S. Badhulika, J. Power Sources 480 (2020) 1–17. https://doi.org/10.1016/j.jpowsour.2020.228830.

[78] Z. Li, Z. Xu, X. Tan, H. Wang, C.M. BHolt, T. Stephenson, B.C. Olsen, D. Mitlin, Energy Environ. Sci. 6 (2013) 871–878. https://doi.org/10.1039/C2EE23599D.

[79] D. Zhang, L. Zheng, Y. Ma, L. Lei, Q. Li, Y. Li, H. Luo, H. Feng, Y. Hao, Activated carbon Appl. Mater. Interface, 6 (2014) 2657–2665. https://doi.org/10.1021/am405128j.

[80] M. Seredych, T.J. Bandosz, J. Mater. Chem. A 1 (2013) 11717–11727. https://doi.org/10.1039/C3TA12252B.

[81] T.K. Enock, C.K. King'ondu, A. Pogrebnoi, Y.A.C. Jande, Int. J. Electrochem. 2017 (2017) 1–14. http://dx.doi.org/10.1155/2017/6453420.

[82] M. Toda, A. Takagaki, M. Okamura, J.N. Kondo, S. Hayashi, K. Domen, M. Hara, Nature 438 (2005) 178. https://doi.org/10.1038/438178a.

[83] A. Macias-Garcia, C. Valenzuela-Calahorro, A. Espinosa-Man-silla, A. Bernalte-Garcia, V. Gomez-Serrano, Carbon 42 (2004) 1755–1764. http://dx.doi.org/10.1016/j.carbon.2004.03.009.

[84] G. Hasegawa, M. Aoki, K. Kanamori, K. Nakanishi, T. Hanada, K. Tadanaga, J. Mater. Chem. 21 (2011) 2060–2063. https://doi.org/10.1039/C0JM03793A.

[85] J.A. Macia-Agullo, M. Sevilla, M.A. Diez, A.B. Fuertes, ChemSusChem. 3 (2010) 1352–1354. https://doi.org/10.1002/cssc.201000308.

[86] W. Kiciński, M. Szala, M. Bystrzejewski, Carbon 68 (2014) 1–32. https://doi.org/10.1016/j.carbon.2013.11.004.

[87] Z. Wan, Y. Sun, Tang, C.W. Daniel, D. Hou, X. Cao, S. Zhang, B. Gao, Y.S. Ok, Green Chem. 22 (2020) 2688–2711. https://doi.org/10.1039/d0gc00717j.

[88] W. Gu, M. Sevilla, A. Magasinski, A.B. Fuertes, G. Yushin, Energy Environ. Sci. 6 (2013) 2465–2476. https://doi.org/10.1039/C3EE41182F.

[89] X. Ma, G. Ning, Y. Kan, Y. Ma, C. Qi, B. Chen, Electrochim. Acta 150 (2014)108–113. https://doi.org/10.1016/j.electacta.2014.10.128.

[90] S. Liu, Y. Cai, X. Zhao, Y. Liang, M. Zheng, H. Hu, Y. Li, X. Lan, J. Gao, J. Power Sources 360 (2017) 373–382. https://doi.org/10.1016/j.jpowsour.2017.06.029.

[91] S. Yaglikci, Y. Gokce, E. Yagmur, Z. Aktas, Environ. Technol. 41 (2019) 36–48. https://doi.org/10.1080/09593330.2019.1575480.

[92] X. Zhao, Q. Zhang, C.M. Chen, B. Zhang, S. Reiche, A. Wang, T. Zhang, R. Schlogla, D.S. Sua, Nano Energy 1 (2012) 624–630. https://doi.org/10.1016/j.nanoen.2012.04.003.

[93] D. Lozano-Castello, D. Cazorla-Amoros, A. Linares-Solano, S. Shiraishi, H. Kurihara, A. Oya, Carbon 41 (2003) 1765–1775. https://doi.org/10.1016/S0008-6223(03)00141-6.

[94] J. Conder, K. Fic, C.M. Ghimbeu, in Char and Carbon Materials Derived from Biomass, M. Jeguirim, L. Limousy Eds., Elsevier, France (2019) p. 383. https://doi.org/10.1016/B978-0-12-814893-8.00010-9.

[95] P. Kalyani, A. Anitha. Int. J. Hydrogen Energy 38 (2013) 4034–4045. https://doi.org/10.1016/j.ijhydene.2013.01.048.

[96] P. Kalyani, T.R. Banuprabha, C. Sudharsana, N. Anvarsha, in Waste Material Recycling in the Circular Economy - Challenges and Developments, D.S. Achilias Ed., IntechOpen, United Kingdom (2022). https://doi.org/10.5772/intechopen.99448.

[97] C. Sudharsana, N. Anvarsha, P. Kalyani, in Nanocomposites - Properties, Preparations and Applications, V. Parvulescu, E.M.M. Anghel Eds., IntechOpen, United Kingdom (2024). https://doi.org/10.5772/intechopen.114402.

[98] K. Ashwini. J. Sridhar, D. Aravind, K. Senthil Kumar, T. Senthil Muthu Kumar, M. Chandrasekar, N. Rajini, in Green Hybrid Composite in Engineering and Non-Engineering Applications, T. Khan, M. Jawaid Eds., Springer Nature, Singapore (2023). p.211. https://doi.org/10.1007/978-981-99-1583-5_13.

[99] T. Temesgen, Y. Dessie, E. Tilahun, L.T. Tufa, B.A. Gonfa, T.A. Hamdalla, C.R. Ravikumar, and H.C. Ananda Murthy, ACS Omega, 9 (2024) 30725–30736. https://doi.org/10.1021/acsomega.4c03123.

KALYANI PALANICHAMY[1]
BANUPRABHA THAKKU RANGACHARI[2]
SRIDHAR JAYAVEL[3]
ARAVIND DHANDAPANI[4]
VARAGUNAPANDIYAN NATARAJAN[5]

[1]Department of Chemistry, DDE, Madurai Kamaraj University, Madurai, Tamil Nadu, India
[2]Department of Chemistry, Mary Matha College of Arts and Science, Periyakulam, Tamil Nadu, India
[3]Department of Biotechnology, DDE, Madurai Kamaraj University, Madurai, Tamil Nadu, India
[4]University Science Instrumentation Centre, Madurai Kamaraj University, Madurai, Tamil Nadu, India
[5]Department of Chemical Engineering, King Khalid University, Abha, Saudi Arabia

PREGLEDNI RAD

NAPREDAK U AKTIVNOM UGLJENIKU IZ FITOMASE ZA PRIMENE U SISTEMIMA ZA SKLADIŠTENJE ENERGIJE

Fitomasa, tj. aktivni ugljenik dobijen iz biljne biomase, je svestran elektrodni materijal za energetske uređaje zahvaljujući svom prirodnom i sveprisutnom obilju, raznolikosti, ekocentrizmu i jedinstvenim fizičkim svojstvima. Ovaj rad razmatra nedavna dostignuća u oblasti aktivnog uglja dobijenog iz fitomase, uglavnom za elektrode superkondenzatora i posebno fitomasu koja uključuje različite delove biljaka ograničene na stabljiku, list, cvet, seme, voće i koren za dobijanje aktivnog uglja. uz odlične elektrohemijske performanse. Napredak u pripremi aktiviranog iz fitomase, važne činjenice vezane za sintezu i fizički i elektrohemijski atributi su takođe elaborirani, za koje se očekuje da će dati plodan pravac ka zagovaranju superkondenzatora - paketa zelene energije. Površina aktivnog uglja je obično ukrašena organskim funkcionalnim delovima koji sadrže heteroatome poput O, i/ili S/N (koji se nazivaju samodopiranim heteroatomima). Takođe, prikazana je sinergija ovih heteroatoma u povećanju pseudokapacitivnosti ugljeničnih elektroda u superkondenzatorima. Nadalje, pregled izaziva uvid u strategije, istaknute izazove, izglede, neposredne prilike i trendove koji obećavaju podršku aktivnog uglja iz različitih dijelova postrojenja koji mogu pokretati naše društvo zasnovano na energiji i naučne industrije i uspostavljanje održivog energetskog sektora, kao i iskorištavanje potencijala prirode.

Ključne reči: aktivni ugljenik; fitomasa; heteroatomi; superkondenzatori; samodopirani heteroatomi; kružna bioekonomija.

CI&CEQ
Chemical Industry & Chemical Engineering Quarterly

Available online at
Association of the Chemical Engineers of Serbia *AChE*
www.ache.org.rs/CICEQ

Chem. Ind. Chem. Eng. Q. 31 (4) 277–284 (2025) CI&CEQ

PERIASAMY MANIKANDAN SRINIVASAN
NESAKUMAR DHARMAKKAN

Department of Chemical Engineering, Kongu Engineering College, Erode, India

SCIENTIFIC PAPER

UDC 66.017/.018:544.2

EXPERIMENTAL STUDIES IN PLATE HEAT EXCHANGER USING THERMINOL-55/Al_2O_3 AND GLYCEROL/Al_2O_3 NANOFLUIDS

Article Highlights

- Al_2O_3/Therminol-55/ Water and Al_2O_3/Glycerol/Water mixed nanofluid were prepared
- The heat transfer performance of Al_2O_3 suspended base fluid was studied in a plate heat exchanger
- Individual and overall heat transfer coefficients were determined and analyzed by varying flow rates

Abstract

The experiment aimed to compare the heat transfer performance of two base fluids, Therminol-55 and glycerol, both mixed with aluminum oxide nanoparticles. The investigation focused on assessing how the addition of aluminum oxide nanoparticles (at concentrations of 0.1%, 0.2%, and 0.25% by volume) affected heat transfer in a plate heat exchanger using a mixture of Therminol-55/water and Glycerol/water. Results demonstrated a significant enhancement in heat transfer efficiency for both the hot and cold sides of the exchanger when using these nanoparticle-infused base fluid mixtures. Specifically, the study observed notably improved heat transfer coefficients for the Therminol-55/water mixture with a 0.25% nanoparticle concentration, achieving 3859 W/m²K (23% higher) for the hot fluid coefficient, 4195 W/m²K (31% higher) for the cold fluid coefficient, and an overall coefficient of 2310 W/m²K (23% higher). Similarly, the Glycerol/water mixture with a 0.25% nanoparticle concentration exhibited superior performance, reaching 4491 W/m²K (30% higher) for the hot fluid coefficient, 4395 W/m²K (36% higher)for the cold fluid coefficient, and an overall coefficient of 2508 W/m²K (28% higher). These findings indicate that the Glycerol/water mixture with aluminum oxide nanoparticles outperforms the Therminol-55/water counterpart, suggesting its potential to minimize temperature differentials within the heat exchanger and enhance operational effectiveness.

Keywords: Al_2O_3; heat transfer; Therminol-55; glycerol; nanofluid; plate heat exchanger.

Nanoparticles are particles less than 100 nm in size [1]. Both synthetic and naturally occurring nanoparticles can be found in the environment. Inorganic substances are called nanoparticles. Nanoparticles are invisible to the naked eye. They can be divided into several categories according to their sizes, forms, and features. The large surface area and nanoscale size of nanoparticles give them distinct physical and chemical characteristics. Their distinct composition, size, and form greatly influence their toughness, reactivity, and other qualities. These tiny particles are ideal for strong chemical reactivity, bio-mobility, and energy absorption because of their unique properties. Nanomaterials are divided into four categories: 0D, 1D, 2D, and 3D, depending on their general form [2]. At least one dimension of nanoclusters is between 1 and 10 nm in size, exhibiting a small size

---

Correspondence: P.M. Srinivasan, Department of Chemical Engineering, Kongu Engineering College, Erode-638 060, India.
E-mail: sriperiasamy@gmail.com
Paper received: 9 September, 2024
Paper revised: 3 November, 2024
Paper accepted: 22 November, 2024

https://doi.org/10.2298/CICEQ240903035S

distribution. Heat exchangers are used in industrial production processes to warm and cool fluids [3,4]. Glycols/aluminum oxide nanofluid is used as a base fluid in heat transfer applications. To achieve better heat transfer, we need to focus on improving the thermal conductivity and overall heat transfer characteristics of these fluids [5–8].

Recent advancements in energy reduction through the use of nanofluids are evident in a substantial body of research within the technical community. This innovative engineering fluid, known for its specialized applications, can lower costs in heat transfer operations by modifying appropriate base fluids [9]. Researchers have developed heat transfer fluids containing suspended nanoparticles for various heat transfer equipment [10,11]. Numerous researchers employed various metal oxides, including the addition of CuO nanoparticles to water [12,13], aluminum oxide/water [14], aluminum oxide/water-methanol [15], graphene/water-glycol [16], TiO_2,ZnO in water-ethylene glycol [17], Fe_2O_3 in engine oil-water mixture, Al_2O_3 and CuO nanoparticle suspension in engine oil, vacuum pump fluid, distilled water and ethylene glycol [18] and the results showed that this addition considerably increases the thermal conductivities of fluid mixtures and heat transfer coefficient. Experimental results of Al_2O_3 nanoparticle addition show that the Nusselt number increased significantly with respect to different volume fractions [19]. This study investigates the use of nanofluids for enhanced heat transfer in the oil and gas industry. Therminol 66, a common heat transfer fluid in heat exchangers, was chosen as the base fluid. To improve its heat transfer capabilities, Iron oxide (III) nanoparticles were incorporated at a concentration of 0.3% by weight (wt%). The fundamental properties of these nanofluids, such as density, viscosity, and specific heat capacity, were then measured as the heat transfer increased up to 46%, pressure drop increased up to 37.5% and friction factor increased up to 10% [20]. The result of the heat transfer effect showed energy savings of around 32% for cooling. Methanol has recently been used for a variety of heat transfer applications and different types of heat pipes (vapor-dynamic thermosyphons, conventional and micro heat pipes).

Numerous research works have looked into the special qualities and abilities these novel fluids have shown since nanofluids were first used in a variety of industries. The economically feasible nanomaterial aluminum oxide (Al_2O_3) has good thermophysical and heat transport properties and is non-toxic [21]. Heat transfer study was performed in Armfield plate heat exchanger (HT32) with an Armfield heat exchange service unit (HT30X) by preparing suspension of multi-wall carbon nanotubes in distilled water Hassaan *et al.*, reported 32% increase in Nusselt number (with 1.53% volume fraction) and with the same nanofluids in Shell and tube heat exchanger the percentage increase of the overall heat coefficient ranges between 6% and 76.4%, compared to distilled water [22,23] was reported. Heat transfer performance of two distinct heat exchangers with the same heat transfer area was assessed by Hassaan *et al.*, with a tubular heat exchanger (THE) and a shell-and-tube heat exchanger (STHE) and obtained heat transfer coefficient of STHE is 7–43% greater than that of tubular heat exchanger [24], also proposed a relationship between Reynolds number and MWCNT volume concentration for computing the Nusselt number [25]. In plate heat exchangers (PHEs) hybrid nanofluid (multi-walled carbon nanotubes (MWCNTs)-Al_2O_3/water) was used with various concentrations and reported an increase in the overall heat coefficient from 6% to 97% compared to pure distilled water [26]. An experiment was done using MWCNTs as operating fluids in an automotive radiator with louvered fins and flat tubes (Honda Civic 2005). From the study they reported a Nusselt number increment of 13.72% in comparison to pure water, also a correlation for estimating the Nusselt number in terms of the Reynolds number and MWCNTs volume concentration is provided [27]. While most research on the topic focuses on thermal conductivity studies, there is potential to investigate this material's heat transfer capabilities in real-time heat exchangers. Although employing nanofluids has many advantages, there are some disadvantages as well, such as instability, fouling, and surface erosion [28–30]. Therminol-55 provides a method to resist fouling, decrease pressure drop, increase heat transfer in ribbed tubes, and stop nanoparticle aggregation when making a nanofluid. Since the literature also demonstrates the effectiveness of small plate heat exchangers, we decided to use them in our inquiry [31]. Prior research hasn't explored the heat transfer performance of a specific nanofluid mixture: Al_2O_3-Water-Therminol-55 (AWT) within plate heat exchangers [32]. Also, it was found that Al_2O_3 nanoparticles containing Nanofluids showed increased critical heat flux, which was due to the improved Thermal conductivity of nanoparticles [34], hence Al_2O_3 was chosen. Elaboration of significant factors that play a vital part in enhancing the heat transfer characteristics of nanofluids is also needed to explore the heat transfer performance of nanofluids [35]. To address this gap, we investigated how adding Al_2O_3 nanoparticles (0.1% to 0.25% concentration) affects heat transfer in a Therminol-55/water and glycerol/water base fluid (5:95 volume ratio). The experiments were conducted at a constant hot fluid inlet temperature (60 °C) with varying flow rates (2 to 6 liters per minute).

MATERIALS AND METHODS

Preparation and properties of nanoparticle

Nanopowders refer to agglomerates of ultrafine particles, nanoparticles, or nanoclusters. Nanoparticles consist of three layers—surface layer, shell layer, and core layer. From the literature, it was noticed that To obtain stable Al_2O_3 nanofluids, many routes exist such as surfactant addition, pH control, ultrasonic agitation, functionalization, magnetic stirring, and high-pressure homogenization [36]. Hence in this study, the conversion of nanoparticles into Nanofluids is achieved through a two-step method with the help of a high-pressure homogenizer. The conversion of nanoparticles into Nanofluids is achieved through a two-step method. In this research, a two-step (sol-gel) technique was employed to suspend 50 nm Al_2O_3 nanoparticles in a water-methanol mixture. Base fluids with specific volume fractions (5% Terminol-55 + 95% water) were formulated according to calculated amounts derived from the below fraction Eq. (1).

$$\varphi = \frac{\left(m/\rho\right)_{Al_2O_3}}{\left(m/\rho\right)_{Al_2O_3} + \left(m/\rho\right)_{W:T}} \tag{1}$$

To ensure stability in the prepared nanofluid, a high-pressure homogenizer was employed, and the resulting nanofluid served as the cold fluid in the plate heat exchanger. The utilization of a high-pressure homogenizer ensures the uniform suspension of the prepared nanofluid throughout the base fluid. When designing energy-efficient systems, the thermal conductivity of heating or cooling fluids plays a crucial role. Among the key considerations in developing and controlling the process is the fluid's ability to conduct heat. Factors such as availability, cost, heat conductance, and the propensity of particles to stay uniformly dispersed in the base fluid with minimal agglomeration are all significant. Despite their superior thermal conductivity, metal oxide nanoparticles tend to agglomerate. In our investigation, we used Aluminum oxide (Al_2O_3) nanofluid for heat transfer analysis.

SEM images of aluminum oxide nanoparticle

Widely employed for material analysis, SEM (Scanning Electron Microscopy) plays a crucial role in identifying the microstructure and chemistry of materials. By projecting and scanning a focused stream of electrons across the surface, SEM produces detailed images. The interaction of electrons in the beam with the sample generates various signals, providing valuable information about the surface's composition. Figure 1 depicts SEM images of Al_2O_3 nanoparticles.

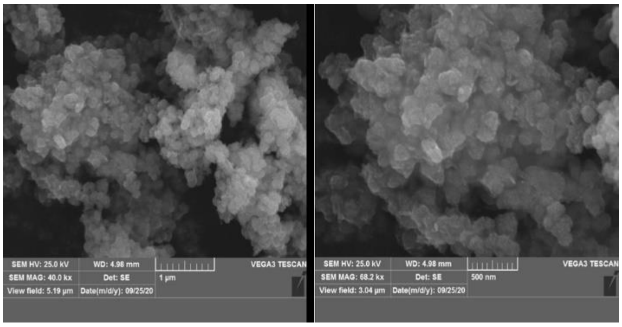

Figure 1. SEM image of Al_2O_3 nanoparticle.

Experimental setup and estimation of thermo physical properties

Experiments were conducted on a plate-type heat exchanger as described in the experimental setup (Schematic and photographic view) illustrated in Figure 2. The plate heat exchanger consists of 13 Stainless Steel corrugated plates (Alfa Laval, India) providing seven flow channels for the hot fluid and six flow channels for the cold fluid. The plate length and thickness of the plate are 0.154m and 0.25mm respectively.

Thermal conductivity was measured using a thermal conductivity analyzer (Scientico, India) and viscosity was measured with a redwood viscometer for all the concentrations of nanofluid. The density and specific heat capacity of the nanofluid were calculated from the correlations [36, 37], Eqs (2,3).

$$\rho_{nf} = (1-\varphi)\rho_f + \varphi\rho_p \tag{2}$$

$$Cpnf = \left((1-\varphi)\rho_f C_{pf} + \varphi\rho_p C_{pp}\right) / (\rho_{nf}) \tag{3}$$

The obtained results of thermophysical properties were used for calculating different dimensionless numbers (Reynolds, Prandtl, and Nusselt numbers) applied in this study.

Nanofluids based on Therminol-55 incorporating Al_2O_3 nanoparticles were prepared at different volume concentrations, including 0.1%, 0.2%, and 0.25%. The density, dynamic viscosity, heating value, and heat conductivity were subsequently calculated based on experimental findings.

Determination of Nusselt number, convective and overall heat transfer coefficient of Al_2O_3/water-methanol nanofluid

Determination of thermophysical properties of Fe_2O_3-water-engine oil nanofluid

Eq. (4), based on the Kim model, was employed

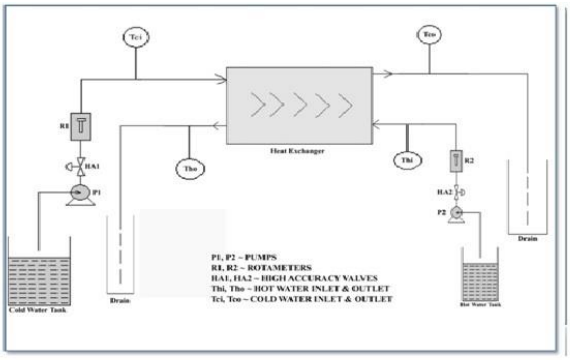

(a) Schematic diagram

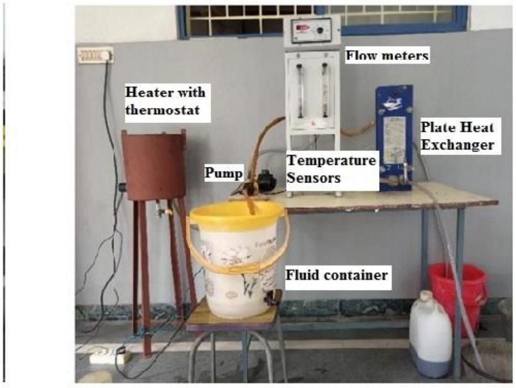

(b) Photographic view

Figure 2. Schematic and photographic view of the experimental setup.

to calculate the Nusselt number of the nanofluid. Eq. (5) was utilized to determine the heat transfer coefficient of both the hot and cold fluids. Eq. (6) is employed to find the overall heat transfer coefficient.

$$Nu = 0.295(N_{\mathrm{Re}})^{0.64}(N_{\mathrm{Pr}})^{0.32}\left(\left(\Pi/2\right)-\beta\right)\right) \tag{4}$$

$$h = \left(\frac{((Nu)(D_H))}{K}\right) \tag{5}$$

$$U = \left(\frac{(Q)_{avg}}{\left|(A)(\Delta T_{lmtd}\right|}\right) \tag{6}$$

MATERIALS AND METHODS

Effect of flow rate on hot fluid heat transfer coefficient (h_h) for Therminol-55/water base fluidat 60 °C

Prior to conducting in-depth experiments with chosen nanofluids, a preliminary study was carried out using de-ionized water to ensure the experimental study's reliability. Figure 3 illustrates the impact of flow rate on the heat transfer coefficient (h_h) of the hot fluid at a hot fluid inlet temperature of 60 °C, considering various nanofluid concentrations (Therminol-55/I_2O_3) and water.

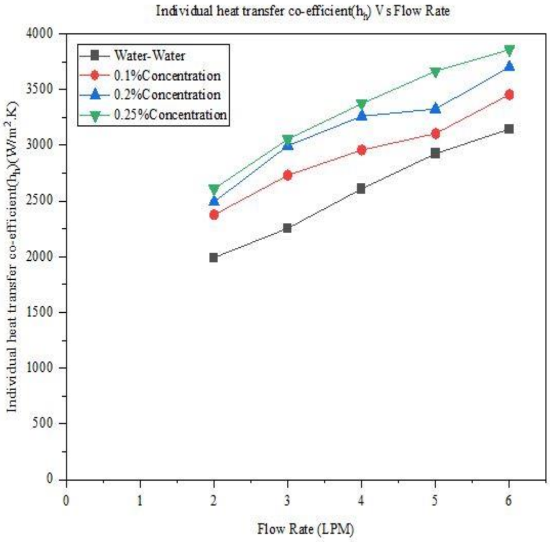

Figure 3. Effect of flow rate on hot fluid heat transfer coefficient (h_h) for Therminol-55/Water base fluid at 60 °C

According to Figure 3, The heat transfer coefficient on the hot side (hh) ranges from 1980 W/m²K for water-water, increasing to 2620 W/m²K at a flow rate of 2 Lpm for a nanofluid with a nanoparticle concentration of 0.25. With an increase in flow rate to 6 lpm, the heat transfer coefficient range also expands, starting at 3145 W/m²K for water-water and rising to 3858.77 W/m²K (for 0.25 vol.%). This underscores the significant impact of flow rate on enhancing heat transfer. This increment is because there is a significant increment in Reynolds number because of the incremental effect in density with respect to the viscosity of a nanofluid. Because of the Reynolds number increment and thermal capacity, the rate of heat transfer increases significantly.

Effect of flow rate on cold fluid heat transfer coefficient (h_c) for Therminol-55/Water base fluidat 60 °C

The effects of varying flow rates on the heat transfer coefficient on the cold side at 60°C for Therminol-55/Water base fluid were investigated and are depicted in Figure 4.

A consistent upward trend in heat transfer enhancement is evident on the cold side fluid, as depicted in Figure 4. Notably, at a low flow rate (2 Lpm) and a low nanoparticle concentration (0.25 vol.%), the heat transfer coefficient closely aligns with that of water as the base fluid. However, a gradual increase in the flow rate leads to a corresponding increase in the heat transfer rate. For example, at a flow rate of 4 lpm, the heat transfer coefficient rose to 2908.82 W/m²K (for 0.25 vol.%) from 2435.76 W/m²K (for water).

The results indicate that both the convective heat

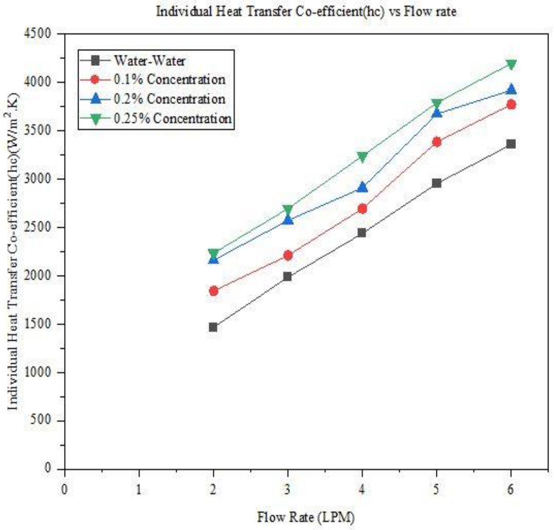

Figure 4. Effect of flow rate on cold fluid heat transfer coefficient (h_c) for Therminol-55/Water base fluid at 60 °C.

transfer coefficient and Nusselt number for Al_2O_3/Therminol-55-water nanofluid surpass those of the base fluid.

This enhancement is attributed to the improved heat transport facilitated by thermally conductive nanoparticles through the interfacial layers of fluids. The maximum enhancement was observed at 6 lpm, with a heat transfer coefficient value of 4194.54 W/m²K (for 0.25 vol.%); however, the rate of enhancement diminishes with increasing flow rate. Hence, optimizing the flow rate is essential for the efficient utilization of nanoparticles.

Effect of flow rate on hot fluid heat transfer coefficient (h_h) for Glycerol/Water base fluid at 60 °C

Given the significant impact of base fluid on heat transfer, the study was replicated with alterations in base fluid composition. This included varying the concentration and observing the effect of flow rate on the heat transfer coefficient of the hot fluid for glycerol/water-based fluid as depicted in Figure 5.

According to the data presented in Figure 5, the heat transfer coefficients for various concentrations (ranging from 0.1 vol.% to 0.25 vol.%) show notable differences. At a flow rate of 2 Lpm, the heat transfer coefficient on the hot side was recorded at 1992.23 W/m²K for water, 3845.17 W/m²K for 0.1 vol.%, and 4491.23 W/m²K for 0.25 vol.%. Similarly, at a flow rate of 6 lpm, the corresponding values were 3145.89 W/m²K for water, 3845.17 W/m²K for 0.1 vol.%, and 4101.24 W/m²K for 0.25 vol.%. These results once again underscore the effectiveness of nanoparticle suspension in enhancing heat transfer. It is also confirmed from Figure 5 that the heat transfer coefficient (h_h) enhancement is directly proportional to nanoparticle concentration and flow rate; however, the maximum enhancement was noted at 0.25 volume% of nanoparticle volume fraction.

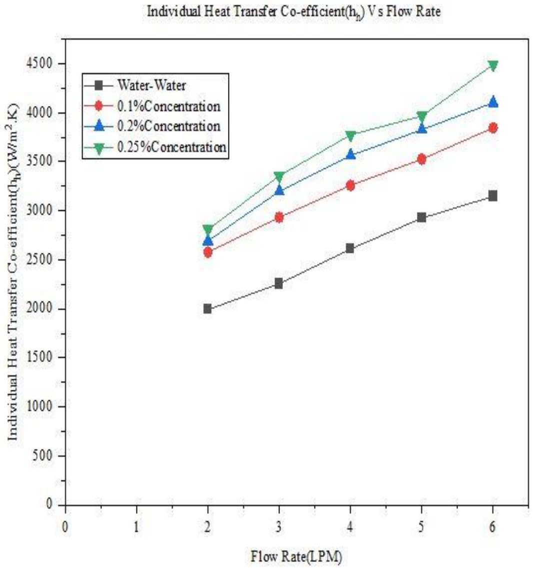

Figure 5. Effect of flow rate on hot fluid heat transfer coefficient (h_h) for Glycerol/Water base fluid at 60 °C.

Effect of flow rate on cold fluid heat transfer coefficient (h_c) for Glycerol/Water base fluid at 60 °C

The influence of flow rate on the heat transfer coefficient of the cold side at 60°C for the glycerol/water base fluid is depicted in Figure 6.

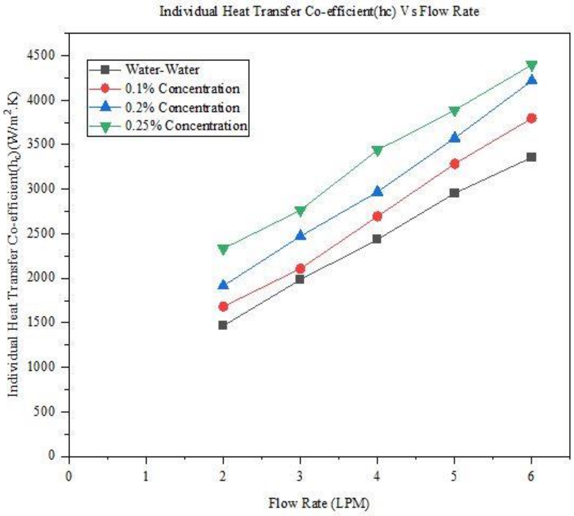

Figure 6. Effect of flow rate on cold fluid heat transfer coefficient (h_c) for Glycerol/Water base fluid at 60 °C.

The impact on the heat transfer coefficient of the cold side demonstrates an increase with a flow rate of 2 Lpm, rising from 1466.25 W/m²K (for water) to 2331.96 W/m²K (for 0.25 vol.% nanoparticle concentration). Similarly, at a flow rate of 6 Lpm, the cold side heat transfer coefficient increased from 3356.76 W/m^{2}K (for water) to 4394.54 W/m^{2}K (for 0.25 vol.% nanoparticle concentration). A notable enhancement in comparison to the Therminol-55/water base fluid was observed. This trend indicates a consistent rise in heat transfer rate, which correlates linearly with both nanoparticle concentration and temperature.

Effect of flow rate on overall heat transfer coefficient (U) for Therminol-55/water and glycerol/water base fluid at 60 °C

While the heat transfer coefficient was initially computed for individual fluids, calculating the overall heat transfer coefficient is crucial to harness the advantages offered by nanoparticles. Therefore, the findings regarding the overall heat transfer coefficient at 60 °C for Therminol-55/Water base fluid are illustrated in Figure 7a.

From Figure 7a, it is evident that at flow rates of 2, 4, and 6 lpm, the range of U was 673.87, 1285.65, and 1918.41 W/m²K (for 0.1 vol. % nanoparticle) and 742.57, 1600, and 2310.92 W/m²K (for 0.25 vol. %). This observation leads to the conclusion that both individual and overall heat transfer coefficients were significantly enhanced due to the presence of nano-sized solid particles.

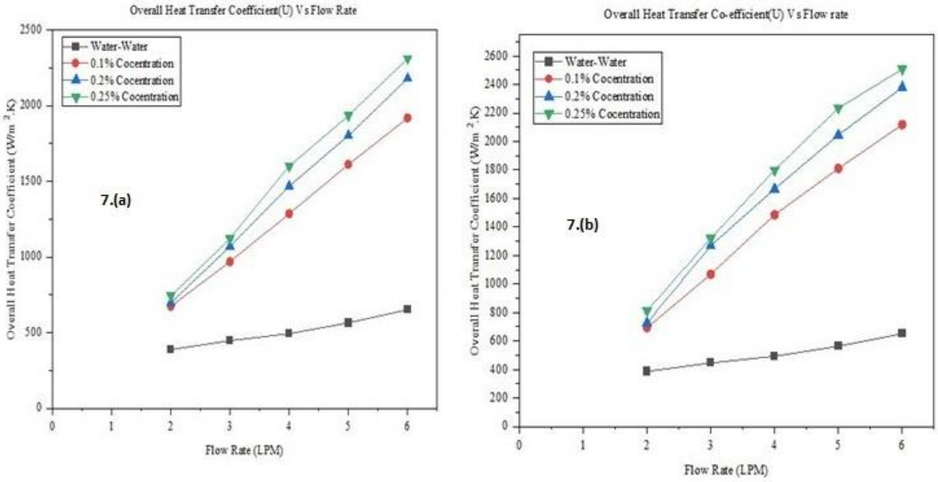

Figure 7. Effect of flow rate on overall heat transfer coefficient (U) for Therminol-55/Water and Glycerol/Water base fluid at 60 °C.

The impact of flow rate variations on the overall heat transfer coefficient at 60 °C for the glycerol/water base fluid is illustrated in Figure 7b. From Figure 7b, it was noted that Changing the base fluid favors heat transfer; Hence study was performed for both the base fluids (Therminol-55/Glycerol) Result shows that uniform enhancement in overall heat transfer rate with respect to all the concentrations (0.1, 0.2 and 0.25 vol. %) and all the flow rates. The ranges were 2118.41W/m^{2}K (for 0.1 vol. % nanoparticle to 2508.12W/m^{2}K (for 0.25 vol. % nanoparticle concentration) at a flow rate of 6 Lpm.

Due to the incremental effect on thermal conductivity of nanofluids heat transport dominates over the momentum transport and hence the Prandtl number decreases at the highest volume fractions of nanofluid. There exists a good agreement between the results calculated from these experimental values and the correlation. It was noticed that the calculated Nusselt number falls within ±8% and ±10 % deviation when compared with experimental results of (Al_2O_3/Glycerol-water) and (Al_2O_3/Therminol-55-water) nanofluids respectively, which shows the accuracy of the results of the experiment. The obtained results are consistent with the reported results that thermal conductivity, viscosity, and density of the Al_2O_3 nanofluids are increased with the addition of nanoparticles in the base fluid [22–28].

CONCLUSION

The study revealed a significant enhancement in heat transfer when nanoparticles were added to a water-water system. This improvement can be attributed to the high thermal conductivity of the solid nanoparticles, which effectively increase the rate of heat transfer within the base fluid.

Employing the (Al_2O_3/Glycerol-water) nanofluid resulted in notably decreased temperature differentials compared to the nanofluid (Al_2O_3/Therminol-55-water) within the heat exchanger, leading to improved performance of the heat exchanger.

The highest coefficients were observed at 0.25%

in Glycerol base fluid and a flow rate of 6 Lpm These peak values comprised a hot fluid coefficient of 4101.24 W/m²K, a cold fluid coefficient, and an overall coefficient of 4394.54 W/m²K and 2508.12 W/m²K respectively.

Comparing the previously mentioned heat transfer coefficient values of Glycerol base fluid nanoparticle with those of Therminol-55 base fluid nanoparticle reveals that the hot fluid coefficient increases by up to 6.28%, the cold fluid coefficient by up to 4.76%, and the overall coefficient by up to 8.5%.

Glycerol base fluid nanoparticle has a better heat transfer coefficient compared to the Therminol-55. Furthermore, the study revealed that the minimum fluid flow rate is sufficient to attain the maximum enhancement in heat transfer rate.

ACKNOWLEDGEMENTS

The authors are grateful to the management of the Kongu Engineering College and the Department of Chemical Engineering for the facility provided.

NOMENCLATURE

Al_2O_3	Aluminum Oxide
TiO_2	Titanium dioxide
ZnO	Zinc Oxide
Fe_2O_3	Iron Oxide
CuO	Copper Oxide
SiO_2	Silicon dioxide
CNT	Carbon Nano Tubes
D	Dimension
D_H	Hydraulic diameter, m
ΔT_{LMTD}	Logarithmic Mean Temperature Difference
T	Therminol-55
G	Glycerol
W	Water
m	Mass, kg
U	Overall Heat transfer coefficient, W/m^2. K
N_{Nu}	Nusselt number, dimensionless
N_{Pr}	Prandtl Number, dimensionless
N_{Re}	Reynolds number, dimensionless
Q	Heat Flux, W
Cp	Specific heat capacity, J/ (kg. K)
PHE	Plate Heat Exchanger
Pr	Prandtl number, dimensionless
H	Heat transfer coefficient, W/m2. K
Hh	Hot Fluid Heat transfer coefficient, W/m2. K
Hc	Cold Fluid Heat transfer coefficient, W/m2. K
vol. %	Volume %
Greek symbols	
β	corrugation angle, °
ρ	density, kg/m3
μ	dynamic viscosity, Pa s
$\o$	nanoparticle volume fraction, dimensionless
k	thermal conductivity, W/ (m.K)
Π	Corrugation angle

REFERENCES

[1] S.U.S. Choi, S. Lee, S. Li, J.A. Eastman, J. Heat Transfer 121 (1999) 280–289. https://doi.org/10.1115/1.2825978.

[2] S.K. Das, N. Putra, P. Thiesen, W. Roetzel, J. Heat Transfer 125 (2003) 567–574. https://doi.org/10.1115/1.1571080.

[3] S.S. Sonawane, R. S., Khedkar, K.L.T. Wasewar, Int. Commun. Heat Mass Transfer 49 (2013) 60–68. https://doi.org/10.1016/j.icheatmasstransfer.2013.10.001.

[4] M.A. Sabiha, R. Saidur, S. Mekhilef, O. Mahian, Renewable Sustainable Energy Rev. 51 (2015) 1038–1054. https://doi.org/10.1016/j.rser.2015.07.016.

[5] S.P. Manikandan, N. Dharmakkan, S. Nagamani, Chem. Ind. Chem. Eng. Q. 28 (2022) 95–101. https://doi.org/10.2298/CICEQ210125021M.

[6] S.P. Manikandan, N. Dharmakkan, M.D. Sri Vishnu, H. Prasath, R. Gokul, Hem. Ind. 75 (2021) 341–352. https://doi.org/10.2298/HEMIND210520031S.

[7] S.P. Manikandan, N. Dharmakkan, M.D. Sri Vishnu, H. Prasath, R. Gokul, G. Thiyagarajan, G. Sivasubramani, B. Moulidharan, Chem. Ind. Chem. Eng. Q. 29 (2023) 225–233. https://doi.org/10.2298/CICEQ220430029S.

[8] M.M. Sarafraz, A.D. Baghi, M.R. Safaei, A.S. Leon, R. Ghomashchi, M. Goodarzi, C.X. Lin, Energies 12 (2019) 1–13. https://doi.org/10.3390/en12224327.

[9] W. Xu, S. Wang, Q. Zhang, Q., Wang, H. Lu, H. Tan, Appl. Therm. Eng. 95 (2016) 165–177. https://doi.org/10.1016/j.applthermaleng.2015.10.164.

[10] E. Abu-Nada, Int. J. Heat Fluid Flow 30 (2009) 489–500. https://doi.org/110.1016/j.ijheatfluidflow.2009.02.003,

[11] M.M. Sarafraz, A.D. Baghi, M.R. Safaei, A.S. Leon, R. Ghomashchi, M. Goodarzi, C.X. Lin, Energies 12 (2019) 1–13. https://doi.org/10.3390/en12224327.

[12] S.P. Manikandan, R. Baskar, Chem. Ind. Chem. Eng. Q. 27 (2021) 15–20. https://doi.org/10.2298/CICEQ191220020P.

[13] B. Sahin, E. Manay, E.F. Akyurek, J. Nanomater. 2015 (2015) 1–10. https://doi.org/10.1155/2015/790839.

[14] S. Hoseinzadeh, P.S. Heyns, H. Kariman, Int. J. Numer. Methods Heat Fluid Flow 30 (2020) 1149–116. https://doi.org/10.1108/HFF-06-2019-0485.

[15] S.P. Manikandan, P.K. Chinnusamy, R. Thangamani, S. Palaniraj, P. Ravichandran, S. Karuppasamy, Y.R. Sanmugam, Chem. Ind. Chem. Eng. Q. 30 (2024) 257–264. https://doi.org/10.2298/CICEQ230726028M.

[16] S.P. Manikandan, R. Baskar, Chem. Ind. Chem. Eng. Q. 27 (2021) 177–187. https://doi.org/10.2298/CICEQ200504036P.

[17] S.P. Manikandan, R. Baskar, Chem. Ind. Chem. Eng. Q. 24 (2018) 309–318. https://doi.org/10.2298/CICEQ170720003M.

[18] S.P. Manikandan, R. Baskar, Period. Polytech., Chem. Eng. 62 (2018) 317–322. https://doi.org/10.3311/PPch.11676.

[19] T. Maré, S. Halelfadl, O. Sow, P. Estellé, S. Duret, F. Bazantay, Exp. Therm. Fluid Sci. 35 (2011) 1535–1543. https://doi.org/10.1016/j.expthermflusci.2011.07.004.

[20] A. Munimathan, T. Sathish, V. Mohanavel, A. Karthick, R. Madavan, R. Subbiah, S. Rajkumar, Int. J. Photoenergy 1 (2021) 6680627. https://doi.org/10.1155/2021/6680627.

[21] M. M. Sarafraz, A. Dareh Baghi, M. R. Safaei, A.S. Leon, R. Ghomashchi, M. Goodarzi, C. Lin, Energies 12 (2019) 4327. https://doi.org/10.3390/en12224327.

[22] A. M. Hassaan, Heat Trans. Res. 53 (2022) 19–34. https://doi.org/10.1615/HeatTransRes.2022042147.

[23] A. M. Hassaan, Int. J. Therm. Sci. 177 (2022) 107569. https://doi.org/10.1016/j.ijthermalsci.2022.107569.

[24] A. M. Hassaan, Heat Trans. Res. 54 (2023) 1–16. https://doi.org/10.1615/HeatTransRes.2023045768.

[25] A. M. Hassaan, Proc. Inst. Mech. Eng., Part E 236 (2022) 2139–2146. https://doi.org/10.1177/09544089221086825.

[26] A. M. Hassaan, Proc. Inst. Mech. Eng., Part E 237 (2022) 1310–1318. https://doi.org/10.1177/09544089221113977.

[27] A. M. Hassaan, Heat Mass Transfer 60 (2024) 1211–1219. https://doi.org/10.1007/s00231-024-03487-8.

[28] M. M. Sarafraz, A. Dareh Baghi, M. R. Safaei, A.S. Leon, R. Ghomashchi, M. Goodarzi, C. Lin, Energies 12 (2019) 4327. https://doi.org/10.3390/en12224327.

[29] N. S. Sahid, M.M. Rahman, K. Kadirgama, M.A. Maleque, J. Mech. Eng. Sci. 11 (2017) 3087–3094. https://doi.org/10.15282/jmes.11.4.2017.11.0277.

[30] B. Barbés, R. Páramo, E. Blanco, M.J. Pastoriza-Gallego, M.M. Pineiro, J.L. Legido, C.J. Casanova, J. Therm. Anal. Calorim. 111 (2013) 1615–1625. https://doi.org/10.1007/s10973-012-2534-9.

[31] S.Z. Heris, T.H. Nassan, S.H. Noie, H. Sardarabadi, M. Sardarabadi, Int. J. Heat Fluid Flow 44 (2013) 375–382. https://doi.org/10.1016/j.ijheatfluidflow.2013.07.006.

[32] B. Mehta, D. Subhedar, Mater. Today: Proc. (2023). https://doi.org/10.1016/j.matpr.2023.09.142.

[33] M. A. Rahman, S. M. Hasnain, S. Pandey, A., Tapalova, N., Akylbekov, R. Zairov, ACS omega 9 (2024) 32328–32349. https://doi.org/10.1021/acsomega.4c03279.

[34] M. M. Arani, Micro and Nano Technologies (2024) 45–75. https://doi.org/10.1016/B978-0-443-13625-2.00003-6.

[35] R.S. Khedkar, A. Saikiram, S.S. Sonawane, K. Wasewar, S.S. Umre, Procedia Eng. 51 (2013) 342–346. https://doi.org/10.1016/j.proeng.2013.01.047.

[36] W. Yu, H. Xie, L. Chen, Y. Li, Colloids Surf., A 355 (2010) 109–113. https://doi.org/10.1016/j.colsurfa.2009.11.044.

PERIASAMY MANIKANDAN SRINIVASAN

NESAKUMAR DHARMAKKAN

Department of Chemical Engineering, Kongu Engineering College, Erode, India

NAUČNI RAD

EKSPERIMENTALNA ISTRAŽIVANJA U PLOČASTOM IZMENJIVAČU TOPLOTE KORIŠĆENJEM NANOFLUIDA Terminol-55/Al_2O_3 I GLICEROL/Al_2O_3

Cilj eksperimenata je bio da se uporede performanse prenosa toplote dve bazne tečnosti, Terminol-55 i glicerola, pomešana sa nanočesticama aluminijum-oksida. Istraživanje se fokusiralo na procenu na to kako dodatak nanočestica aluminijum-oksida (u koncentracijama od 0,1%, 0,2% i 0,25% v/v) utiče na prenos toplote u pločastom izmenjivaču toplote korišćenjem mešavine Therminol-55/voda i glicerol/voda. Rezultati su pokazali značajno poboljšanje efikasnosti prenosa toplote i za toplu i za hladnu stranu izmenjivača kada se koriste ove mešavine baznih fluida sa nanočesticama. Konkretno, studija je pokazala značajno poboljšane koeficijente prenosa toplote za mešavinu Terminol-55/voda sa koncentracijom nanočestica od 0,25%, postižući 3859 V/m²K (povećanje od 23%) za koeficijent toplog fluida, 4195 V/m²K (povećanje od 31%) za koeficijent hladnog v i ukupan koeficijent od 2310 V/m²K (povećanje od 23%). Slično tome, mešavina glicerol/voda sa koncentracijom nanočestica od 0,25% pokazala je superiorne performanse, dostižući 4491 V/m²K (povećanje od 30%) za koeficijent toplog fluida, 4395 V/m²K (povećanje od 36%) za koeficijent hladnog fluida i ukupni koeficijent od 2508 V/m²K (povećanje od 28%). Ovi rezultati ukazuju na to da mešavina glicerol/voda sa nanočesticama aluminijum-oksida nadmašuje par Terminol-55/voda, što ukazuje na njen potencijal da minimizira temperaturne razlike unutar izmenjivača toplote i poboljša operativnu efikasnost.

Ključne reči: Al_2O_3; prenos toplote; terminol-55; glicerol; nanofluid; pločasti izmenjivač toplote.

Chemical Industry & Chemical Engineering Quarterly

Available online at
Association of the Chemical Engineers of Serbia *AChE*

www.ache.org.rs/CICEQ

Chem. Ind. Chem. Eng. Q. 31 (4) 285−293 (2025) CI&CEQ

AZZA MOHAMED KHALIFA[1]
NADIA ALI ELSAYED[2]
MOSTAFA AWAD[2]

[1]General Authority of Import and Export, Suez, Egypt

[2]Department of Refining and Petrochemical Engineering, Faculty of Petroleum and Mining Engineering, Suez University, Suez, Egypt

SCIENTIFIC PAPER

UDC 628.1/.2:66:519.8

COMPARATIVE ANALYSIS OF WATER NETWORK MINIMIZATION IN INDUSTRIAL PROCESSES: REGENERATION VS. NON-REGENERATION METHODS

Article Highlights

- The regeneration method focuses on minimizing water network losses, such as leakage and inefficiencies
- It minimizes the risk of system failures and distributions in water supply
- The regeneration method contributes to environmental sustainability

Abstract

The utilization of a regeneration method in water networks provides a distinct benefit by effectively decreasing the usage of freshwater and the release of wastewater; while also preventing the accumulation of contaminants; it is crucial to employ appropriate process decomposition strategies. In this study, the primary objective is to analyze the disparity between water networks that incorporate a regeneration unit and those that do not; in addition to addressing the primary objective of minimizing fresh water usage, this study focuses on examining the influence of different process decomposition strategies on the reduction of freshwater consumption using the concentration-mass load diagram as a tool for analysis. Moreover, an approach for determining interim concentrations in multiple-contaminant water systems during the concentration decomposition process was explored. Through the reduction of freshwater consumption, regenerated water flow rate, and contaminant regeneration load, the overall impact on freshwater resources was minimized, and an optimally designed regeneration recycling water network was synthesized. The evidence of the feasibility and efficacy of the proposed approach was provided by showcasing three case studies. The outcomes of the selected literature examples indicated that the designs achieved through this approach were comparable to those found in the existing literature.

Keywords: contaminant removal; mathematical modeling; optimization algorithms; regeneration methods; water network minimization.

Water network minimization plays a crucial role in enhancing the efficiency and sustainability of water distribution systems. Optimizing water consumption and reducing losses ensures the effective management of our precious water resources. This process is essential for achieving a balance between water supply and demand, conserving water, and mitigating the environmental impact of water distribution systems [1]. By implementing this approach, we can ensure a reliable water supply for communities, promote water conservation, and work towards a more sustainable future. The concept of the circular economy underscores the importance of minimizing the utilization of fresh resources through the implementation of the 3R strategies: reduce, reuse, and recycle [2]. Water consumption in Malaysia is predominantly driven by domestic and industrial activities, accounting for over 50% of the total water

---

Correspondence: A.M, Khalifa, General Authority of Import and Export, Suez, Egypt.
E-mail: azzakhalifa06@gmail.com
Paper received: 13 February, 2024
Paper revised: 19 October, 2024
Paper accepted: 2 December, 2024

https://doi.org/10.2298/CICEQ240213036K

consumption. Therefore, it is imperative to implement measures to decrease water usage in these areas, as the wastewater generated can be regenerated, reused, or treated, thereby reducing the reliance on freshwater resources [3].

The research focus on wastewater minimization has gained significant attention because of the crucial significance of water conservation and the imperative to decrease the discharge of wastewater. The incorporation of water systems plays a crucial role in attaining substantial reductions in both the consumption of fresh water and the discharge of wastewater by implementing practices such as wastewater reuse and regeneration recycling [4]. Wastewater treatment plants (WWTPs) play a crucial role in removing pollutants from water to meet water quality standards and regulations. The increasing significance of adhering to environmental standards and the inefficiencies resulting from inadequate designs and practices underline the need for systematic tools for WWTP design [5]. The objective of wastewater management is to establish measures for environmental protection while considering economic and social concerns.

In light of the imperative to preserve water resources, the utilization of reused water represents a significant and strategic milestone towards achieving sustainable development. This approach offers the potential for substantial environmental, economic, and social benefits, By implementing consumption optimization measures and promoting water reuse, industries can potentially reduce their water consumption by 25 to 30% compared to current levels within the sector [6].To overcome the difficulties of cutting water usage in industrial processes without significantly altering the plant, to get around the challenges of reducing the amount of water used in industrial operations without drastically changing the plant. There is currently a considerable trend towards the implementation of pollution control approaches at the source, specifically through the reuse and/or recycling of wastewater.

The loop-breaking technique has been discussed, highlighting how it can be adapted to manage flow rates and water losses [7]. A novel graphical method has been introduced to illustrate the relationship between supply and demand, focusing on concentration versus flow rate [8]. Achieving a global optimum in nonlinear mathematical programming [9], particularly with many variables, poses challenges. A new graphical approach addresses the distribution of wastewater quality while optimizing freshwater allocation [10]. Additionally, a method for creating water utilization networks in process plants aims to minimize fresh water and utility use [11].

The concept of concentration potential serves as a foundation for regeneration and recycling in water networks [12]. A methodical design approach has been developed to simultaneously manage energy and water systems, maximizing water reuse [13].

In practice, identifying the best strategies for reusing water between operations can be complex due to numerous mixing and reuse options. Since the early 1990s, various design methodologies have been proposed to systematically explore water reuse within networks, primarily based on limiting water profiles. This design philosophy has been successfully applied across various industrial sectors, demonstrating the benefits of integrated and system-wide analysis in water system design and operation.

The advantages of this method include targeting the maximum potential for water savings and simplifying the synthesis of water networks. This is done by manipulating information related to water conditions, such as flow rate and concentration, while not involving the specific conditions of process streams. This simplification provides a common, yet powerful, basis for integrated design frameworks, even if the mass transfer mechanisms for water use differ across operations.

Three primary applications for wastewater reuse in industry include cooling towers and HVAC systems, industrial processes and manufacturing, and energy production [14]. In industrial settings, treated wastewater can serve as a cost-effective and sustainable source for heating, cooling, and ventilation. It can function as a cooling agent, reducing freshwater intake and energy consumption, while also improving system efficiency and lowering maintenance costs.

However, it is essential to ensure that wastewater is appropriately treated and disinfected prior to use to prevent microbiological growth and minimize health risks. Effective design, maintenance, and operation of these systems are crucial for optimizing performance and safety. Wastewater can also be utilized in energy production. Treated wastewater may be used as a cooling source to drive turbines for electricity generation or as a feedstock for biofuel.

In this paper, the main focus is on the minimization of fresh water usage in water systems. To achieve this goal, the regeneration-reuse method is employed. The key aspect of this method is the determination of the specific contaminant that needs to be minimized. By analyzing the concentration of the contaminant at both the inlet and outlet points of the water system, appropriate measures can be taken to reduce its presence. The regeneration-reuse method offers several advantages. Firstly, it helps preserve valuable freshwater resources by reusing treated wastewater instead of relying solely on freshwater sources. Secondly, it contributes to cost reduction, as recycling wastewater can be more economical compared to constantly using fresh water. Additionally, it provides environmental benefits by minimizing the discharge of contaminants into natural water bodies. By incorporating the regeneration-reuse method and considering the analysis of contaminant concentration, this paper aims to optimize water networks and achieve an optimal balance between water conservation, cost reduction, and environmental sustainability.

Design and optimize an integrated water minimization and regeneration network for an industrial manufacturing facility with the following objectives and requirements [15]: minimize freshwater intake from municipal sources by 50% or more through water reuse and regeneration; maximize water recovery from process drainages, wastewater streams, and other sources; minimize life cycle costs including capital expenses, operational costs, and water/wastewater utilities.

Requirements: provide sufficient water supply to meet all process and non-potable fixture demands; regenerated water must meet quality standards for intended end uses such as cooling tower makeup, landscape irrigation, wash down, etc; system must comply with all applicable health, safety, and environmental regulations. The optimized solution should achieve the objectives through effective integration of reuse, regeneration, and minimization strategies to reduce the plant's water usage, costs, and environmental impacts.

MATERIALS AND METHODS

Methodology

The procedure essentially consists of the four steps listed below, omitting the regeneration process [16]:

Step 1: determine the freshwater processes (FWPs), which their inlet concentration is zero.

Step 2: Calculation of the limiting concentration of the regeneration processes which do not take fresh water only.

$$LimCR = C0*(1-RR) \tag{1}$$

where *Lim CR* is the limiting concentration of regeneration, *C0* is the outlet concentration of the process, and *RR* is the removal ratio.

Step 3: Allocation of source and demand. Allocation of processes according to (CPD), if the CPD for a process is equal to zero, it will take fresh water only. When multiple source streams are available, we should prioritize the reuse of one source over the others. Eq. (1) displays the source stream with the highest quasi-allocation ratio value first [16,17,18].

$$R_{i,j} = \min k = 1,2,3,\ldots NC\left(\frac{D\lim_{j,k}}{CS_{i,k}}\right) \tag{2}$$

where, *Ri,j* is the limiting quasi-allocation from Si to DJ.

When Si is the allocation to DJ, reuse critical contaminant is defined as the concentration that reaches the limiting value before any other. (RKC) for Si, DJ. The source with the next-highest quasi-allocation amount should be selected if one source is unable to fully meet the demand. (*Ri,j*) value. Calculate the mass load for demand and source at a definite reuse key contaminant by equations:

$$MD = FD*Ci \tag{3}$$

$$MS = FS*C0 \tag{4}$$

There are three cases for mass load:

The source provides all of the water in it to the demand if the mass load of RKC for the source (MS) equals the mass load of RKC for the demand (MD). If the mass load of RKC for the source is higher than the mass load of RKC for demand, in this situation, the source gives only the amount of water as follows:

$$WR = (MD/CSOUT) \tag{5}$$

The other needed water is taken from freshwater.

When the RKC mass load for the source is less than the RKC mass load for the demand. In this case, the source provides all the water needed to meet demand, and the source with the next-highest *Ri,j* value is used to provide the remaining water.

Step 4: After allocation, determine the updated concentrations at the intake and output for each process [18] as follows:

$$CN,I = (C0,I*MN)/M0 \tag{6}$$

$$CN,0 = C0,0-(C0,I-CN,I)/M0 \tag{7}$$

where *CO* is the outlet concentration, *WR* is the water required for each process, RKC is the reuse key contaminant, *CN,I* is the new inlet concentration, *Co,I* is the old inlet focus, the old mass load is *MO*, *MN* is the new mass load, *CN,O* is the new outlet concentration, and *CO,O* is the old outlet concentration.

Basically, the method consists of seven steps described in the following using the regeneration method.

Step 1: Determine the freshwater processes (FWPs), which their inlet concentration is zero.

Step 2: (1) Determine the processes that feed the regeneration process by water (BP), and тхе processes that take water from a regeneration process (AP); (2) Calculate the limiting concentration of the regeneration processes which don't take fresh water only from Eq. (1); (3) Determine the type of processes: Calculate the average of limiting concentration of regeneration. If the concentration of the contaminant is lower than the average limiting concentration take φ sign. If the contaminant concentration is at least as high as the limiting concentration average take the η sign. If $\varphi > \eta$, the process is called the below process (BP). If $\eta > \varphi$, the process is called the above process (AP).

Step 3: (1) Using CPD values to determine the order in which processes should execute; (2) Determining CPD for the (BP+FW) process by Eq. (5) [17,19]

$$CPD(Dj) = \sum_{i=1}^{Ns} \min k = 1,2,3,\ldots NC\left(\frac{CD\lim i,k}{CSi,k}\right) \qquad (8)$$

where, CD Lim I,k (Limited Demand concentration) is the limiting concentration of the contaminant K in the demand stream Dj, *CSi,k* is the concentration of the contaminant K in the source stream Si, Nc is the number of contaminants, and *NS* is the source stream order.

Step 4: Design procedure of water using networks, the design steps are as follows: (1) Allocation of processes according to order of priority factor (CPD): if the CPD for a process is equal to zero, it will take fresh water only. One should choose which source should be reused first when there are multiple streams of the sources accessible. Eq. (1) displays the source stream with the highest quasi-allocation ratio value first [16,17,18] from Eq. (2); (2) When Si is allocated to DJ, the concentration reaching the limiting value first will be called the reuse key contaminant (RKC) for Si, DJ; (3) If the demand cannot be totally satisfied by one source, another source should be used which has the next highest the lowest quasi-allocation amount (*Ri,j*) value; (4) Calculate the mass load for demand and source at a definite reuse key contaminant by Eqs. (3) and (4). In this case, the source provides all of the water in it to the demand if the mass load of RKC for the source (MS) equals the mass load of RKC for the demand (MD). The source only provides the following amount of water if the total mass load of RKC for the source is more than the mass load of RKC for the demand, from Eq. (5). When the RKC mass load for the supply is less than the RKC mass load for the demand. In this case, the source provides all the water needed to meet demand, and the source with the next-highest Ri,j value is used to provide the remaining water.

Step 5: After allocation, determine the updated concentrations at the intake and output for each process as follows by using Eqs. (6) and (7).

Step 6: calculation of inlet regeneration concentration by using Eq. (9):

$$C^0 reg = \sum\nolimits_i \left(F_{si}^{\lim} C_{reg,s}^{\lim}\right) / \sum\nolimits_i F_{si}^{\lim} \qquad (9)$$

Step 7: Repeat Step 4 Design the procedure of water using networks.

Algorithm

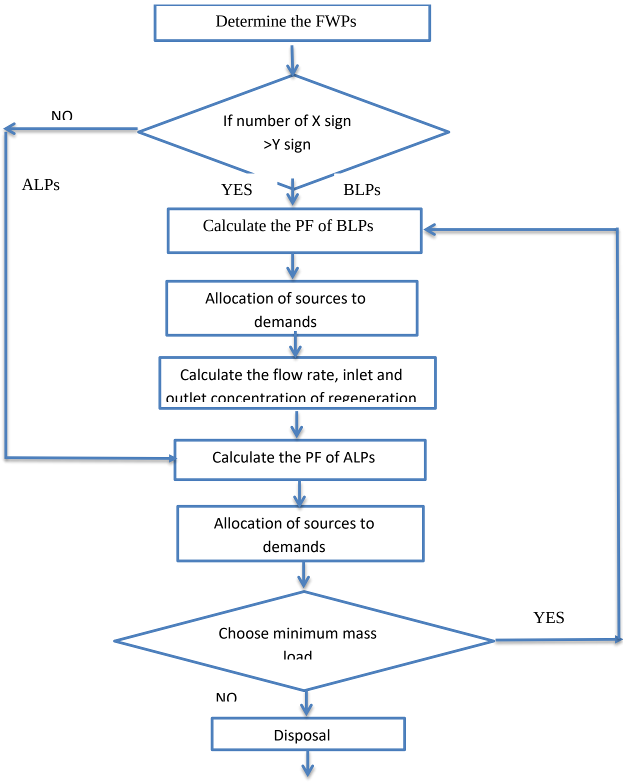

Figure 1. Water network minimization flow chart.

Case study

Example (1): (multi-contaminant, three processes). This case study is taken from [19] with the information displayed in Table 1, and the removal ratio is (0%, 99.9%, 0%).

In this particular example, a water network comprising three processes was considered, and each

Table1. Limiting data for example (1).

Process	Contaminant	Mass load (Kg/hr.)	C_{in} (ppm)	C_{out} (ppm)
Distillation	Hydrocarbon (A)	0.675	0	15
	H2S (B)	18	0	400
	SALT (c)	1.575	0	35
Hydro-desulphurization	Hydrocarbon (A)	3.4	20	120
	H2S (B)	414.8	300	12500
	SALT (c)	4.59	45	180
DE salter	Hydrocarbon (A)	5.6	120	220
	H2S (B)	1.4	20	45
	SALT (c)	520.8	200	9500

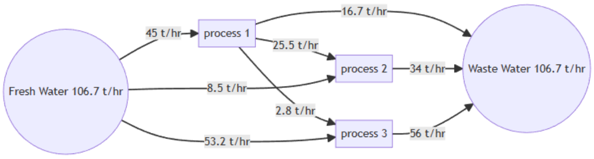

Figure 2. Network design without regeneration.

process involves three contaminants. Our objective is to design a water network that demonstrates the reduction of freshwater usage through two different methods: one without regeneration and the other with regeneration by using a removal ratio. Furthermore, a thorough comparison between these two approaches will be conducted to assess their effectiveness and efficiency [17].

The water network without regeneration

Based on the determined order of processes (P1, P3, P2), the allocation of process P1 involves a freshwater requirement of 45T/h. The determination of the recycle and keep concentration (RKC) in process 3 is denoted as (B), calculated using Eq. (2). Subsequently, Eqs (3) and (4) are employed to obtain the values. It is observed that the mass source (S1) exceeds the mass demand (D3), indicating a requirement of 2.8 t/h. of water from S1 to D3, as determined by Eqs (2) and (5). The total amount of freshwater required is 53.2 t/h. Utilizing Eqs (6) and (7), the new inlet and outlet concentrations are calculated as follows: CN, I = (0.75, 20, 1.75) ppm and CNO = (100.75, 45, 9301.75).

Within process 2, two sources, S1 and S3, are present. By applying equation (2), source S1 is selected with an assigned RKC of B. Eqs (3) and (4) are then utilized to determine the corresponding values. The analysis reveals that the mass source (S1) surpasses the mass demand (D2), indicating a requirement of 25.5 t/h. of water to be transferred from S1 to D2, as determined by Eq. (5). The total freshwater demand amounts to 8.5 T/hr. Employing Eqs (6) and (7), the new inlet and outlet concentrations can be calculated as follows: CN, I = (11.26, 300, 26.26) ppm and CNO = (111.25, 12500, 161.26).

Table S1 (Supplementary material) exhibits the definitive results achieved in Example (1) for three distinct processes, each comprising three contaminants. These results were obtained by employing the RKC method for process sequencing and selection. This table facilitates the identification of the appropriate process that aligns with the desired quantities of regeneration water. Notably, it is observed that process 1 exclusively necessitates the use of fresh water. We have only one outlet stream P3, that stream will recycle

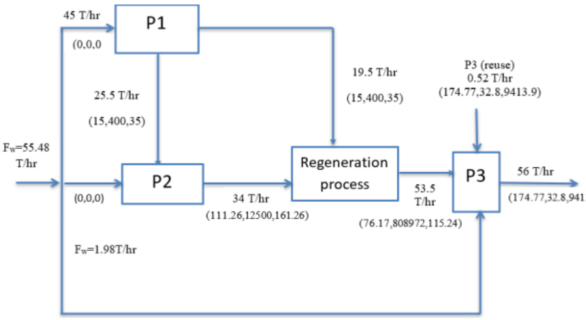

Figure 3. Final network design with regeneration.

Table S2 (Supplementary material) provides a comparative analysis between the utilization of a regeneration method and the absence of such a method. The disparity between the two approaches is evident, as the regeneration method necessitates a greater quantity of freshwater compared to the method without regeneration.

Table 2 describes the disparity between the prior research and the authors' study. The employed methodology demonstrates a decreased freshwater flow and regenerated flow that is lower than what was observed in the earlier work.

Table 2. Comparison between different methods, for example 1.

	Minimum freshwater flow rate/t·h -1	Minimum regenerated water flow rate/t·h -1
Kuo & Smith [17]	59.7	55.6
Present study	55.48	53.5

Example 2: (multi contaminant, five processes) This case study is taken from [20] using the information displayed in Table 3, including five processes, three contaminants and the removal ratio for regeneration is (0. 99.9%, 0)

In this particular example, a water network comprising five processes was considered, and each process involves three contaminants. Our objective is to design a water network that demonstrates the reduction of freshwater usage through two different methods: one without regeneration and the other with regeneration using a removal ratio. Furthermore, we will conduct a thorough comparison between these two approaches to assess their effectiveness and efficiency [20].

Table 3. Limiting data for example (2).

Process	Contaminant	C_{in} (ppm)	C_{out}(ppm)	F_{max} (T/hr.)
P1	A	0	15	50
	B	0	400	
	C	0	35	
P2	A	20	120	34
	B	300	12500	
	C	45	180	
P3	A	120	220	56
	B	20	45	
	C	200	9500	
P4	A	0	20	8
	B	0	60	
	C	0	20	
P5	A	50	150	8
	B	400	8000	
	C	60	120	

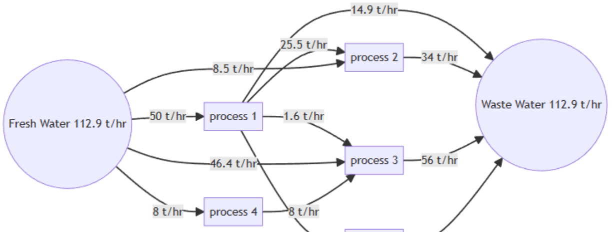

Figure 4. Network design without regeneration.

The network without regeneration

Based on the determined order of processes (P4, P1, P3, P5, P2), the allocation of processes P1 and P4 requires a freshwater requirement of 50 t/h and 8 t/h, respectively. The determination of the recycle and keep concentration (RKC) in process 3 is denoted as (B) in S4 after choosing between S1 and S4, calculated using Eq. (2). Subsequently Eqs (3) and (4) are employed to obtain the values. It is observed that the mass source (S4) is lower than the mass demand (D3). In this situation, S4 provides all the water to D3, while D3 will obtain water from other sources, specifically S1, indicating a requirement of 1.6 t/h of water from S1 to D3, as determined by equation (5). The total amount of freshwater required is 46.4 t/h. By utilizing equations (6) and (7), the new inlet and outlet concentrations can be calculated as follows: CN, I = (3.29, 20, 3.86) ppm and CNO = (103.29, 45, 9303.86). Within process 5, two sources, S1 and S3, are present. Applying Eq. (2), source S1 is selected with an assigned RKC of B. Eqs (3) and (4) are then used to determine the corresponding values. The analysis reveals that the mass source (S1) exceeds the mass demand (D5), indicating a requirement of 8 t/h of water to be transferred from S1 to D2, as determined by equation (2.5). By employing Eqs (6) and (7), the new inlet and outlet concentrations can be calculated as follows: CN, I = (15, 400, 31.25) ppm and CNO = (115, 8000, 91.25).

Within process 2, three sources, S1, S3, and S5, are present. Applying Eq. (2), source S1 is selected with an assigned RKC of B. Eqs (3) and (4) are then used to determine the corresponding values. The analysis reveals that the mass source (S1) exceeds the mass demand (D2), indicating a requirement of 25.5 T/hr. of water to be transferred from S1 to D2, as determined by Eq. (5). By employing Eqs (6) and (7), the new inlet and outlet concentrations can be calculated as follows: *CN, I* = (15, 400, 31.25) ppm and *CNO* = (115, 8000, 91.25).

Table S3 (Supplementary material) displays the conclusive outcomes obtained in example (2) involving five distinct processes, with each process consisting of three contaminants. These results were derived through the implementation of the RKC method for process sequencing and selection. The table serves as a helpful tool for identifying the most suitable process that corresponds to the desired quantities of regeneration water. It is worth noting that process 1 and process 4 specifically require the utilization of freshwater exclusively.

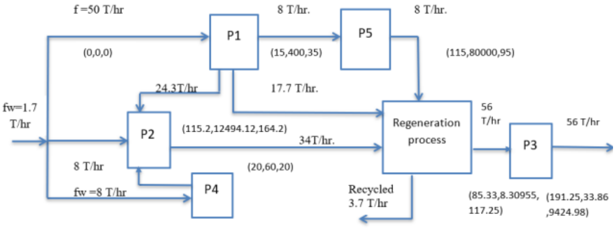

Figure 5. The final water network design with regeneration.

Table S4 (Supplementary material) presents a comprehensive comparative analysis investigating the use of a regeneration method versus the absence of such a method. The findings clearly demonstrate a notable discrepancy between the two approaches, with the regeneration method requiring a significantly larger volume of fresh water in comparison to the method that does not incorporate regeneration. This suggests that the regeneration process is more resource-intensive and demands a higher input of fresh water. It is important to consider the implications of this disparity when selecting and implementing a suitable method for water treatment or purification. Furthermore, additional research may be warranted to explore potential strategies for optimizing the regeneration process and minimizing the overall freshwater requirement.

Table 4 presents a comparison between the findings of previous research and the author's study, highlighting the divergence between the two. Our adopted methodology showcases a reduction in both freshwater flow and regenerated flow, which are lower in magnitude compared to the observations made in the earlier investigation. This indicates that our approach has successfully achieved a more efficient utilization of fresh water and regeneration resources, surpassing the outcomes of the previous research. It is important to acknowledge the significance of these advancements in terms of water conservation and resource optimization.

Table 4. Comparison between different methods for example (2).

	Minimum freshwater flow rate/t·h -1	Minimum regenerated water flow rate/t·h -1
Kuo & Smith [17]	59.7	55.6
Liu et al.	59.7	55.5
Ying, Li; Jintao, Guan	59.7	56
Present study	59.7	56

RESULT AND DISCUSSION

The optimization results of the first case show that: process (1) determines the processes that feed the regeneration process by water (BP) and the processes that take water from a regeneration process (AP), Therefore, the above and below limiting processes can be determined by Eq. (8), determining P1 and P2 as BLPs and P3 as ALPS; then, they can be allocated to the source to demand BLPs determining that P1 will take freshwater at a zero inlet concentration, and determining RKC as B. Mass load calculation, introduce that MS> MD, SO water required from S1 to D2 is 25.t/h and freshwater =8.5t/h, by Eqs (3), and (4). Respectively, the old and new mass load can be calculated and after that, the new inlet concentration and new outlet concentration can be determined by Eqs (6) and (7). the values are (11.26,300,26.26) and (111.26,12500,161.26), respectively.

Calculation of inlet and outlet regeneration concentrations by Eq. (9) gave the following values (76.16,8089.72,115.24) and (76.17,8.089.72,115.24), respectively. According to the calculation of priority factor for ALPs to determine the order of processes, Preg and P3.the allocate for ALPs and regeneration source, we can determine that RKC is contaminant A and MS less than MD, so regeneration source will give all water in it to demand of P3, fresh water is 2.5 t/h, calculate inlet and outlet concentration which values are (72.85,7.7,110.2) and (172.85,32.7,9410.3), there is only one stream, P3 will be recycled. Repeat the steps until reach the allocation of P3 and regeneration source, in this situation, MS is less than MD, so S reg will give all water to the demand and there is no other source to take water from it, the amount of fresh water is 1.98T/hr., and inlet and outlet concentrations are (74.28,8.04,197.5), (174.28,33.04,9497.5).

The optimization results of the second case show that: Using Eqs (2) and (8), we can determine whether each process is an ABLP or a BLP. Processes P1, P4, P2, and P5 are identified as BLPs, while P3 is an ALP. By calculating the priority factor, we can establish the order of the processes as follows: P1, P4, P2, P5. For P1 and P4, fresh water is required as their inlet concentrations are zero and equal to 45 t/h and 8 t/h, respectively. Regarding P2, Eq. (2) is utilized to determine that the RKC is A for source S4. In this case, MD (mass demand) is greater than MS (mass source), indicating that all the water in S4 will be allocated to D2, amounting to 8 t/h. S1 is selected as the source for P2, and the RKC is determined as B, resulting in a freshwater requirement of 2.2 t/h. The old and new mass loads are calculated using Eqs (3) and (4), respectively. The new inlet and outlet concentrations are determined using Eqs (6) and (7) as Cin = (15.2, 294.12, 29.2) and Cout = (115.2, 12494.12, 164.2). For P5, S1 is chosen as S4 has been consumed. Hence, the RKC is B. The new and old mass loads are calculated, and the new inlet and outlet concentrations are obtained as (15, 400, 35) and (115, 8000, 95). The inlet and outlet regeneration calculations from equation (2.9) are (85.53, 8309.55, 117.25) and (85.53, 8.30955, 117.25).

For P3, the RKC is determined as A from S reg, and since MD is greater than MS, all the water from S reg will be allocated to the demand, amounting to 59.7 t/h. This value exceeds 56 T/hr., so there will be remaining water from S reg. The old and new mass loads are calculated, and the new inlet and outlet concentrations are determined as (91.25, 8.86, 124.98) and (191.25, 33.86, 9424.98). By determining the minimum mass load, we can identify whether stream S3 or S reg will be recycled. In this case, the stream from S reg will be recycled. After repeating all the steps and calculating the inlet and outlet concentrations, it is observed that there is no need to recycle Preg because BLPs do not require any water from that recycled stream.

CONCLUSION

The primary focus of this study centers on minimizing the usage of fresh water in water systems. To accomplish this objective, the regeneration-reuse method is employed. A critical aspect of this method involves identifying the specific contaminant that necessitates reduction. Appropriate steps can be taken to reduce the contaminant's presence by determining its concentration at the water system's entry and output points. It provides environmental benefits by minimizing the release of contaminants into natural water bodies. By incorporating the regeneration-reuse method and considering the analysis of contaminant concentration, the primary objective of this paper is to optimize water networks and attain a harmonious balance between water conservation and environmental sustainability.

In this research, our primary objective is to analyze the disparity between water networks that incorporate a regeneration unit and those that do not, while also addressing the overarching concern of minimizing fresh water usage. Our goal is to create an optimally planned regeneration water network by minimizing the amount of freshwater used, the flow rate of regenerated water, and the load of contaminants during regeneration. Additionally, we propose simplifying the network structure by considering the objective of minimizing the number of interconnections among processes.

REFERENCES

[1] H. H. Chin, P. Y. Liew, P. S. Varbanov, J. J. Klemeš, Chem. Eng. Sci. 248 (2022), 117223. https://doi.org/10.1016/j.ces.2021.117223.

[2] F.S. Francisco, M. Bavar, F.L.P. Pessoa, E M. Queiroz, H. Asgharnejad, M.H. Sarrafzadeh, J. Water Process Eng. 47 (2022) 102758. https://doi.org/10.1016/j.jwpe.2022.102758.

[3] H.P. Zhao, X.Y. Fan, Z.Y. Liu, Chem. Eng. Sci. 91(2013), 162–172, 2013. https://doi.org/10.1016/j.ces.2013.01.025.

[4] B.J. Singh, A. Chakraborty, R. Sehgal, J. Environ. Manage 348 (2023) 119230. https://doi.org/10.1016/j.jenvman.2023.119230.

[5] É. Hansen, M.A.S. Rodrigues, M.E. Aragão, P.M. de Aquim, J. Clean. Prod. 172 (2018) 1814–1822. https://doi.org/10.1016/j.jclepro.2017.12.005.

[6] D.C. de Faria, A.A. Ulson de Souza, S.M. de A. Guelli Ulson de Souza, J. Clean. Prod. 17 (9) (2009) 857–862. https://doi.org/10.1016/j.jclepro.2008.12.012.

[7] T. Budak Duhbacı, S. Özel, S. Bulkan, J. Clean. Prod. 284 (2021) 124752. https://doi.org/10.1016/j.jclepro.2020.124752.

[8] W. Zhao, T. H. Beach, Y. Rezgui, IEEE Trans. Syst. Man. Cybern. Syst. 46(5) (2015) 659–681. https://ieeexplore.ieee.org/document/7185445.

[9] M. Souifi, A. Souissi, Mater. Today Proc.13 (2019) 1115–1124. https://doi.org/10.1016/j.matpr.2019.04.079.

[10] F. Boukouvala, R. Misener, C. A. Floudas. Eur. J. Oper. Res. 252(3) (2016) 701–727. https://doi.org/10.1016/j.ejor.2015.12.018.

[11] K. Nemati Amirkolaii, H. Romdhana, M.L. Lameloise, Sustainability 11(16)(2019) 4492. https://doi.org/10.3390/su11164492.

[12] G.K.C. Ding, Encycl. Sustain. Technol. (2017) 43–52. https://doi.org/10.1016/B978-0-12-409548-9.10170-8.

[13] C. Pan, J. Shi, Z. Liu, AIChE J. 58(2) (2012) 456–465. https://doi.org/10.1002/aic.12595.

[14] M. Gutterres, P.M. de Aquim, in Wastewater Reuse and Management, S. Sharma, R. Sanghi (Eds.). Springer, Dordrecht (2012), p. 127–164. https://doi.org/10.1007/978-94-007-4942-9_5.

[15] E. Mehregan, A. Mahmoudi, Medbiotech J.4(1) (2020) 8–12. http://www.medbiotech.net/article_105333.html.

[16] N. Ibrić, E. Ahmetović, Z. Kravanja, I.E. Grossmann, Energy 235 (2021) 121354. https://doi.org/10.1016/j.energy.2021.121354.

[17] W.C. Kuo, R. Smith, Process Saf. Environ. Prot.76(2) (1998) 94–114. https://doi.org/10.1205/095758298529399.

[18] Z.Y. Liu, Y.M. Li, Z.H. Liu, Y.J. Wang, AIChE J. 55(6) (2009) 1628–1633. https://doi.org/10.1002/aic.11748.

[19] D.C. Faria, M.J. Bagajewicz, AIChE J. 56(3) (2010) 668–689. https://doi.org/10.1002/aic.11983.

[20] Z. Liu, Y. Yang, L. Wan, X. Wang, K. Hou, AIChE J. 55(2) (2009) 374–382. https://doi.org/10.1002/aic.11693.

AZZA MOHAMED KHALIFA[1]
NADIA ALI ELSAYED[2]
MOSTAFA AWAD[3]

General Authority of Import and Export, Suez, Egypt

Department of Refining and Petrochemical Engineering, Faculty of Petroleum and Mining Engineering, Suez University, Suez, Egypt

NAUČNI RAD

KOMPARATIVNA ANALIZA MINIMIZACIJE VODOVODNE MREŽE U INDUSTRIJSKIM PROCESIMA: REGENERACIONA NASPRAM NEREGENERACIONE METODA

Korišćenje metode regeneracije u vodovodnim mrežama pruža izrazitu korist efektivnim smanjenjem upotrebe sveže vode i ispuštanjem otpadnih voda; istovremeno sprečavajući akumulaciju zagađivača. Ključno je primeniti odgovarajuće strategije razlaganja procesa. U ovom radu, primarni cilj je da se analizira disparitet između vodovodnih mreža koje uključuju jedinicu za regeneraciju i onih koje nemaju. Osim što se bavi primarnim ciljem minimiziranja upotrebe slatke vode, ova studija se fokusira na ispitivanje uticaja različitih procesa dekompozicije i strategije smanjenja potrošnje slatke vode korišćenjem dijagrama koncentracije-masenog opterećenja kao alata za analizu. Štaviše, istražuje se pristup za određivanje privremenih koncentracija u sistemima vode sa više kontaminanata tokom procesa razlaganja koncentracije. Kroz smanjenje potrošnje slatke vode, protoka regenerisane vode i opterećenja regeneracije zagađivača, cilj je da se minimizira ukupni uticaj na slatkovodne resurse i csintetiše optimalno dizajnirana mreža za reciklažu vode za regeneraciju. Pruženi su dokazi o izvodljivosti i efikasnosti predloženog pristupa prikazujući tri studije slučaja. Rezultati odabranih primera ukazuju na to da su dizajni ostvareni ovim radom uporedivi sa onima koji se nalaze u postojećoj literaturi.

Ključne reči: uklanjanje kontaminanata; matematičko modeliranje; optimizacioni algoritmi; metode regeneracije; minimizacija vodovodne mreže.

CI&CEQ
Chemical Industry & Chemical Engineering Quarterly

Available online at
Association of the Chemical Engineers of Serbia *AChE*
www.ache.org.rs/CICEQ

Chem. Ind. Chem. Eng. Q. 31 (4) 295–304 (2025) CI&CEQ

MILENA ŽUŽA PRAŠTALO[1]
NIKOLA MILAŠINOVIĆ[2]
MARKO JONOVIĆ[3]
MELINA KALAGASIDIS-KRUŠIĆ[4]
ZORICA KNEŽEVIĆ-JUGOVIĆ[1]

[1]Department of Biochemical Engineering and Biotechnology, Faculty of Technology and Metallurgy, University of Belgrade, Belgrade, Serbia

[2]Department of Forensic Sciences, Faculty of Forensic Sciences and Engineering, University of Criminal Investigation and Police Studies, Belgrade, Serbia

[3]Institute of Chemistry, Technology and Metallurgy, University of Belgrade, Belgrade, Serbia

[4]Department of Organic Chemical Technology, Faculty of Technology and Metallurgy, University of Belgrade, Belgrade, Serbia

ALCALASE IMMOBILIZATION ONTO CHITOSAN/GLUTARALDEHYDE/TRIPOLYPHOSPHATE BEADS OBTAINED BY INVERSE EMULSION TECHNIQUE

Article Highlights

- Alcalase was covalently immobilized onto chitosan beads obtained by inverse emulsion technique
- The beads were additionally cross-linked by immersion in tripolyphosphate solution
- The beads had a sufficient amount of attachment points for enzyme immobilization
- The additional cross-linking resulted in smaller beads and higher specific activity of the enzyme
- The immobilized alcalase could potentially be used for several industrial applications

Abstract

Enzymes immobilization can efficiently solve limitations of their large-scale application, such as stability and reusability. In this study, Alcalase® 2.4L (protease from Bacillus licheniformis) was covalently immobilized onto chitosan beads obtained by inverse emulsion technique using 1.5% (m/v) of chitosan and 0.67% (v/v) or 1.0% (v/v) of glutaraldehyde (CTPP (1.5/0.67) and CTPP (1.5/1.0)). Afterward, the beads were additionally crosslinked by immersion into 10 % (m/v) tripolyphosphate solution. The parameters studied were enzyme loading, enzyme coupling yield, bead diameter, SEM, biocatalyst activity, and FTIR. The beads had adequate enzyme loading and enzyme coupling yield (Pg_{max} was 117.1 mg/g dry CTPP 1.5/0.67 and 90.1 mg/g dry CTPP 1.5/1.0, and μ_{max} was 96.7% for both carriers). CTPP (1.5/1.00) beads were smaller (diameter 635.2 ±25.2 mm wet/ 230.4±12.5 mm dry beads) and showed a higher specific activity of 20.1 ± 0.23 $IU/mg_{protein}$. The immobilized Alcalase® 2.4L was tested for hydrolyzing egg white and soy proteins. Alcalase® 2.4L, covalently attached to CTTP (1.5/1.0) chitosan beads, is a promising choice for industrial processes involving egg white protein hydrolysis, as the enzyme achieved a notable hydrolysis rate of 26.34 ± 0.879% after 195 minutes. Additionally, it remained effective through five successive applications under practical conditions (50 °C, pH 8).

Keywords: Alcalase® 2.4L; covalent immobilization; inverse emulsion technique; chitosan beads; tripolyphosphate.

SCIENTIFIC PAPER

UDC 577.15:66:544.773.3

Alcalase® 2.4L, a non-specific serine-type endoprotease from *Bacillus licheniformis*, is a commercial enzymatic preparation consisting of several proteinases (mainly of subtilisin A) with different specificities [1,2]. The enzyme has been used for various purposes such as detergent, dairy, silk, soy processing, brewing industries applications, production of hydrolysates, chemo-enzymatic synthesis, and others [3–5]. Free enzymes have several disadvantages such as high product cost, poor stability, and inability to be used in continuous production [6]. Enzyme immobilization increases its usability and stability and facilitates product separation and catalyst recycling [7–9]. Enzyme immobilization methods include cross-linking, encapsulation, entrapment,

---

Correspondence: M.Ž. Praštalo, Department of Biochemical Engineering and Biotechnology, Faculty of Technology and Metallurgy, University of Belgrade, Karnegijeva 4, 11000 Belgrade, Serbia.
E-mail: mzuza@tmf.bg.ac.rs

Paper received: 1 April, 2024
Paper revised: 29 September, 2024
Paper accepted: 6 December, 2024

https://doi.org/10.2298/CICEQ240401037Z

adsorption, and covalent binding. The choice of immobilization method and support depends on the intended use of the enzyme, the nature of the support, and the simplicity of the method [6]. The covalent binding of enzymes to the support provides improved stability and reduces enzyme leaching [8–11]. Alcalase® 2.4L has been immobilized using different methods and supports, such as glyoxyl- and monoaminoethyl-N-aminoethyl- agarose beads, hollow core-mesoporous shell silica nanospheres unmodified or modified with various metal ions, chitosan beads activated with different agents (such as glutaraldehyde, glyoxyl, and divinyl sulfone), chitosan-coated Fe_3O_4 nanoparticles, sol-gels, silica supports, alginate micron and submicron beads [3–5,12–22]. Chitosan is produced as a by-product through the alkaline deacetylation of chitin, a process in which the amide group in chitin is hydrolyzed to form a primary amine group (R-NH_2), resulting in chitosan. Chitosan has been one of the most promising renewable biopolymers due to its properties such as biocompatibility, biodegradability, non-toxicity, ability to be easily modified, and low cost. Chitosan's lack of toxicity and its rapid degradability make it ideal for various environmental and agricultural applications. It is used in drug delivery within the human gastrointestinal tract, food processing, biomedical fields, cosmetics, enzyme immobilization, as a heterogeneous catalyst, a sorbent for organic and inorganic contaminants, antimicrobial products, and for uranium recovery [23–27]. In this paper, for the first time, Alcalase® 2.4L was covalently immobilized onto different types of chitosan beads obtained by the emulsion technique, crosslinked with glutaraldehyde (GA) and then, additionally cross-linked by immersion into tripolyphosphate (TPP) solution. TPP is a multivalent anion and a non-toxic ionic cross-linker that interacts with the cationic chitosan forming ionically crosslinked networks through electrostatic forces [28]. TPP is especially appealing as an ionic crosslinker due to its stable performance, straightforward process control, and safety benefits [29]. The mechanical strength of chitosan beads crosslinked with only TPP is somewhat limited, but it can be improved by coating them with a negatively charged polymer, to create a polyelectrolyte complex film, or by employing covalent crosslinking [30]. The immobilized enzyme is potentially recycled, can be easily separated without contaminating a final product, can reduce the costs of downstream processing, has better stability, etc. The effects of chitosan bead properties on enzyme binding capacity, immobilization yield, and immobilized enzyme activity were investigated and the results were compared. The Alcalase® 2.4L immobilized to CTTP (1.5/1.0) chitosan bead was subsequently utilized in the industrial-scale hydrolysis of egg white and soy proteins. The degree of hydrolysis achieved was measured and compared to that obtained with the free enzyme.

In the literature, there are no studies of chitosan beads obtained by inverse emulsion technique, firstly cross-linked with GA and afterward immersed into TPP for additional cross-linking. Current enzyme immobilization methods have specific limitations, particularly in terms of stability, reusability, and efficiency when using conventional materials and techniques. Our approach, using novel chitosan beads, offers a potential solution to these limitations. Likewise, there are only a few studies on the use of immobilized Alcalase® 2.4L for the hydrolysis of egg white and soy proteins.

MATERIALS AND METHODS

Materials

Alcalase® 2.4L (protease from *Bacillus licheniformis*, Subtilisin EC 3.4.21.14) was provided by Sigma-Aldrich (*St Louis, MO,* USA). Chitosan (Ch) and tripolyphosphate (TPP) were obtained from Sigma, Japan, while itaconic acid (2-methylidenebutanedioic acid) was purchased from Sigma Aldrich, Germany. Glutaraldehyde (GA) (pentane-1,5-dial) and paraffin oil (light liquid paraffin) were obtained from Centrohem, Serbia. Tween 80 (polyoxyethylene (20) sorbitanmonooleate) used as an emulsifier was obtained from Riedel-de Haën, Germany. Azo-casein and sodium tripolyphosphate (TPP) were purchased from Sigma Chemical Co. (St. Louis, MO). Chicken egg whites obtained from a local supermarket were separated from the yolk and gently stirred without foam formation to provide a homogeneous mixture. Soy protein isolates with a protein content of 90% were received from Sojaprotein, Serbia. All other chemicals used in this research were of analytical grade.

Preparation and activation of chitosan microbeads

Emulsion technique

Chitosan microbeads were prepared by applying the emulsion technique, with the addition of GA, as a crosslinking agent as previously described [5], with some modifications. The aqueous phase was prepared by adding chitosan (1.5% (m/v)) in 5 mL of acetic acid solution (2.0% (v/v)). Water and oil phases (50 mL of paraffin oil) were mixed in a 1:10 ratio using a magnetic stirrer (Heidolph Hei-Connect, Germany), with the addition of 1.0% (v/v) Tween 80 (0.5 mL) as an emulsifier at room temperature and at stirring speed of 750 rpm. After homogenization, GA solution (0.67% or 1.0% (v/v)) was added, drop-by-drop, and stirring was continued under the same conditions for the next 24 h. To remove all residues of the surfactant, the microbeads were washed out thoroughly with plenty of water, ethanol, and petroleum ether in three cycles, respectively. Afterwards, the obtained beads were submerged in 10% (m/v) TPP solution at room temperature for the next 24 h and subsequently thoroughly washed with water. The microbeads were dried in the oven at 37 °C for 48 h until constant mass was achieved, and kept until further use in a desiccator at 25 °C.

The samples were labeled as CTPP(Ch/GA), where two numbers correspond to the chitosan concentration (m/v%) and the concentration of the GA (v/v%). For example, CTPP (1.5/0.67) - means chitosan beads obtained by inverse emulsion technique using 1.5% (m/v) of chitosan and 0.67% (v/v) of glutaraldehyde, afterward immersed into 10% (m/v) tripolyphosphate solution.

Bead size

Data related to bead size were obtained using an optical microscope Olympus CX41RF, equipped with picture analyzing software "CellA" (Olympus, Tokyo, Japan). Microbeads were examined immediately after formation (native microbeads), in a dry and rehydrated state.

Scanning Electron Microscopy

The effect of Alcalase® 2.4L on the surface morphology of chitosan microbeads was examined using a TESCAN Vega TS 5130MM scanning electron microscope (Brno, Czech Republic) at different magnifications. SEM analysis was performed at 10.0 kV.

Immobilization method

The beads were treated with 1% (v/v) GA in 0.1M phosphate buffer at pH 8.0 and 28 °C for 30 min under gentle stirring. The excess of GA was then washed out using distilled water until no absorbance was read at 280 nm, confirming the absence of GA.

Enzyme coupling solution containing different amounts of Alcalase® 2.4L was prepared in 0.1 M phosphate buffer at pH 8.0 and pre-incubated at 28 °C under stirring for 2 h. After this period, activated microbeads (1 g wet weight) were submerged into the enzyme solution for 22 h at 28 °C under gentle stirring (120 rpm). At the end of this period, Ch/GA/TPP-Alcalase® 2.4L conjugate was formed (Fig. 1). Afterwards, sodium borohydride was added (0.5 mg $NaBH_4$/mL of solution) to reduce the Schiff's bases and the remaining aldehyde groups [31]. After 30 min at 4 °C under mechanical stirring, the produced derivative was washed with 0.1 M sodium phosphate buffer, pH 8.0, followed by washing with distilled water after which it was stored at 4 °C in 0.1 M sodium phosphate buffer, pH 8.0 before being used.

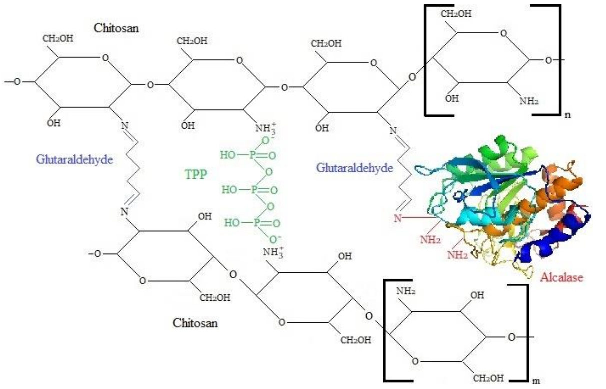

Figure 1. Chemical structure of the Alcalase® 2.4L conjugate formed with chitosan, glutaraldehyde, and tripolyphosphate. The 3-D structure was obtained from Protein Data Bank 1SCB using Pymol.

Samples of the enzyme solution before and after the immobilization, together with the washing solutions, were taken for protein content and enzyme activity determination. Alcalase® 2.4L concentration was determined according to the Bradford method using bovine serum albumin (BSA) as a standard [32]. The amount of bound enzyme was determined indirectly from the difference between the amount of enzyme introduced into the coupling reaction mixture and the amount of enzyme in the filtrate and the washing solutions:

$$\eta_{enz} = \frac{P_1}{P_0} \cdot 100 \tag{1}$$

where P_1 is the immobilized amount of Alcalase® 2.4L and P_0 is the initial amount of Alcalase® 2.4L in the enzyme coupling solution determined by the Bradford method. All experiments were carried out in triplicate. The efficiency of immobilization was evaluated in terms of enzyme coupling yield.

Alcalase activity assay

The Alcalase® 2.4L activity was measured using azo-casein as a substrate [33]. Assay mixture containing 75 µL of the enzyme solution or different mass of immobilized Alcalase® 2.4L (0.01 to 0.2 g) and 125 µL of 2% (m/v) azocasein in 50 mM Tris-HCl (pH 9.0) was incubated for 30 min at 37°C. The reaction was terminated by the addition of 600 µL of 10% (m/v) trichloroacetic acid. To remove the resulting precipitate, the assay tubes were cooled down in an ice bath prior to centrifugation for 10 min at 8000 rpm. Subsequently, 600 µL of supernatant was added to 700 µL 1 M NaOH and the absorbance at 440 nm was measured against a reference tube prepared separately for each sample by the addition of trichloroacetic acid stop solution immediately after mixing the enzyme solution with the substrate. One unit of Alcalase® 2.4L activity was defined as the amount of enzyme required to produce an increase in absorbance at 440 nm of 1.0 in a 1-cm cuvette, under the above-mentioned assay conditions. All measurements were done in three repetitions.

Fourier transform infrared spectroscopy analysis

Fourier transform infrared spectroscopy (FT-IR) of dry samples was performed using Bomem MB 100 FT-IR spectrophotometer, applying the KBr disc method. Test samples consisted of 1 mg of sample mixed and ground with 50 mg of potassium bromide and compressed into pallets at a pressure of 11 t for about a minute, using a Graseby Specac model: 15.011. The spectra were obtained in the wave number range between 4000 and 400 cm^{-1} at 25 °C and at 4 cm^{-1} spectral resolution. All experiments were carried out in triplicate.

Hydrolysis of egg white protein and soya protein isolate with free alcalase and immobilized alcalase

The activity of free and immobilized alcalase in the industrially feasible reactions was assayed by monitoring the hydrolysis of 1% (w/w) soy protein isolate aqueous solution (2.4 mg/mL, protein content) and 10% (w/w) aqueous solution of pretreated egg white (11.4 mg/mL, protein content determined according to the standard Kjeldahl method, N 9 6.25). The hydrolysis was carried out in a 600 mL mechanically stirred batch reactor with temperature and pH control. Prior to the enzymatic hydrolysis, the egg white protein solution was subjected to thermal pretreatment at a high temperature (75 °C) for half an hour and afterward, the solution was kept out at an ambient temperature to cool. After pH and temperature stabilization (about 20 min) at optimum conditions for protease (50 °C and pH 8.0), the hydrolysis reaction was initiated by adding 2.12 and 0.11 IU of the free enzyme and the equivalent amount of the immobilized enzyme into egg white and soy protein solution, respectively, with stirring at 240 rpm. During the reaction, pH was kept at a constant value by adding 0.2 M NaOH, using the pH-stat method with automatic dosage of the base. The reaction was stopped by heating the mixture at 90 °C for 15 min to inactivate the free enzyme. In the case of the immobilized alcalase, the biocatalyst was removed by filtration, washed with plenty of water, and repeatedly recycled to examine its reusability.

Determination of hydrolysis degree

The progress of the enzymatic hydrolysis was followed by monitoring the hydrolysis degree through the pH-stat method. The hydrolysis degree was calculated as follows [34]:

$$DH(\%) = \frac{h \cdot 100}{h_{tot}} = \frac{N_b \cdot B \cdot 100}{\alpha \cdot m_p \cdot h_{tot}} \tag{2}$$

where h is the number of equivalents of peptide bonds hydrolyzed at the time per weight unit, h_{tot} is the total amount of peptide bonds per weight unit of a protein and can be calculated from its amino acid composition, N_b is the normality of the base, B is the consumption of the base in mL, and α is the degree of dissociation of the α-amino groups (1/α = 1.13 at 50 °C and pH 8.0), and m_p is the mass of protein in g. The degree of conversion (*DH*) was defined as the ratio of the cleaved peptide bonds to the total amount of peptide bonds.

Statistical analysis

All experiments were performed in triplicate and the data are presented in average of triplicates and standard deviation (*SD*). Statistical differences were determined by one-way analysis of variance (ANOVA). A Tukey test was applied as a test a posteriori with a level of significance of 95%. All the tests were considered statistically significant at $p < 0.05$. Statistical analysis was performed using the Origin Pro 8 software package.

RESULTS AND DISCUSSION

Alcalase® 2.4L immobilization

As the enzyme loading capacity is an important feature that affects the support price of the final catalysts [35] the total protein loading and the enzyme coupling yields were investigated. The Alcalase® 2.4L concentration was varied in the range of 0.1–1.68 mg/mL and 0.5 g of the wet chitosan beads CTPP (1.5/0.67) or CTPP (1.5/1.0) was immersed in 10 mL of enzyme coupling solution. The results are shown in Fig. 2.

The increase of the initial enzyme concentration in the coupling solution resulted in a linear increase of the enzyme loading on support (Figure 2). The result can be explained by the proportional binding of enzyme molecules to available sites on the support, assuming the support has excess binding sites and is not saturated with the enzyme [36]. The immobilization onto CTPP (1.5/0.67) provides a higher loading of protein than that on CTPP (1.5/1.0). The maximum amount of the Alcalase® 2.4L bound (Pg_{max}) was 117.1 mg/g dry support and 90.1 mg/g dry support, respectively. In the literature, other authors reported lower or comparable Pg_{max} values of Alcalase® 2.4L

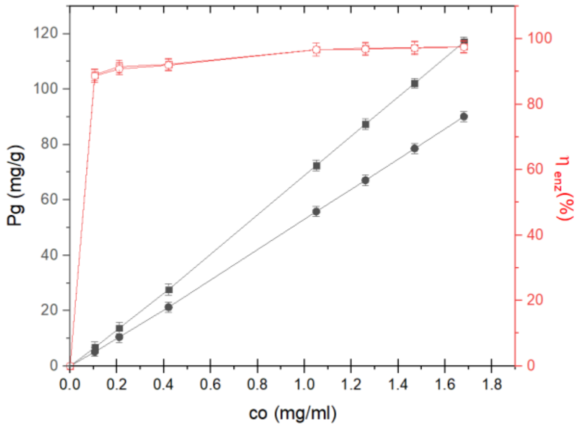

Figure 2. Impact of initial enzyme concentration on Alcalase® 2.4L loading and coupling yield for chitosan/glutaraldehyde/tripolyphosphate beads (CTTP) with different cross-linker ratios (Alcalase 2.4L loading: CTPP (1.5/0.67) (■), CTPP (1.5/1.0) (●) beads and enzyme coupling yield: CTPP (1.5/0.67) (□), CTPP (1.5/1.0) (○) beads). (c_o-initial enzyme concentration in coupling solution, Pg-enzyme loading, η_{enz}-enzyme coupling yield).

immobilized onto different supports. Thus, Zhu *et al.* and Zeng *et al.*, based on metal ion affinity chromatography immobilized Alcalase® 2.4L using triamino-functionalized hollow mesoporous silica spheres modified with various metal ions (Fe^{3+}, Ca^{2+}, Cu^{2+}, Ni^{2+}, Zn^{2+}) and obtained Alcalase® 2.4L loading capacity of 33.7-119.3 mg/g and 124.5 to 227.8 mg/g, respectively. [19,22] Corîci *et al.* immobilized Alcalase® 2.4L in dimethyldimethoxysilane (DMDMOS)-containing sol-gel system and attained the optimum capacity for enzyme loading in the silica matrix of 115 mg of protein per g of dry xerogel [37]. Ferreira *et al.* covalently immobilized Alcalase® 2.4L onto two sets of chemically distinct silica supports presenting terminal amino (S_{APTES}) or hydroxyl groups ($S_{TESPM\text{-}pHEMA}$) and achieved the loading of 2.4–6.3 mg of protein per gram of silica [38]. Zuza *et al.* immobilized Alcalase® 2.4L onto different types of chitosan beads obtained by electrostatic extrusion and inverse emulsion techniques, cross-linked only with glutaraldehyde, achieved the enzyme loading in the range of 116.3 to 340.2 mg/g [5]. Jonovic *et al.* immobilized Alcalase® 2.4L on alginate micron and submicron beads and obtained excellent maximum enzyme bounding of 592.3 mg/g [21]. Therefore, the obtained supports have an adequate content of attachment points for enzyme immobilization.

It can be noticed that the enzyme coupling yield also increased as the initial enzyme concentration was increased to 1.05 mg/mL and leveled off at about 96.7% for both carriers. Therefore, the beads have satisfactory enzyme coupling yield and the enzyme coupling yields were less influenced by the initial Alcalase® 2.4L concentration than the enzyme loading on supports. This can be attributed to the effective use of available binding sites on the support. As long as the support is not saturated and there are sufficient binding sites, the proportion of enzyme-coupled yield remains relatively stable, while enzyme loading increases proportionally with enzyme concentration [36].

As more enzyme was loaded onto the support, the specific activity of the immobilized Alcalase® 2.4L increased, reaching a maximum value A_{max} of 17.3 ± 0.34 IU/mg$_{protein}$ and 20.1 ± 0.23 IU/mg$_{protein}$ for CTPP (1.5/0.67) and CTPP (1.5/1.00), respectively (data not shown). These activities are higher than the activity of Alcalase® 2.4L immobilized to silicas with large pores and $S_{TESPM\text{-}pHEMA}$ (2.2–6.7 IU/mg$_{protein}$), glass sol-gel matrices (3.49-9.91 IU/mg$_{protein}$), chitosan beads obtained by emulsion technique cross-linked with GA S(1.5/0.67) (12.5 IU/mg$_{protein}$) and S(1.5/1.00) (16.3 IU/mg$_{protein}$) and lower than activity of Alcalase® 2.4L immobilized to S(2.0/0.57) (21.5 IU/mg$_{protein}$), EE (23.6 IU/mg$_{protein}$), S_{APTES} (17.9-40.3 IU/mg$_{protein}$) and glyoxyl- and glutaraldehyde-agarose bead (28.4–55.3 IU/mg$_{protein}$) [5,37–39]. Further increase of initial Alcalase® 2.4L concentrations and/or enzyme loading did not result in higher activities for the immobilized enzyme. As enzyme loading increases, the availability of enzyme molecules grows, leading to higher specific activity as more active sites participate in catalysis. As enzyme loading continues to increase, specific activity reaches a maximum due to factors such as saturation of the support's binding capacity, possible enzyme aggregation, and diffusion limitations [36].

Selected CTPP (1.5/0.67) beads in the relaxed polymer state are shown in Fig. 3. Average diameters of chitosan beads were 1008.8 ± 223.3 mm wet/ 288.8±54.2 mm dry CTPP (1.5/0.67) beads and 635.2±25.2 mm wet/ 230.4±12.5 mm dry CTPP (1.5/1.00) beads. Thus, the GA content increase led to a decrease in the size of the beads. The beads were smaller than chitosan beads obtained by inverse emulsion technique using the same chitosan and GA concentration and crosslinked only with glutaraldehyde (S (1.5/0.67), S (1.5/1.00)) [5]. Therefore, additional crosslinking with TPP leads to a bead size decrease. The smaller chitosan beads for the Alcalase® 2.4L immobilization yield higher activity because the surface area per unit mass of smaller beads is larger than that of larger beads. Hence, the enzyme immobilized onto CTPP (1.5/0.67) and CTPP (1.5/1.0) had higher activity (17.3±0.34 IU/mg$_{protein}$ and 20.1±0.23 IU/mg$_{protein}$, respectively) than the enzyme immobilized onto S (1.5/0.67) and S (1.5/1.0) (12.5 IU/mg$_{protein}$ and 16.3 IU/mg$_{protein}$, respectively).

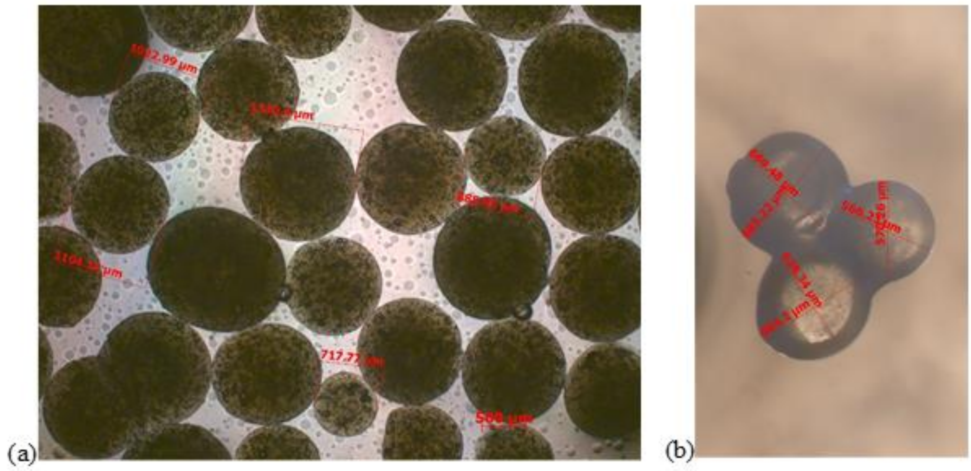

Figure 3. Images obtained by optical microscopy of chitosan/glutaraldehyde/tripolyphosphate beads a) (CTTP) (1.5/0.67) and b) (CTTP) (1.5/1.0) beads in their relaxed state. At a magnification of 10X.

SEM analysis

Figure 4. presents the SEM results of CTPP beads and CTPP beads after Alcalase® 2.4L immobilization. The Figure shows that the surface of the pure beads was smooth and uniform. After GA treatment and the enzyme immobilization, the roughness of the bead surface increased and the bead had rounded structures that may be attributed to protein aggregates after Alcalase® 2.4L immobilization [40,41].

We studied the effects of the mass of the biocatalysts obtained by varying initial enzyme concentration on the activity of the Alcalase® 2.4L – CTPP(1.5/0.67) and –CTPP(1.5/1.0) chitosan beads. The obtained results (Fig. 5) showed that the biocatalyst activity increased with the mass of the immobilized enzyme to some maximal value and then decreased with a further increase in weight probably due to steric hindrance and diffusion limitations. Within the experimental ranges used (0.33-5.32 IU), the highest activity was shown by the biocatalysts obtained in the system with the highest number of enzyme units 5.32 IU in the coupling solution. Alcalase® 2.4L immobilized onto CTPP(1.5/1.0) and CTPP(1.5/0.67) had higher activity than Alcalase® 2.4L immobilized onto S(1.5/0.67) and S(1.5/1.0), as CTPP beads were smaller in size and the contact surface between the substrate and the Alcalase® 2.4L where the reaction takes place was higher [5].

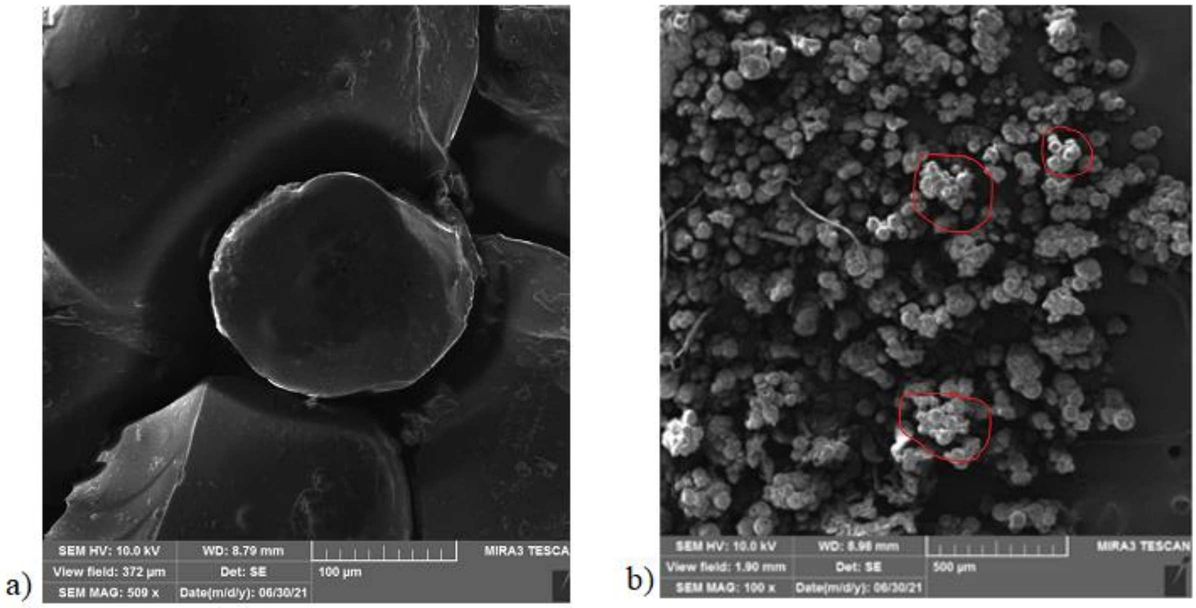

Figure 4. Images obtained by optical microscopy of a) chitosan/glutaraldehyde/tripolyphosphate beads CTPP (1.5/1.0) at a magnification of ×500 and b) chitosan/glutaraldehyde/tripolyphosphate beads CTPP (1.5/1.0) with immobilized Alcalase® 2.4L at a magnification of ×100.

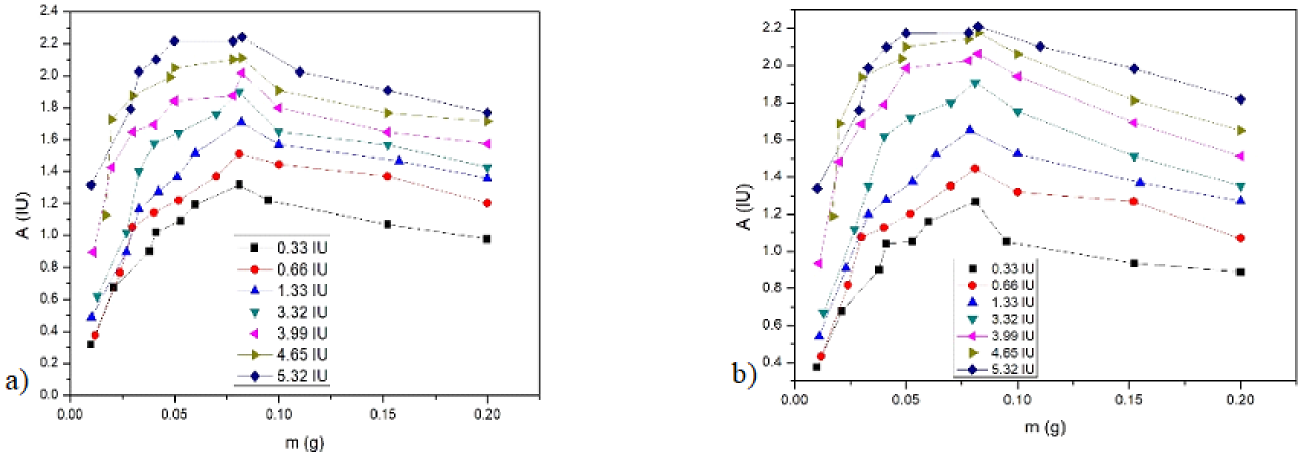

Figure 5. Impact of biocatalyst mass on the activity of Alcalase® 2.4L Immobilized on chitosan/glutaraldehyde/tripolyphosphate beads (CTTP): Comparison Between CTPP (1.5/0.67) and CTPP (1.5/1.0) Cross-Linker Ratios.

Fourier Transform Infrared Spectroscopy analysis

Fourier Transform Infrared Spectroscopy analysis (FT-IR) was performed in the 4000–400 cm^{-1} to confirm relationships between the matrix and enzyme. Figure 6. shows FT-IR spectra of Alcalase® 2.4L (spectrum a), pure CTPP beads spectrum (b); activated CTPP beads spectrum (c); and CTPP beads with immobilized Alcalase® 2.4L spectrum (d). Spectrum (a) shows a strong peak at 1550–1650 cm^{-1} that corresponds to amide I and amide II groups in the protease. The presence of bands in the region around 1350 cm^{-1} indicates the significant CH_2 and CH_3 deformation of the aliphatic amino acids [42]. Spectrum (b), the wide extension peaks observed at 3438 cm^{-1} are attributed to the stretching and bending vibrations of O-H and N-H bonds of chitosan and at 2921 cm^{-1} to CH_3 symmetric stretch. The bands at 1640–1658 cm^{-1} were referenced as amides I and bands in the range between 1390–1380 cm^{-1} correspond to the C-H bending due to the presence of aldehyde. The amide II band was at 1544 cm^{-1}. The bands at 1084 cm^{-1} and 1024 cm^{-1} were groups of C-O-C and C-O (spectrum b) [43–45]. There was no major difference in FTIR profile between pure CTPP beads and activated CTPP beads, indicating that GA and TPP cross-linking slightly hindered chitosan structure. Spectrum (d) shows the characteristic peak for the C=N group at 1664 cm^{-1} which indicates the imine reaction between the aldehyde group of glutaraldehyde and the NH_2 group of the enzyme [18]. It can be noticed that the characteristic peaks of the enzyme at 1110 cm^{-1} (spectrum a) shift the chitosan peak at 1158 cm^{-1} (spectrum b) to 1150 cm^{-1} (spectrum d) probably due to the reaction with GA on the support [46]. A peak at about 541 cm^{-1} indicates characteristic trans-gauche-trans enzyme conformation correlated to the S-S stretching vibrations and is shifted to 548 cm^{-1} upon Alcalase® 2.4L immobilization [5]. The FT-IR data confirmed that the activation of the beads and the subsequent covalent immobilization of the enzyme were carried out successfully. The changes in the FT-IR spectra align with expected chemical interactions, validating the effectiveness of the process. Therefore, we assume that the process of the bead activation with GA and Alcalase® 2.4L covalent immobilization was successful.

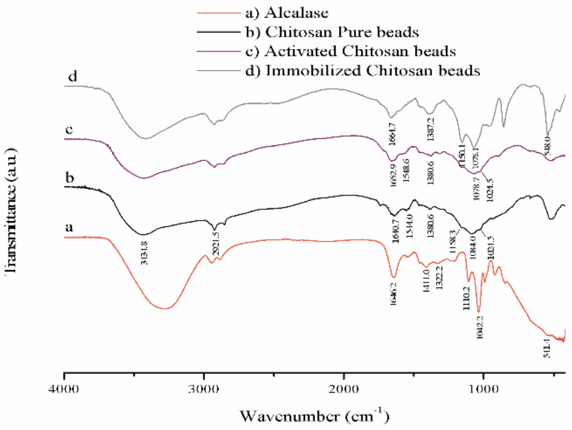

Figure 6. FT-IR spectra of investigated samples: (a) Alcalase® 2.4L (b) pure chitosan/glutaraldehyde/tripolyphosphate beads; (c) activated chitosan/glutaraldehyde/tripolyphosphate beads; and (d) chitosan/glutaraldehyde/tripolyphosphate beads with immobilized Alcalase® 2.4L.

Hydrolysis of egg white and soy proteins

The effectiveness of Alcalase® 2.4L immobilized on CTTP (1.5/1.0) chitosan beads for proteolysis of egg white and soy proteins has also been assessed. Figure 7. illustrates how the degree of hydrolysis (DH) changes over time for the immobilized enzyme at 50 °C. Free Alcalase® 2.4L reached the degrees of hydrolysis off egg white and soy protein of 35.10±1.125 at 75 min and 25.64±0.87 at 120 min [5], while the immobilized Alcalase® 2.4L achieved 18.06±0.963 at 75 min and 11.52±0.987 at 120 min, respectively.

Hydrolysis using free Alcalase® 2.4L proceeded quickly at the beginning but then slowed down, eventually leveling off after 75 min and 120 min for egg white and soy protein, respectively [5]. In contrast, hydrolysis with immobilized Alcalase® 2.4L was more gradual, reaching a plateau after 150-195 minutes.

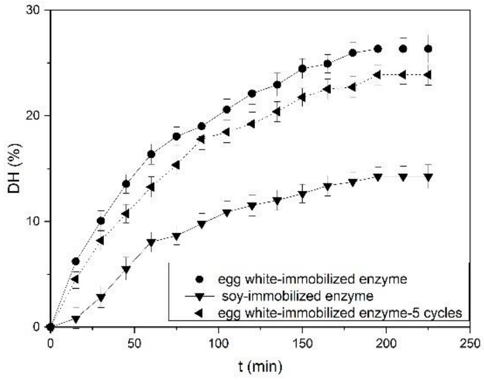

Figure 7. Enzymatic progress curves of hydrolysis of egg white protein and soy protein isolate with alcalase immobilized on CTTP (1.5/1.0) chitosan beads,

The initial rate of free and immobilized enzyme was 0.834 and 0.414, and 0.237 and 0.056 DDH%/min (it was decreased 2.01- and 4.23-fold) for egg white and soy, respectively. Therefore, the immobilization of the enzyme negatively affected the initial rate. Conversely, although the maximum degree of hydrolysis reached with the immobilized enzyme was lower compared to the free enzyme, it is still considered satisfactory (35.09±1.125 and 26.34±0.989, and 25.64±0.875 and 14.25±0.968 for hydrolysis of egg white and soy protein with free and the immobilized, respectively) [5]. Overall, the immobilized enzyme performs significantly better in egg white compared to soy protein hydrolysis, considering both, the degree of hydrolysis and the initial hydrolysis rate. Alcalase® 2.4L immobilized on CTTP (1.5/1.0) chitosan beads exhibited somewhat lower effectiveness compared to Alcalase® 2.4L immobilized on EE chitosan beads, which achieved maximum degrees of hydrolysis of 30.28 ± 1.107% for egg white and 16.38 ± 0.989% for soy protein. Additionally, Alcalase® immobilized on magnetic chitosan nanoparticles reached a maximum degree of hydrolysis of 18.38% for soy protein isolate [5, 18].

The immobilized Alcalase® 2.4L was then used for egg white hydrolysis in five successive cycles. It was obtained that the activity dropped only about 10% after five reaction cycles. Further, the activity progressively decreased, likely due to factors such as product inhibition, denaturation, and enzyme leakage.

CONCLUSION

The paper presents the covalent immobilization of Alcalase® 2.4L onto new chitosan beads obtained by the emulsion technique, crosslinked with glutaraldehyde and for the first time, additionally crosslinked with tripolyphosphate solution. The results showed that the beads had sufficient content of attachment points for the enzyme immobilization as they had satisfactory enzyme loading and coupling yield. It was confirmed that additional crosslinking led to smaller beads and subsequently the immobilized enzyme had higher specific activity. The Alcalase® 2.4L immobilization onto CTPP beads was also confirmed by the FTIR technique. It can be concluded that CTPP beads are promising supports for enzyme immobilization. The Alcalase® 2.4L immobilized onto CTPP beads can be used for egg white proteins hydrolysis in real food systems, as it demonstrated a satisfactory initial rate, a high maximum degree of hydrolysis, and effective reusability over five consecutive cycles.

ACKNOWLEDGEMENT

This work was supported by the Ministry of Science, Technological Development, and Innovation of the Republic of Serbia (Contract No. 451-03-65/2024-03/200135).

NOMENCLATURE

CTPP (1.5/0.67)	chitosan beads obtained by inverse emulsion technique using 1.5% (m/v) of chitosan and 0.67% (v/v) of glutaraldehyde, afterward immersed into 10 % (m/v) tripolyphosphate solution
CTPP (1.5/1.0)	chitosan beads obtained by inverse emulsion technique using 1.5% (m/v) of chitosan and 1.0% (v/v) of glutaraldehyde, afterward immersed into 10 % (m/v) tripolyphosphate solution
Pg	enzyme loading
η	enzyme coupling yield
GA	glutaraldehyde
TPP	tripolyphosphate
Ch	Chitosan
Tween 80	polyoxyethylene (20) sorbitanmonooleate
BSA	bovine serum albumin
S_{APTES}	silica supports presenting terminal amino groups
$S_{TESPM\text{-}pHEMA}$	silica supports presenting terminal hydroxyl group
A	specific activity of the immobilized Alcalase® 2.4L
S (1.5/0.67)	chitosan beads obtained by emulsion technique using 1.5% (m/v) of chitosan and cross-linked with 0.67% (v/v) GA
S (1.5/1.00)	chitosan beads obtained by emulsion technique using 1.5% (m/v) of chitosan and cross-linked with 1.00 % (v/v) GA
EE	chitosan beads obtained by electrostatic extrusion
FT-IR	Fourier Transform Infrared Spectroscopy analysis

REFERENCES

[1] C. Liu, M. Bhattarai, K. S. Mikkonen, M. Heinonen, J. Agric. Food Chem. 67 (2019) 6625–6632. https://doi.org/10.1021/acs.jafc.9b00914.

[2] A. Eberhardt, E. C. López, R. J. Ceruti, F. Marino, E. J. Mammarella, R. M. Manzo, G. A. Sihufe, Int. J. Dairy

Technol. 72 (2019) 573–584. https://doi.org/10.1111/1471-0307.12606.

[3] F. Hussain, S. Arana-Peña, R. Morellon-Sterling, O. Barbosa, S. A. Braham, S. Kamal, R. Fernandez-Lafuente, Molecules. 23 (2018) 3188. https://doi.org/10.3390/molecules23123188.

[4] A. S. S. Ibrahim, A. A. Al-Salamah, A. M. El-Toni, K. S. Almaary, M. A. El-Tayeb, Y. B. Elbadawi, G. Antranikian, Int. J. Mol. Sci. 17 (2016) 184. https://doi.org/10.3390/ijms17020184.

[5] M. G. Žuža, N. Z. Milašinović, M. M. Jonović, J. R. Jovanović, M. T. Kalagasidis Krušić, B. M. Bugarski, Z. D. Knežević-Jugović, Bioprocess Biosyst. Eng. 40 (2017) 1713–1723. https://doi.org/10.1007/s00449-017-1826-7.

[6] Y. Aslan, A. Y. Taher, I. Cavidoğlu, J. Anim. Plant Sci. 28 (2018) 1648–1655. https://www.siirt.edu.tr/dosya/personel/alan-taher-yaseen-ile-makale-siirt-2019226111612272.pdf.

[7] P. J. Allertz, S. Berger, G. Sellenk, C. Dittmer, M. Dietze, K. P. Stahmann, K. Salchert, Catalysts. 7 (2017) 1–21. https://doi.org/10.3390/catal7120359.

[8] R. Plagemann, J. von Langermann, U. Kragl, Eng. Life Sci. 14 (2014) 493–499. https://doi.org/10.1002/elsc.201300115.

[9] M. Planchestainer, D. R. Padrosa, M. L. Contente, F. Paradisi, Catalysts. 8 (2018) 40. https://doi.org/10.3390/catal8010040.

[10] P. Zucca, E. Sanjust, Molecules. 19 (2014) 14139–14194. https://doi.org/10.3390/molecules190914139.

[11] M. G. Žuža, S. Šiler-Marinković, Z. D. Knežević-Jugović, Chem. Ind. Chem. Eng. Q. 13 (2007) 205–210. https://doi.org/10.2298/CICEQ0704205Z.

[12] S. Ait Braham, F. Hussain, R. Morellon-Sterling, S. Kamal, J. F. Kornecki, O. Barbosa, D. E. Kati, R. Fernandez-Lafuente, Biotechnol. Prog. 35 (2019) 1–4. https://doi.org/10.1002/btpr.2768.

[13] L. Molawa, J. Jordaan, J. Limson, D. Brady, Biocatal. Biotransform. 31 (2013) 71–78. https://doi.org/10.3109/10242422.2013.767335.

[14] C. Fenoglio, N. Vierling, R. Manzo, R. Ceruti, G. Sihufe, E. Mammarella, Am. J. Food Technol. 11 (2016) 152–158. https://doi.org/10.3923/ajft.2016.152.158.

[15] T. B. Pessato, N. C. de Carvalho, O. L. Tavano, L. G. R. Fernandes, R. de L. Zollner, F. M. Netto, Food Res. Int. 83 (2016) 112–120. https://doi.org/10.1016/j.foodres.2016.02.015.

[16] Y. Liu, D. Dave, Aquaculture. 548 (2022) 737546. https://doi.org/10.1016/j.aquaculture.2021.737546.

[17] T. A. Siswoyo, N. F. Matra, A. A. Safiera, A. Supriyadi, IJASEIT. 7 (2017) 1315–1321. https://doi.org/10.18517/ijaseit.7.4.936.

[18] S. nan Wang, C. ran Zhang, B. kun Qi, X. nan Sui, L. zhou Jiang, Y. Li, Z. jiang Wang, H. xia Feng, R. Wang, Q. zhi Zhang, Eur. Food Res. Technol. 239 (2014) 1051–1059. https://doi.org/10.1007/s00217-014-2301-1.

[19] H. Zhu, Y. Zhang, T. Yang, D. Zheng, X. Liu, J. Zhang, LWT. 162 (2022) 113505. https://doi.org/10.1016/j.lwt.2022.113505.

[20] P. dos S. Kimberle, M. S. Carolina, I. S. B. Ana, R. B. G. Luciana, Process Biochem. 97 (2020) 27–36. https://doi.org/10.1016/j.procbio.2020.06.019.

[21] M. Jonović, M. Žuža, V. Đorđević, N. Šekuljica, M. Milivojević, B. Jugović, B. Bugarski, Z. Knežević-Jugović, Catalysts. 11 (2021) 1–17. https://doi.org/10.3390/catal11030305.

[22] Q. Zeng, Q. Li, D. Sun, M. Zheng, Front. Bioeng. Biotechnol. 8 (2020) 1–11. https://doi.org/10.3389/fbioe.2020.00565.

[23] Y. Qin, P. Li, Int. J. Mol. Sci. 21 (2020) 499. https://doi.org/10.3390/ijms21020499.

[24] M. Gierszewska-Drużyńska, J. Ostrowska-Czubenko, Prog. Chem. Appl. Chitin Its Deriv. 20 (2015) 43–53. https://doi.org/10.15259/PCACD.20.04.

[25] D. Svirskis, A. Seyfoddin, S. Chalabi, J. H. I. Kim, C. Langford, S. Painter, R. Al-Kassas, Pharm. Dev. Technol. 19 (2014) 571–576. https://doi.org/10.3109/10837450.2013.813539.

[26] M. I. Wahba, Biotechnol. Prog. 34 (2018) 347–361. https://doi.org/10.1002/btpr.2587.

[27] S. K. Yong, M. Shrivastava, P. Srivastava, A. Kunhikrishnan, N. Bolan, Rev Environ Contam Toxicol. 233 (2015) 1–43. https://doi.org/10.1007/978-3-319-10479-9_1.

[28] W. Zeng, H. Hui, Z. Liu, Z. Chang, M. Wang, B. He, D. Hao, Carbohydr Polym. 258 (2021) 117684. https://doi.org/10.1016/j.carbpol.2021.117684.

[29] C. Pan, J. Qian, C. Zhao, H. Yang, X. Zhao, H. Guo, Carbohydr Polym. 241 (2020) 116349. https://doi.org/10.1016/j.carbpol.2020.116349.

[30] S. Durkut, Y. M. Elcin, A. E. Elcin, Artif Cells Blood Substit Immobil Biotechnol. 34 (2) (2006) 263–276. https://doi.org/10.1080/10731190600581866.

[31] M. G. Žuža, B. M. Obradović, Z. D. Knežević-Jugović, Chem. Eng. Technol. 34 (2011) 1706–1714. https://doi.org/10.1002/ceat.201100297.

[32] M. M. Bradford, Anal. Biochem. 72 (1976) 248–254. https://doi:10.1016/0003-2697(76)90527-3.

[33] G. Sarath, R. de la Motie, F. Wagner, in Proteolytic Enzymes: A Practical Approach, R. Beynon, J. Bond Editors, IRL Press, Oxford (1989), 25–56. ISBN 0-19-963058-5/963059-3.

[34] J. Adler-Nissen, Enzymatic hydrolysis of food proteins, Elsevier Applied Science Publishers, London and New York (1989), p 427.

[35] N. S. Rios, S. Arana-Peña, C. Mendez-Sanchez, Y. Lokha, V. Cortes-Corberan, L. R. B. Gonçalves, R. Fernandez-Lafuente, Catalysts. 9 (2019) 576. https://doi.org/10.3390/catal9070576.

[36] R. Austin, Enzyme Immobilization, ED-TECH PRESS, United Kingdom (2018), p. 181.

[37] L. N. Corîci, A. E. Frissen, D. J. Van Zoelen, I. F. Eggen, F. Peter, C. M. Davidescu, C. G. Boeriu, J. Mol. Catal. B: Enzym. 73 (2011) 90–97. https://doi.org/10.1016/j.molcatb.2011.08.004.

[38] L. Ferreira, M. A. Ramos, J. S. Dordick, M. H. Gil, J. Mol. Catal. B: Enzym. 21 (2003) 189–199. https://doi.org/10.1016/S1381-1177(02)00223-0.

[39] P. W. Tardioli, J. Pedroche, R. L. C. Giordano, R. Fernández-Lafuente, J. M. Guisán, Biotechnol. Prog. 19

(2003) 352–360. https://doi.org/10.1021/bp025588n.

[40] U. M. F. de Oliveira, L. J. B. Lima de Matos, M. C. M. de Souza, B. B. Pinheiro, J. C. S. dos Santos, L. R. B. Gonçalves, Appl. Biochem. Biotechnol. 184 (2018) 1263–1285. https://doi.org/10.1007/s12010-017-2622-1.

[41] S. D. Gür, N. İdil, N. Aksöz, Appl. Biochem. Biotechnol. 184 (2018) 538–552. https://doi.org/10.1007/s12010-017-2566-5.

[42] A. K. Sharma, B. A. Kikani, S. P. Singh, Int. J. Biol. Macromol. 153 (2020) 680–696. https://doi.org/10.1016/j.ijbiomac.2020.03.006.

[43] S. Ranjbari, A. Ayati, B. Tanhaei, A. Al-Othman, F. Karimi, Environ. Res. 204 (2022) 111961. https://doi.org/10.1016/j.envres.2021.111961.

[44] B. E. Abdelmalek, A. Sila, A. Haddar, A. Bougatef, M. A. Ayadi, Int. J. Biol. Macromol., 104 (2017) 953–962. https://doi.org/10.1016/j.ijbiomac.2017.06.107.

[45] S. Najavand, M. Habibnejad, A. R. Amani-Ghadim, P. Rahimizadeh, M. Pazhang, Biotechnol. Prog. 36 (2020) 2960. https://doi.org/10.1002/btpr.2960.

[46] M. A. A. Abdella, G. M. El-Sherbiny, A. R. El-Shamy, S. M. M. Atalla, S. A. Ahmed, Bull. Natl. Res. Cent. 44 (2020) 40. https://doi.org/10.1186/s42269-020-00301-3.

IMOBILIZACIJA ALKALAZE NA HITOZAN/GLUTARALDEHID/TRIPOLIFOSFAT PERLE DOBIJENE TEHNIKOM INVERZNE EMULZIJE

MILENA ŽUŽA PRAŠTALO[1]
NIKOLA MILAŠINOVIĆ[2]
MARKO JONOVIĆ[3]
MELINA KALAGASIDIS-KRUŠIĆ[4]
ZORICA KNEŽEVIĆ-JUGOVIĆ[1]

[1]Department of Biochemical Engineering and Biotechnology, Faculty of Technology and Metallurgy, University of Belgrade, Belgrade, Serbia

[2]Department of Forensic Sciences, Faculty of Forensic Sciences and Engineering, University of Criminal Investigation and Police Studies, Belgrade, Serbia

[3]Institute of Chemistry, Technology and Metallurgy, University of Belgrade, Belgrade, Serbia

[4]Department of Organic Chemical Technology, Faculty of Technology and Metallurgy, University of Belgrade, Belgrade, Serbia

NAUČNI RAD

Imobilizacija enzima može efikasno da reši ograničenja njihove široke primene, kao što su stabilnost i ponovna upotreba. U ovom radu je enzim Alcalase® 2.4L (proteaza Bacillus licheniformis) kovalentno imobilisan na perle hitozana dobijena tehnikom inverzne emulzije korišćenjem 1,5% (m/v) hitozana i 0,67% (v/v) ili 1,0% (v/v)) glutaraldehida (CTPP (1,5/0,67) i CTPP (1,5/1,0)). Nakon toga, perle su dodatno umrežene uranjanjem u 10% (m/v) rastvor tripolifosfata. Proučavani su opterećenje enzima, prinos enzimskog kuplovanja, prečnik perli, SEM, aktivnost biokatalizatora i FTIR. Perle su imale adekvatno punjenje enzima i prinos enzimskog kuplovanja (P_{gmax} je bio 117,1 mg/g suvog CTPP 1,5/0,67 i 90,1 mg/g suvog CTPP 1,5/1,0, a μ_{max} je bio 96,7% za oba nosača). CTPP (1,5/1,00) perle su bile manje (prečnik 635,2 ±25,2 mm vlažne/230,4±12,5 mm suve perle) i pokazale su veću specifičnu aktivnost od 20,1 ± 0,23 IU/mg proteina. Imobilisani enzim Alcalase® 2.4L je testiran na hidrolizu proteina belanaca i soje. Enzim Alcalase® 2,4L, kovalentno vezan za CTTP (1,5/1,0) hitozan perle, je obećavajući izbor za industrijske procese koji uključuju hidrolizu proteina belanaca, pošto je enzim postigao značajan stepen hidrolize od 26,34 ± 0,879% posle 195 minuta. Pored toga, ostao je efikasan kroz pet uzastopnih primena u praktičnim uslovima (50 °C, pH 8).

Ključne reči: Alcalase® 2.4L; kovalentna imobilizacija; tehnika inverzne emulzije; hitozanske perle; tripolifosfat.

CI&CEQ
Chemical Industry & Chemical Engineering Quarterly

Available online at
Association of the Chemical Engineers of Serbia *AChE*
www.ache.org.rs/CICEQ

Chem. Ind. Chem. Eng. Q. 31 (4) 305–314 (2025) CI&CEQ

CHAO LV[1,2]
YANLONG LIU[2]
ZHANG LU LU[2]

[1]State Key Laboratory of Complex Nonferrous Metal Resources Clean Utilization, Kunming University of Science and Technology, Kunming, Yunnan, China

[2]Key Laboratory of Vibration and Control of Aero-Propulsion System Ministry of Education, Northeastern University at Qinhuangdao, Qinhuangdao, Hebei, China

SCIENTIFIC PAPER

UDC 544:66:546.19

FORECASTING RESEARCH OF MIXING UNIFORMITY OF CERIUM CHLORIDE SOLUTION UNDER MICROWAVE HEATING

Article Highlights

- A simulation model of electromagnetic force inside the tube was established using an energy equation
- Microwaves have thermal and electromagnetic mixing effects
- The model can accurately predict the mixing uniformity of solutions under different conditions

Abstract

Cerium oxide is an important strategic resource and a key raw material for many functional materials in high-tech fields. Microwave heating is an important method to prepare cerium oxide. In the study of cerium oxide prepared by microwave heating, the variation of the polarity factor inside the solution during heating was explored. In addition to thermal effects, microwave heating also exerts electromagnetic influences that promote the mixing of the solution. This study presents both physical experiments and numerical simulations of the mixing behavior of cerium chloride solutions under microwave exposure. The results reveal that under the influence of the microwave electromagnetic field, the mixing uniformity of the solution remains consistent and stable across the entire region. The VMD-SSA-LSTM model was proposed to forecast the mixing uniformity under different process conditions. The results show that the mixing effect of cerium chloride solution under microwave is better than that under conventional heating. The selected forecast model saves time and energy and can accurately forecast the above situation. In addition, the forecast effect is best when the modal number k of VMD decomposition is selected as 3.

Keywords: cerium oxide; physical experiment; numerical simulation; VMD-SSA-LSTM; forecast.

Micro-nano cerium oxide is an important rare earth oxide, which has stable chemical properties, excellent thermal stability, and good safety. It has been applied in food safety detection, food wastewater treatment, and other related fields [1–3]. Micro-nano cerium oxide is cheap, non-toxic, stable in chemical properties, and excellent in oxygen storage and release [4–5]. As an additive, it can also prolong the service life of some specific coating materials [6–7]. In addition, it can improve the denitration efficiency of the catalyst and improve the ability of sulfur resistance and water resistance [8]. Therefore, it also has high research value and wide application in chemical mechanical polishing, fuel cells, medicine [9], and other fields [10–12].

In the preparation of cerium oxide, the microwave is a high-efficiency, non-pollution, non-contact, penetrating, and adsorption selectivity of the bulk heating method [13–17]. In microwave preparation of cerium oxide, the mixing uniformity of reactants has a great influence on the conversion of cerium oxide. Increasing the mixing uniformity of the cerium chloride solution can make the cerium chloride solution contact

---

Correspondence: C. Lv, State Key Laboratory of Complex Nonferrous Metal Resources Clean Utilization, Kunming University of Science and Technology, Kunming 650093, Yunnan, China.
E-mail: lvchao@neuq.edu.cn
Paper received: 12 July, 2024
Paper revised: 27 December, 2024
Paper accepted: 22 January, 2024

https://doi.org/10.2298/CICEQ240712002L

with gas phase materials sufficiently, thus achieving the effect of refining droplets [18–21].

It is time-consuming and laborious to study the mixing effect in the preparation of cerium oxide under different conditions, which often requires a large number of numerical simulations or experiments. How to accurately analyze the mixing of materials in the preparation of cerium oxide and predict the final preparation results through data is particularly important.

In this study, the UDF (User-Defined Function) feature of Fluent was first used to program the formula for the mixing uniformity index. Then, simulations were conducted under different power levels (3–5 kW), liquid concentrations (0.02–0.1), and time intervals (0.8–2.4 s) to obtain the variation of mixing uniformity over time. The simulation results provided high-dimensional time-series data, which were used as input to the proposed VMD-SSA-LSTM model for predicting mixing uniformity and improving preparation efficiency.

In the current context of the rapid development of artificial intelligence, combining machine learning with practical problems has become an effective way to solve complex problems. In forecasting research, Luan [22] put forward the LSTM forecasting model based on VMD. In this paper, the discharge data of Shalizhai Hydrological Station from 2010 to 2019 are predicted, and the forecasting effect is compared with other models. The results show that the VMD-LSTM model can improve the stability of runoff forecasting and reduce the forecasting error; Lu predicted the sales volume of new energy vehicles by fusing the variational modal decomposition (VMD) method and long-term memory neural network (LSTM) model [23]. Firstly, VMD decomposition was used to decompose the data into multiple modal components, and LSTM models were constructed for each component. Finally, more accurate results were obtained by integrating the forecasting status of each component. The research shows that compared with other forecasting models, this method has lower forecasting error and better final effect; Cao built the SSA-LSTM model based on PM 2.5 concentration data in Changsha from May to August 2023 and made comparative experiments with other models [24]. Experimental results show that the goodness of fit (R^2) of the SSA-LSTM model is improved by 45.93%, 31.55%, and 19.12% compared with single LSTM, PSO-LSTM, and WOA-LSTM models, respectively. It can provide certain reference values for formulating PM 2.5-related preventive measures; Liu proposed a hybrid model of VMD based on rolling time windows and improved ISSA and LSTM for forecasting futures price time series [25]. The empirical results show that the VMD-ISSA-LSTM model performs best on high-frequency data, which helps improve the forecasting quality and provide effective support for financial risk control and investment decision-making; Pan [26] aims to improve the accuracy of the short-term power load forecasting model and combines signal decomposition, ensemble learning, intelligent optimization algorithm, and deep learning to build a combined forecasting model. Aiming at the problem of data quality, an improved VMD-SG filter is introduced to smooth and reduce noise. To solve the parameter adjustment problem of LSTM, the sparrow optimization algorithm is used to optimize the original model. The above literature shows that the combination of signal decomposition, optimization algorithm, and deep learning has good applicability and advantages in the prediction of complex dynamic systems.

In terms of mixing uniformity, Li *et al.* proposed to use information entropy to calculate the index weight to evaluate the mixing uniformity of tobacco [27]. Ju *et al.* used a BP neural network to establish a nonlinear relationship between mixing uniformity and weight to predict the uniformity of components [28]. Liu *et al.* proposed an intelligent identification method for concrete uniformity based on dynamic mixing, which solved the problem of insufficient detection methods in the concrete mixing process [29]. In summary, the application of machine learning in complex process control and uniformity evaluation has gradually matured, especially in dynamic multivariate data analysis and resource saving, which provides a reference for this study.

In the process of microwave mixing and preparation of cerium oxide products, the mixing state of materials and the concentration distribution of products have strong timeliness, so the machine learning algorithm of LSTM is suitable for predicting the above states; And for different periods, power conditions and liquid concentration conditions, its specific state presents different change amplitude and trend, which requires VMD decomposition to provide conditions for individual forecasting of each signal. At the same time, the optimization of LSTM forecasting by SSA can greatly improve the reliability of the results and improve the accuracy of the forecasting results.

To solve the problem of the mixing uniformity of cerium chloride solution, a machine learning optimization scheme based on the VMD-SSA-LSTM model is proposed, which provides data-driven through CFD fluid simulation to improve the prediction accuracy. Due to the strong timeliness of the mixing state and concentration distribution in the preparation of cerium oxide, the LSTM model can effectively capture the time series changes, the VMD decomposition further ensures the independent prediction of different signal components, and the SSA algorithm optimizes the prediction accuracy and stability of the LSTM. In this paper, a green and efficient intelligent analysis method is proposed by combining numerical simulation and intelligent prediction algorithms to achieve high-precision prediction of the mixing uniformity of cerium chloride solution under different process conditions.

MATERIALS AND METHODS

Model and mesh

In the HFSS module of Workbench 22R1, the 3D modeling is carried out at a 1:1 scale according to the size of the microwave pyrolysis experimental equipment, and the microwave oven adopts the national standard BJ26 waveguide model. Adaptive meshing is used to solve the solution, and the mesh is refined by the Mesh module. The microwave oven has a three-dimensional tetrahedral grid, and the hot zone and outlet extension have a hexahedral grid. The grid size is 2.5 mm, and the total number of grids is 1.4 million. In the Fluent solver module, the microwave oven model is shielded and only the Venturi reactor is mesh refined to improve simulation efficiency and ensure accurate modeling of critical sections. The straight pipe part is in the microwave oven, and the mesh adopts a structured meshing method, which is composed of the following steps: 1. a mesh generation method 2, a mesh area division 3, mesh refinement and adaptive processing 4, mesh quality and evaluation; Fig. 1a is the overall structure of the venturi pyrolysis reactor, including the inlet and outlet and the waveguide position, Fig. 1b is the structure and meshing of the individual venturi reactor, Fig. 1c is the meshing of the straight pipe of the venturi reactor, the diameter of the pipe is 30 mm, the length is 310 mm, the coordinates of the left center of the circle are (X=0, Y=0.135 m, Z=0.13 m), and the central axis of the round pipe is (X=0-0.31 m, Y=0.135 m, Z=0.130 m). The total number of grids is 700,000, and the minimum orthogonality of the grids is 0.74.

Calculation method (VMD-SSA-LSTM method)

Calculation method

Fluent software provides four multiphase flow models: VOF, Mixture, Eulerian-Eulerian, and Wet Steam. Because this paper involves droplet diffusion, the VOF model is adopted. Phase Couple SIMPLE algorithm based on pressure-velocity basis and first-order explicit transient algorithm are used in the unsteady calculation. The time step is one thousandth of a second and the iteration times of each time step is 20. This simulation puts forward the following assumptions: (1) Fluid is incompressible; (2) The single solenoid is 32 W, and the second is 64 W; (3) The initial temperature of each area in the flume is 300 K; (4) Permeability is constant at 1.

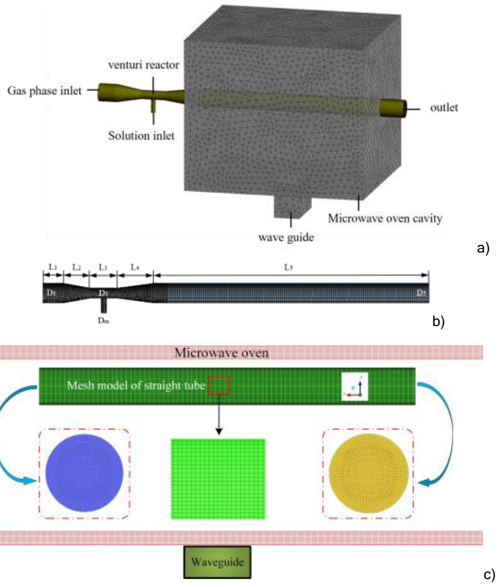

Figure 1. Geometry and meshing. (a) Schematic diagram of pyrolysis plant structure; (b) Schematic diagram of the size and structure of the Venturi reactor; (c) Straight pipe structure and grid.

Thermodynamic parameters as well as dielectric properties:

Table 1. Thermodynamic parameters as well as dielectric properties.

Sample Material	Cp, J/(kg K)	λ, W(m K)	μ, N s/m^2	ε_0	ε''
$CeCl_3$	109.83	600	1.72e^{-5}	72	0.73

λ thermal conductivity; Cp specific heat capacity; μ viscosity、ε_0 dielectric constant; ε'' loss factor.

The boundary conditions and parameter settings for HFSS are shown in Table 2. For solving flow field and heat transfer problems, it is necessary to define boundary conditions.

Table 2. HFSS boundary conditions.

Boundary surface	Boundary condition	Scope
Cavity of microwave oven	Perfect conductor boundary	–
Incentive condition	Excitation of wave port	2.4-2.5 GHz
Scanning step	–	0.01 GHz

In this numerical simulation study, all the boundary conditions are solid wall boundaries in static electromagnetic mixing and microwave thermal mixing. Under this condition, the material and product will not be lost. The specific boundary conditions are shown in Table 3.

Table 3. Static boundary conditions.

Boundary surface	Boundary condition
Cavity of microwave oven	Ideal conductor
Waveguide	Wave port
Wall surface of the reactor	Solid wall

VMD-SSA-LSTM model coupling process

Start by entering the data; Then, the VMD method is used to decompose the original data to obtain k components. SSA was used to optimize the initial parameters of the LSTM, the search range of the sparrow population size N, the maximum number of iterations M, and the parameter range (number of neurons in the hidden layer H, training times E, and learning rate η) were set, and then the mean square error (MSE) was selected as the objective function in the optimization algorithm, and finally the coupling model of the sparrow search algorithm and the long-term and short-term neural network (SSA-LSTM) was established. The SSA-LSTM prediction model was input into each component separately to obtain k prediction models. Finally, the prediction values of k prediction models are added together.

Test verification

To ensure the reliability of the numerical simulation results in this paper, the verification test as shown in Figure 2a is carried out. Start the spotlight (JINBEI) to make the experimental observation position bright enough; Adjust the parameters, placement position, and height of the high-speed camera of Thousand-eyed Wolf, so that the image can be displayed on the computer screen responsible for recording; Two electromagnets with a power of 32 W are placed on both sides of the sink to generate electromagnetic fields; The size of the flume is 9.5 cm × 12 cm. Before the experiment began, distilled water was pre-added to the sink to a height close to 1.5 cm, and the droplets were dripped by the rubber head dropper, which was inserted into the hole at one end of the metal frame and kept fixed.

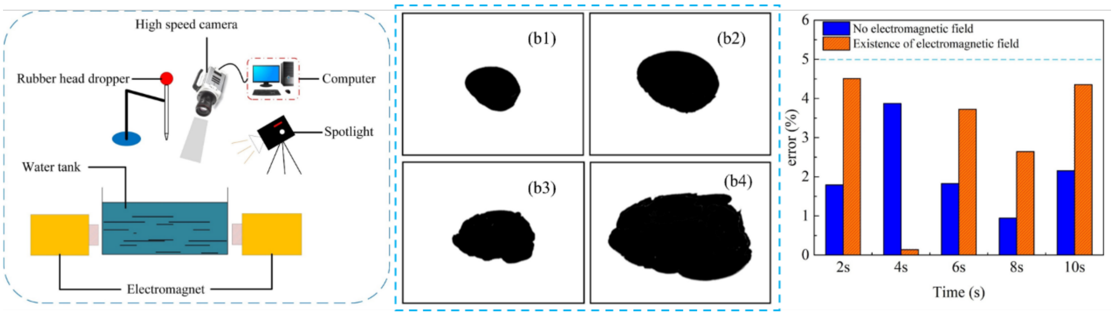

(a) (b) (c)

Figure 2. Verification experiment : (a) Schematic diagram of the validation experiment; (b) Comparison of droplet diffusion areas; (c) Error comparison chart.

After all the preparatory work before the test is completed, adjust the rubber head dropper to 1.5 cm height, electrify the electromagnet, drop cerium chloride solution droplets with a particle size of 3.75 mm from the rubber head dropper, and immediately diffuse into the water to form a diffusion area. To make the diffusion area more obvious, a little black ink was added as a tracer to observe the diffusion of droplets, and the whole process was recorded by a high-speed camera.

The diffusion image of cerium chloride solution taken by the high-speed camera is grayscale processed and binarized, so that the approximate change of diffusion area in the test can be observed more intuitively, and the processed binarization image is shown in Fig. 2b, b 1 and b 2 are the diffusion of cerium chloride solution in the ordinary state, and b 3 and b 4 are the diffusion under the action of the electromagnetic field. Through comparison, it was found that the diffusion rate of the cerium chloride solution underwent significant changes. In the absence of an electromagnetic field, the diffusion of the cerium chloride solution to the surrounding areas was relatively smooth and regular. However, under the influence of the electromagnetic field, the diffusion of the cerium chloride solution appeared less regular and smooth. The diffusion area under the influence of the electromagnetic field was larger than that without the electromagnetic field, leading to changes in the dynamics and morphology of the diffusion process. Then, the numerical simulation process is carried out. According to the size of the flume, the grid model is established, and the appropriate initialization state and boundary conditions are set. The change of cerium chloride diffusion area within 10 seconds is recorded, and compared with the diffusion area at the same time in the test process, and the error between them is calculated.

The variation of diffusion area of cerium chloride solution with time within 10 s was sorted out. Using Visual Studio software to write a C language program to calculate the black area in image processing technology, import it into Opencv library, and finally present the black area in the drawing, thus obtaining accurate contrast results.

The comparison between numerical simulation results and experimental results is shown in Figure 2c. Through the comparison of numerical simulation and experimental values, it can be seen that the overall error under the action of the electromagnetic field is higher than that under the action of no electromagnetic field and the error has been kept below 5%, which ensures the accuracy of the selected dynamic model, boundary condition setting and numerical simulation model.

Governing equations

When cerium chloride solution is in the electromagnetic field, its motion is affected not only by ordinary hydrodynamic equations but also by Maxwell equations reflecting electromagnetic law. In this case, if a microwave or electromagnetic field interacts with cerium chloride solution, a series of complex physical phenomena and reactions will be caused.

Maxwell's equation is shown in equations 1–4:

$$\nabla \cdot D = q_e \tag{1}$$

$$\nabla \cdot B = 0 \tag{2}$$

$$\nabla \cdot E = \frac{\partial B}{\partial t} \tag{3}$$

$$\nabla \cdot H = \frac{\partial D}{\partial t} + J \tag{4}$$

where B refers to magnetic flux density (Wb/m^3), D refers to electric displacement or flux density (C/m^2), E refers to electric field strength (V/m), H refers to magnetic field strength (A/m), J refers to current density vector (A/m^2), and q_e refers to charge density (C/m^3).

The constitutive equations for the electromagnetic field are determined by Eqs. (5) and (6), and the magnetic Reynolds number is low during electromagnetic mixing and heating, so magnetic diffusion is ignored.

$$B = \mu H \tag{5}$$

$$J = \sigma\left(E + \mu \times B\right) \approx \alpha E \tag{6}$$

where μ is the permeability and σ is the electrical conductivity.

During the electromagnetic mixing of cerium chloride solution, under the influence of microwaves, the charged particles will be subjected to electromagnetic forces, i.e., Lorentz force and electric field force, from which the formulas are derived:

$$F_l = J \times B = \alpha E \times \mu H = \alpha \mu E \times H \tag{7}$$

$$F_e = qE \tag{8}$$

where q is the amount of charge (C).

In the process of microwave heating, the microwave energy is absorbed by the droplets and converted into heat, which can be expressed by the following formula:

$$Q = \frac{1}{2}\omega \varepsilon_0 \varepsilon'' \left|E\right|^2 \tag{9}$$

where, ω refers to the angular frequency (rad/s), ε_0 refers to the free space permittivity (8.85×10^{-12} F/m), ε'' refers to the corresponding loss factor, $/E/^2$ refers to the modulus of the electric field, and Q is the energy absorbed or converted (J).

Choose from standard k-ε models and Euler-Euler multiphase flow models to simulate fluid mixing and flow in the lumen. The Lorentz force [30] and the electric field force are added to the momentum equation as source terms. The theoretical equation is as follows:

Momentum equation:

$$\frac{\partial\left(\rho u_i\right)}{\partial t} + \nabla \cdot \left(\rho u_i u_j\right) = -\nabla P + \mu_{eff} \nabla^2 u_i + \rho g + F_l + F_e \tag{10}$$

where P is the pressure (Pa); μ_{eff} is the effective viscosity (Pa s); g is the acceleration due to gravity (m/s^2); Fl is the Lorentz force (N), Fe is the electric field force (N).

Energy equation:

$$\frac{\partial\left(\rho T\right)}{\partial t} + div\left(\rho u T\right) = div\left(\frac{k}{C_p} gradT\right) + S_T \tag{11}$$

where C_P is the specific heat capacity; T is the temperature; k is the heat transfer coefficient of the fluid; S_T is the internal heat source of the fluid and the part of the fluid that converts mechanical energy into heat energy due to viscosity, sometimes referred to as the viscous dissipative phase.

When predicting the mixing uniformity under different process conditions, the VMD signal of the data set should be decomposed first, and the decomposition steps are as follows: Eqs. (12–14) are understood after the split of Eq. (15).

(1) It is assumed that the input signal $f(t)$ consists of k modal components and k is the center frequency of each eigenmode function $u_k(t)$. Firstly, the Hilbert transform is performed, and the decomposed signal of the modal function is obtained according to the single-side spectrum, as shown in Eq. (12).

Then, the center frequency $exp(j\ w_k\ t)$ of each decomposed signal is estimated, and the frequency spectrum of the decomposed signal is converted to the baseband by shifting the frequency, as shown in Eq. (13).

$$E\left(\delta(t)+\frac{j}{\pi t}\right)*u_k(t) \tag{12}$$

where, $u_k(t)$ is the eigenmode function with finite bandwidth with stricter constraints is redefined. Defined as:

$$u_k(t)=A_k(t)\cos(\phi_k(t))$$

where $\delta(t)$-pulse function.

$$\left[\left(\delta(t)+\frac{j}{\pi t}\right)*u_k(t)\right]\bullet\exp(-j\omega_k t) \tag{13}$$

(2) The square norm of the decomposed signal gradient is calculated to obtain the signal width, as shown in Eq. (14). The limiting principle is that the sum of each modal function is equal to the input signal *f* so that the sum of the estimated widths of each modal function is minimized. The final constrained variational problem is as follows:

$$\left\|\partial_t\left[\left(\delta(t)+\frac{j}{\pi t}\right)-u_k(t)\right]\cdot\exp(-j\omega_k t)\right\|^2 \tag{14}$$

VMD decomposes the input signal $x(t)$ into k, each corresponding to a specific frequency band. The basic goal is to decompose the input signal into multiple band-restricted signals $u_k(t)$ so that each modality is smoothed across its frequency band. The optimization problem of VMD can be expressed as:

$$\min_{\{u_k\},\{\omega_k\}}\left\{\sum k\left\|\partial_t\left[\left(\delta(t)+\frac{j}{\pi t}\right)*u_k(t)\right]\bullet\exp(-j\omega_k t)\right\|^2\right\} \tag{15}$$
$$s.t.\sum ku_k=f$$

where: $\{u_k\}=\{u_l,\cdots,u_k\}$; $\{\omega_k\}=\{\omega_1,\cdots,\omega_k\}$.

(3) To transform the constrained variational problem into an unconstrained variational problem, an augmented Lagrangian function is proposed to obtain the optimal solution of the constrained variational problem, as shown in Eq. (16).

$$L(\{u_k\},\{\omega_k\},\lambda)=\alpha\left\|\Sigma_k\partial_t\left[\left(\delta(t)+\frac{j}{\pi t}\right)*u_k(t)\right]\cdot\exp(-j\omega_k t)\right\|_2^2 \tag{16}$$
$$+\left\|f(t)-\Sigma_k u_k(t)\right\|_2^2+\left\langle\lambda(t),f(t)-\Sigma_k u_k(t)\right\rangle$$

where: α is the quadratic penalty factor; $\lambda(t)$ is a Lagrangian multiplication operator.

(4)The saddle point of Eq. (16) is obtained by the alternating direction multiplier method, and the optimal solution of Eq. (15) is obtained by iterating u_k^{n+1}, w_k^{n+1} and λ_k^{n+1}, where u_k^{n+1} is obtained by Eq. (17).

$$u_k^{n+1}=\operatorname{argmin}\left\{\begin{array}{l}\alpha\Sigma_k\left\|\partial_t\left[\left(\delta(t)+\frac{j}{\pi t}\right)*u_k(t)\right]\cdot\exp(-j\omega_k t)\right\|_2^2+\\ \left\|f(t)-\Sigma_k u_k(t)+\frac{\lambda(t)}{2}\right\|_2^2\end{array}\right\} \tag{17}$$

(5) To transform Eq. (17) above the frequency domain, Fourier isometric transform can be used to obtain quadratic optimization. The result of solving the problem is shown in Eq. (18). Similarly, the center frequency iteration problem can be transformed above the frequency domain to obtain the minimum value of w_k^{n+1}, as shown in Eq. (19), and w_k^{n+1} is obtained by Eq. (20).

$$\overline{u_k}^{n+1}(\omega)=\frac{\bar{f}(\omega)-\sum_{i\neq k}\bar{u}_i(\omega)+\frac{\bar{\lambda}(\omega)}{2}}{1+2\alpha(\omega-\omega_k)^2} \tag{18}$$

$$\omega_k^{n+1}=\operatorname{argmin}\left\{\int_0^\infty(\omega-\omega_k)^2\left|\bar{u}_k(\omega)\right|^2 d\omega\right\} \tag{19}$$

$$\omega_k^{n+1}=\frac{\int_0^\infty\omega\left|\bar{u}_k(\omega)\right|^2 d\omega}{\int_0^\infty\left|\bar{u}_k(\omega)\right|^2 d\omega} \tag{20}$$

where: $\bar{u}_k(\omega)$ is the Wiener filter of $\bar{f}(\omega)-\sum_{i\neq k}\bar{u}_i(\omega)$; w_k^{n+1} is the center of the power spectrum of the current modal function.

The mixing degree is an important indicator to represent the mixing capability of electromagnetic mixing and conventional heating mixing for cerium chloride solution. Therefore, the mixing uniformity formula is introduced to quantify the mixing degree of the cerium chloride solution. When *M* approaches 100%, it indicates a higher mixing degree.

$$M=\left[1-\left[\sum_{i=1}^{n}\frac{(Xi-\overline{X})^2}{(n-1)}\right]^{\frac{1}{2}}/\overline{X}\right]\times 100\% \tag{21}$$

When the mixing uniformity reaches approximately 95%, it is considered a state of micro mixing, and when it reaches 98%, it is regarded as uniformly mixed.

RESULTS AND DISCUSSION

Mixing status of cerium chloride solution under microwave irradiation

Microwave mixing [31] of cerium chloride solution at time t=0 is carried out. Under the conditions of microwave power of 3–5 kW and liquid phase concentration of 0.02–0.1, the concentration distribution of cerium chloride solution within 2.4 s is shown in Figure 3.

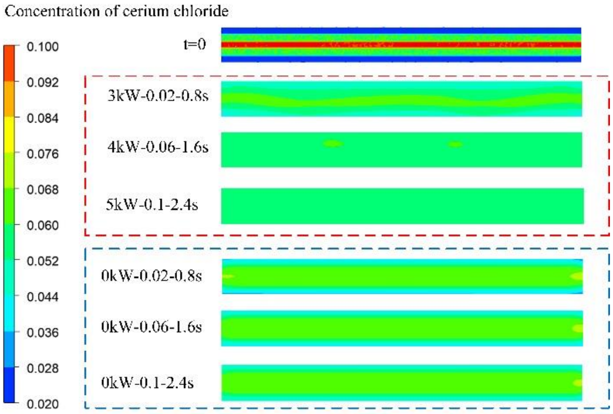

Figure 3. Concentration distribution of cerium chloride under different process conditions.

As shown in Fig. 3, under the reference of a free state, the microwave shows its influence on the concentration distribution of cerium chloride solution. When the concentration of cerium chloride solution is 0.02 and the time is 0.8 s, the microwave power of 3 kW makes the cerium chloride solution achieve the mixing effect; When the concentration is 0.06 and the time is 1.6 s, the microwave power is increased to 4 kW, and the cerium chloride solution achieves better mixing effect; When the concentration is 0.1 and the time is 2.4 s, the concentration distribution of cerium chloride in the model tends to be consistent and stable under the influence of microwave power of 5 kW, and the cerium chloride solution achieves the best mixing effect.

Data preprocessing and parameter setting

Data preprocessing

The mixing uniformity data were obtained under the conditions of microwave power 3 kW, 3.5 kW, 4 kW, 4.5 kW, 5 kW, liquid concentration 0.02(100%), 0.04(100%), 0.06(100%), 0.08(100%), 0.1(100%), time 1/5 t, 2/5 t, 3/5 t, 4/5 t, t and so on.

Firstly, the Eq. (21) was programmed using the UDF (User-Defined Function) feature in Fluent. This allowed the mixing uniformity values at each time step to be output at the end of the respective time step during the calculation process. The values were written to a .txt file, thereby obtaining the variation of mixing uniformity over time. The mixing uniformity data is divided into a training set and a test set, and the ratio of 7:3 is used as the training set, in which the first 70% of data are used as the training set to train the model; The last 30% of the data is used as a test set, and the validity of the model is verified by predicting the data. The data set distribution is shown in Figure 4.

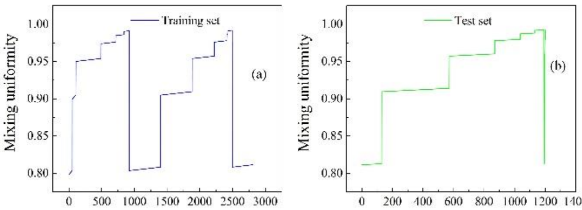

Figure 4. Data distribution diagram of training set and test set: (a)Training set; (b)Test set.

Parameter setting

The parameters of the VMD-SSA-LSTM model include the input layer and output layer. Adam optimization algorithm is adopted, and the initial learning rate is 0.01, and the learning rate is reduced to one-tenth of the original one every 10 iterations. The number of hidden layer units, maximum training period, and learning rate are super-parameters of the LSTM model, and the ranges are [50,300], [50,300], and [0.01,0.1], respectively. The population size of the sparrow is 30, the maximum iteration times are 10, and the decomposition mode numbers are 3, 4, and 5. Producers account for 20%, the safety threshold is 0.8, and RMSE is used as the fitness function.

VMD decomposition

In this section, the observation method is selected, and the optimal solution is selected according to the data situation, that is, the decomposition situation when the observed modal number k is 3, 4, and 5. VMD decomposition is performed. The maximum decomposition mode number is 5, the moderate bandwidth constraint/ penalty factor is 2500, there is no DC part, and the uniform initialization value of omegas is 1. The decomposition result is shown in Fig. 5, and the first behavior is the original data, where X represents the index of the data point. It can be seen that the VMD decomposition method is used to decompose the signals of different frequencies and ranges of the data set, which is beneficial to carry out separate operations on each signal mode and obtain more accurate forecasting results.

Forecasting research and result analysis

In the process of wave pyrolysis, there are complex electromagnetic effects on materials, which affect the uniform distribution of materials and materials

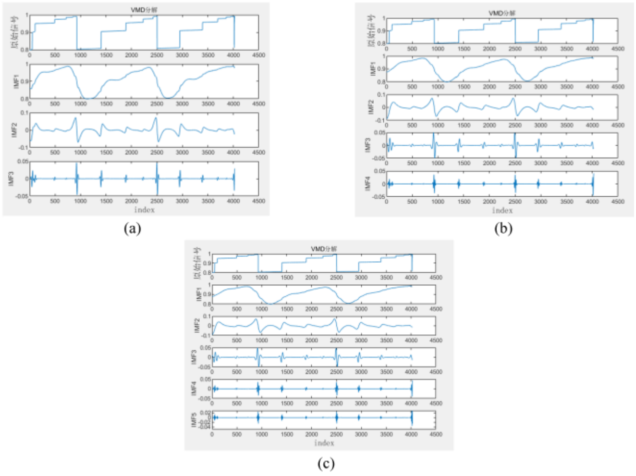

Figure 5. Modal signal distribution of VMD decomposition: (a) k=3; (b) k=4; (c) k=5.

and will have an important impact on the pyrolysis results. Therefore, to get more accurate forecasting results, this paper uses the VMD-SSA-LSTM model to optimize the parameters in the forecasting process to ensure the forecasting accuracy and reliability of the model.

LSTM is optimized by a sparrow optimization algorithm to predict each modal signal. Taking the data of the data set as an example, Fig. 6 shows the RMSE curve change of the sparrow search algorithm.

As can be seen from Fig. 6(a–c), when k=3, 4, and 5, RMSE values tend to be stable from the 5th, 6th, and 7th iterations respectively, and their corresponding fitness values are 0.0118, 0.0136, and 0.012 respectively. It can be seen from the figure that the sparrow search algorithm for optimizing the LSTM forecasting model is easy to converge.

Fig. 6(d–f) shows the comparison chart of the forecasting results of the three models. It can be seen from the chart that during the iteration process, the forecasting value of the VMD-SSA-LSTM algorithm is always closest to the real data, and when the real data value fluctuates greatly in the later iteration period, it can alleviate the fluctuation of the value to the greatest extent and maintain the stability of the forecasting data;

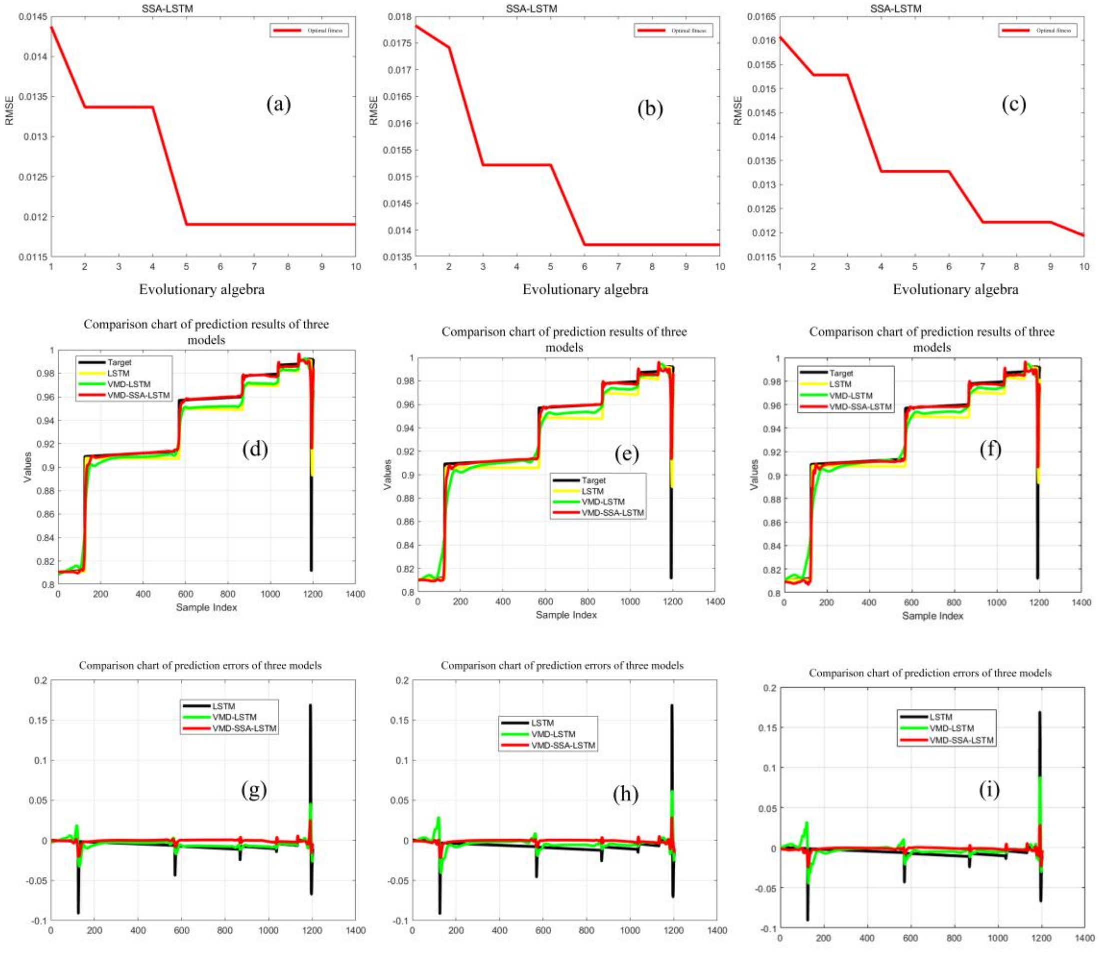

Figure 6. RMSE curve change and prediction results of sparrow search algorithm: (a) k=3; (b) k=4; (c) k=5; (d) k=3; (e) k=4; (f) k=5; (g) k=3; (h) k=4; (i) k=5.

As for the forecasting result, the forecasting result of the VMD-LSTM algorithm is closer to the real value than that of the single LSTM algorithm, which shows the necessity and effectiveness of the VMD signal decomposition.

Fig. 6(g–i) shows the comparison diagram of forecasting errors of the three models. It can be seen from the diagram that the forecasting error of the VMD-SSA-LSTM algorithm is always lower than that of the other two forecasting models during the iteration process, and when the real data value fluctuates greatly in the later iteration period, the error can fluctuate in a small amplitude near 0 to the greatest extent.

Tables 4 summarize the comparison of forecasting errors between the two models when the modal numbers are 3, 4, and 5. It can be seen from the table that RMSE, MAE, and MAPE predicted by the VMD-SSA-LSTM algorithm model are lower than those predicted by a single LSTM, showing better accuracy.

Table 4. Error comparison of two algorithms.

Forecasting algorithm		RMSE	MAE	MAPE (%)
k=3	LSTM forecasting	0.010429	0.0062302	0.67588
	VMD-SSA-LSTM forecasting	0.0026056	0.0011468	0.12304
k=4	LSTM forecasting	0.011174	0.0072928	0.78999
	VMD-SSA-LSTM forecasting	0.0028125	0.0013123	0.14047
k=5	LSTM forecasting	0.011272	0.0074544	0.80791
	VMD-SSA-LSTM forecasting	0.0031478	0.0013971	0.14702

It can be seen from Table 4 that when *k*=3, RMSE decreases by 0.7% and MAE decreases by 0.5%; MAPE decreases by 0.55%; When *k*=4, RMSE and MAE decrease by 0.8% and 0.6% respectively; MAPE decreases by 0.65%; When *k*=5, RMSE and MAE decrease by 0.7% and 0.6% respectively; MAPE decreases by 0.65%.

CONCLUSION

The experimental results show that microwave can promote the diffusion and mixing of cerium chloride solution, and verify the correctness of the calculation method, kinetic model, and calculation results selected by numerical simulation. The concentration distribution of cerium chloride solution changed under different microwave technology conditions, and achieved a good mixing effect, showing its non-thermal effect. Under different modal components (*k*), the errors of the VMD-SSA-LSTM forecasting model are significantly reduced compared with that of single long-short-time memory (LSTM) forecasting. When the VMD component is set to 3, the RMSE of the VMD-SSA-LSTM model is the lowest, and the selected decomposition mode number *k*=3.

REFERENCES

[1] C.Y. Chen, J.M. Lu, Q.Z. Yao, Chem. Eng. Sci. 22 (2016) 2501–2512. https://doi.org/10.12659/MSM.899852.

[2] Y. Xu, S.H. Yang, G.X. You, Asian J. Ecotoxicol. 16 (2021) 43–55. https://kns.cnki.net/kcms2/article/abstract.

[3] A. Patlán, V. Ayala-García, L. Valenzuela-García, PLoS. One. 14 (2019) e0211653. https://doi.org/10.1371/journal.pone.0211653.

[4] P. Min, S.Z. Zhang, Y.H. Xu, R.X. Li, Appl. Surf. Sci. 448 (2018) 435–443. https://doi.org/10.1016/j.apsusc.2018.04.103.

[5] G. Yoganandan, V. Durgambika, P. Manoj, M.N. Thayee, B.J. Nagabushan, R. Michael, N. Lakshman, Electrochim. Acta. 425 (2022) 140696. https://doi.org/10.1016/j.electacta.2022.140696.

[6] B. Richa, N. Sreeja, K. Krishna, Mater. Today Commun. 30 (2022) 103177. https://doi.org/10.1016/j.mtcomm.2022.103177.

[7] D.T. Diksha, M. Ananthkumar, Mater. Today: Proc. 49 (2022) 2007–2012. https://doi.org/10.1016/j.matpr.2021.08.1572.

[8] N. Li, Z.D. Chen, J.J. Wang, J. Mater. Rev. 36 (2022) 54–63. https://kns.cnki.net/kcms2/article/abstract.

[9] C.Y. Wang, P. Tong, C. Li, Carcinog., Teratog. Mutagen. 31 (2019) 464–468. https://kns.cnki.net/kcms2/article/abstract.

[10] L. Zhang, L.M. Zhu, T. Zhou, P. Guo, X. Wang, P. Liu, W. Shao, Mater. Des. 215 (2022) 110451. https://doi.org/10.1016/j.matdes.2022.110451.

[11] T. Bhusankar, Y. Kisoo, K. Jonghoon, Ceram. Int. 48 (2022) 3628–3635. https://doi.org/10.1016/j.ceramint.2021.10.143.

[12] H. Yang, L. Jia, Z. Zhang, B. Xu, Z. Liu, Q. Zhang, Y. Cao, M. Zhang, T. Ohno, J. Catal. 405 (2022) 74–83. https://doi.org/10.1016/j.jcat.2021.11.017.

[13] S. Galema, Chem. Soc. Rev. 26 (1997) 233–238. https://doi.org/10.1039/CS9972600233.

[14] C.O. Kappe, Chem. Bio. Chem. 43 (2004) 6250–6284. https://doi.org/10.1002/anie.200400655 .

[15] B.A. Roberts, C.R. Strauss, Acc. Chem. Res. 38 (2005) 653–661. https://doi.org/10.1021/ar040278m.

[16] F. Wiesbrock, R. Hoogenboom, U.S. Schubert, Macromol. Rapid Commun, 25 (2004) 1739–1764. https://doi.org/10.1002/marc.200400313.

[17] J.A Gerbec, D. Magana, A. Washington, G.F Strouse, J. Am. Chem. Soc. 127 (2005) 15791–15800. https://doi.org/10.1021/ja052463g.

[18] C. Lv, X. Lv, Q.Y. Zhao, Rare Metal. 46 (2022) 394–401. https://doi.org/10.13373/j.cnki.cjrm.xy19070035.

[19] C. Lv, T.A. Zhang, Z.H. Dou, Q.Y. Zhao, Rare Metals. 38 (2019) 1160–1168.

https://doi.org/10.1007/s12598-019-01337-9.

[20] C. Lv, H.X. Yin, Y.L. Liu, X.X, Chen, H.L. Zhao, JOM. 75 (2023) 2421–2429. https://doi.org/10.1007/S11837-022-05654-W.

[21] C. Lv, T.A. Zhang, Z.H. Dou, Q.Y. Zhao, JOM. 71 (2019) 34–39. https://doi.org/10.1007/s11837-018-3194-4.

[22] C. Luan, Water Resources & Hydropower of Northeast China. 42 (2024) 23–29. https://kns.cnki.net/kcms2/article/abstract.

[23] Z.P. Lu, X.J Yu, C.Y. Lu, Journal of Wuhan University of Technology (Information & Management Engineering). 45 (2023) 546–551. https://kns.cnki.net/kcms2/article/abstract.

[24] H.J. Cao, Z.Y. Li, Modern Information Technology.8 (2024) 142–146152. https://doi.org/10.19850/j.cnki.2096-4706.2024.04.030.

[25] Y.J. Liu, Shandong University, 2024. https://kns.cnki.net/kcms2/article/abstract.

[26] S.Y. Pan, China University of Mining and Technology. 2023. https://kns.cnki.net/kcms2/article/abstract.

[27] J.L. Li, G.Y. Yin, G.H. Zhang, Proceedings of the 31st chinese control, 2012, 7552–7555. https://ieeexplore.ieee.org/abstract/document/6391279.

[28] Y.P. Ju, Y.G. Li, Chinese Automatomation Congress (CAC). 2017, 777–781. https://doi.org/10.1109/CAC.2017.8242871.

[29] M.T. Liu, B. Li, S. Yue, Y. Du, J. Xu, Signal image and video Pro. 18 (2024) 427–436. https://link.springer.com/article/10.1007/s11760-023-02738-1.

[30] Y.J. Zhang, W.N. Qin, X.F. Huang, HU BEI: CN104809297A, 2015-07-29._ https://kns.cnki.net/kcms2/article/abstract.

[31] C. Lv, Y. Liu, G. Li, T. Yang, H. Zhao, X. Chen, Case Stud. Therm. Eng. 60 (2024) 104741. https://doi.org/10.1016/j.csite.2024.104741.

CHAO LV[1,2]
YANLONG LIU[2]
ZHANG LU LU[2]

[1]State Key Laboratory of Complex Nonferrous Metal Resources Clean Utilization, Kunming University of Science and Technology, Kunming, Yunnan, China

[2]Key Laboratory of Vibration and Control of Aero-Propulsion System Ministry of Education, Northeastern University at Qinhuangdao, Qinhuangdao, Hebei, China

NAUČNI RAD

IMOBILIZACIJA ALKALAZE NA HITOZAN/GLUTARALDEHID/TRIPOLIFOSFAT PERLE DOBIJENE TEHNIKOM INVERZNE EMULZIJE

Cerijum-oksid je važan strateški resurs i ključna sirovina za mnoge funkcionalne materijale u oblastima visoke tehnologije. Mmikrotalasno zagrevanje je važno za pripremu cerijum-oksida. U ovom radu su istražene varijacije faktora polariteta unutar rastvora tokom zagrevanja. Pored termičkih efekata, mikrotalasno zagrevanje vrši i elektromagnetne uticaje koji promovišu mešanje rastvora. Rad uključuje fizičke eksperimente i numeričke simulacije prirode mešanja rastvora cerijum-hlorida pod mikrotalasnom ekspozicijom. Rezultati otkrivaju da pod uticajem mikrotalasnog elektromagnetnog polja, uniformnost mešanja rastvora ostaje konzistentna i stabilna u celom regionu. Za predviđanje uniformnosti mešanja u različitim uslovima procesa predložen je VMD-SSA-LSTM model. Rezultati pokazuju da je efekat mešanja rastvora cerijum-hlorida u mikrotalasnoj pećnici bolji od onog pri konvencionalnom zagrevanju. Izabrani prognostički model štedi vreme i energiju i može precizno predvideti gornju situaciju. Pored toga, efekat predviđanja je najbolji kada je modalni broj k VMD dekompozicije iznosi 3.

Ključne reči: cerijum-oksid, fizički eksperiment, numerička simulacija, VMD-SSA-LSTM, prognoza.

CI&CEQ
Chemical Industry & Chemical Engineering Quarterly

Available online at
Association of the Chemical Engineers of Serbia *AChE*
www.ache.org.rs/CICEQ

Chem. Ind. Chem. Eng. Q. 31 (4) 315−323 (2025) CI&CEQ

BEHROOZ SEDIGHI[1]
ABOLFAZL DAVODIROKNABADI[2]
MOHAMMAD SHAHVAZIYAN[1]
MOHAMMADALI SHIRGHOLAMI[1]

[1]Department of Textile Engineering, Yazd Branch, Islamic Azad University, Yazd, Iran

[2]Department of Design and Clothing, Yazd Branch, Islamic Azad University, Yazd, Iran

SCIENTIFIC PAPER

UDC 66.017:66

THE INFLUENCE OF VIBRATION VELOCITY ON THE NANOCOMPOSITE OF HALLOYSITE CLAY NANOTUBES

Article Highlights

- Influence of vibration velocity on composite properties
- Enhancing electrical conductivity of the composite
- Enhancing crease recovery of composite

Abstract

This research examined the properties of a nanoweb created using the electrospinning technique, incorporating Halloysite clay nanotubes. The main focus was to understand how different vibration speeds affected the characteristics of the nanoweb. By utilizing FESEM and elemental mapping, it was confirmed that the Halloysite clay nanotubes were present and provided valuable insights into the structure of the samples. The results regarding electrical conductivity were remarkable, showing that the treated specimens had higher crease recovery properties compared to the untreated ones(more than 24%), thanks to the presence of Halloysite clay nanotubes and the different vibration speeds applied. In addition, the samples showed improved UV blocking capabilities up to about 75%, as well as exceptional strength (~33%) and abrasion resistance (~93%). Overall, the nanocomposite webs exhibited promising qualities that could have applications in various industries.

Keywords: clay nanotubes; vibration speed; electrospinning; nanoweb.

Nanoweb/fiber electrospinning is a cutting-edge technology that has the potential to revolutionize various industries, including healthcare and electronics. By harnessing the power of an electric field, electrospinning produces polymer webs that have a wide range of applications. These applications span across tissue engineering, drug delivery systems, filtration, and sensors. One particularly exciting application is in regenerative medicine, where these nanofibers can serve as scaffolds to support tissue regeneration. This process mimics the natural extracellular matrix and aids in the healing and restoration of damaged organs and tissues. Moreover, the small size of these webs facilitates cell adhesion and growth, which holds great promise for advancements in the treatment of injuries and diseases. Additionally, this technique can be utilized to create nanocomposites using natural materials [1–9].

To create a nanocomposite, Ghiasi *et al.* conducted a study that involved extracting active components from wheat bran using this particular method. According to their findings, the resulting composite contained nanomaterials and exhibited advantageous characteristics in terms of protection against ultraviolet rays and bacteria [10]. In contrast, Zohoori *et al.* [11] conducted a study where they utilized palm-based materials and carbon mesoporous nanoparticles to create a nanocomposite through the electrospinning method. This investigation demonstrated the effectiveness of electrospinning in the production of nanocomposites and achieved positive outcomes in enhancing the properties of the nanocomposite. Asakereh and his team conducted additional research by utilizing the technique of electrospinning to create nanocomposites using

---

Correspondence: A. Davodiroknabadi, Department of Design and Clothing, Yazd Branch, Islamic Azad University, Yazd, Iran.
E-mail: davodi@iauyazd.ac.ir
Paper received: 12 July, 2024
Paper revised: 28 January, 2025
Paper accepted: 6 February, 2025

https://doi.org/10.2298/CICEQ240712003S

hazelnut green shells. Through their study, they successfully synthesized nanocomposites made of gelatin and hazelnut green shells, which exhibit unique properties [12]. Nanomembranes and nanocomposites offer a broad spectrum of applications that enhance various attributes, including water-attracting capabilities, permeability to substances, salt rejection capacity, resistance to fouling, and long-lasting durability [13]. In recent times, there has been a significant increase in the focus on natural composites. This is because these composites possess unique characteristics such as effective sound insulation, recyclability, easy accessibility, and environmental friendliness. These properties are achieved by incorporating nanomaterials into the composites. Currently, a wide range of nanomaterials is being utilized to enhance specific qualities in the final products. One example of such a nanomaterial is nano clay. Nano clay is known for its impressive strength-to-weight ratio, meaning that despite being lightweight, it exhibits remarkable strength and durability. Additionally, nano clay possesses exceptional barrier capabilities. Its extremely small size and unique structure enable it to form a tight network of particles, acting as a barrier against gases and liquids [14–21].

The study conducted by Gbadeyan *et al.* discovered that the addition of nano clay to banana fibers enhances the bonding between the matrix, nano clay, and banana fiber. This improvement is attributed to the thermal properties and hydrophobic nature of the nano clay, as well as the enhanced capacity of the banana fiber to distribute stress within the biocomposites. As a result, there is a significant enhancement in the dynamic mechanical analysis, rate of water absorption, and abrasion properties [22]. Nanofibers and nanowebs, despite their lack of electrical conductivity, possess certain limitations in terms of their properties. The occurrence of static electricity in nanowebs leads to their adherence to the surrounding environment, causing discomfort when worn. Additionally, static electricity poses a disadvantageous factor in knitting and weaving processes, possibly resulting in fabric damage. Numerous approaches exist for investigating the electrical conductivity of these materials [23–27].

This study presents a novel approach to the creation of a nanocomposite by incorporating Halloysite clay nanotubes and subjecting the material to varying vibration speeds during its synthesis. The findings are groundbreaking, particularly in the realm of electrical conductivity, where the treated specimens outperformed their untreated counterparts. The incorporation of Halloysite clay nanotubes, coupled with the effects of controlled vibration speeds, significantly enhanced crease recovery properties, making the material more versatile for practical applications. Additionally, the nanocomposite demonstrated improved UV-blocking capabilities and exceptional mechanical properties, including strength and resistance to abrasion. These advancements underscore the potential of this innovative methodology in developing high-performance materials for diverse industrial applications.

The primary objective of this study involved the creation of a nanocomposite by utilizing Halloysite clay nanotubes with the application of different vibration speeds. The aim was to assess the diverse attributes of the composite and establish a versatile nanostructure. Rather than depending on chemical particles, this research opted for the integration of nanoparticles and vibration energy as a doping agent to augment the characteristics of nanocomposites.

MATERIALS AND METHODS

Materials and devices

Halloysite clay nanotube ($Al_2Si_2O_5(OH)_4 \cdot 2H_2O$) with a surface area of 64 m^2/g and molecular weight of 294.19 was prepared from Sigma Aldrich (CAS No.1332-58-7). Tetra-ammine-di-aqua-copper(II) hydroxide with formula of $[Cu(NH_3)_4(H_2O)_2](OH)_2$ and succinic acid (CAS No.110-15-6) as a cross-link factor was prepared from Merck. The strength under tension was analyzed using a tabletop uniaxial testing device called INSTRON 3345. To achieve homogeneity in the solution, a high-energy micro-vibration homogenizer (model MSK-SFM-12M-LD) was utilized. The abrasion resistance was evaluated using the ASTM D-3884-09 method, employing a double-head rotary platform. We examined the morphology of the specimens by utilizing a field emission scanning electron microscope (FESEM-MIRA3-TESCAN). To enhance visibility, a thin layer of gold film was applied to the samples. A magnetic stirrer (Model: HPMA 700) was used to prepare the solution. To gauge the level of electrical conductivity, we utilized the Hioki digital multimeter model 3256/50 from Japan. Also, the crease recovery tester device model GT-C21-1(China) was used. The crystalline structure of the materials was characterized by the X-ray diffraction (XRD)model Bruker D8 Discover, Germany.

Method

Pure cellulose was liquefied utilizing Schweizer's reagent, also identified as ($[Cu(NH_3)_4(H_2O)_2](OH)_2$). This liquefaction phase lasted for half an hour, conducted with a magnetic stirrer at 60°C. In the next step, succinic acid was infused into the concoction, accompanied by Halloysite clay nanotubes of 1.5% concentration. This newly formed compound was then agitated for another half-hour at the same temperature of 60 °C, utilizing a magnetic stirrer. Following this, the concoction was subjected to a high-intensity micro-vibration homogenizer employing a device with vibration speeds of 2700, 3500, and 4000 rpm, at a temperature of 50 °C for 3 minutes. The final blend was then divided into three different syringes situated on an electrospinning machine. The result of this operation was the successful creation of a nonwoven web.

Table 1. Specification of samples.

Sample	Vibration speed (rpm)	Halloysite clay nanotube (%)
A	-	0.0
B	2700	1.5
C	3500	1.5
D	4000	1.5

RESULTS AND DISCUSSION

Morphological analysis

An in-depth exploration of the physical properties of nanofibers produced via electrospinning necessitates a meticulous study of their microscopic architecture. This examination enables us to understand the layout, dispersal, dimensions, form, and surface attributes of these nanofibers. By employing state-of-the-art visualizing methods such as field emission scanning electron microscopy (FESEM), we can procure intricate, high-definition images that display the complex aspects of these fibers. This inclusive review offers precious knowledge on how elements like polymer density, electric charge, and solvent mix impact the construct of electrospun nanofibers. Figure 1 portrays a field emission scanning electron microscopy visual of the specimen, indicating that the cross-section of the nanocomposite is about 59 nm. Moreover, Figure 1(A–B) demonstrates that the nanofibers are synthesized via electrospinning. Upon more detailed scrutiny, it's evident that the breadth of the nanofibers doesn't surpass 75 nm, which is exceptionally satisfactory. Upon scrutiny of the distribution of Halloysite clay nanotubes, it becomes evident that they approximately span 34 nm Figure 1C. Moreover, their configuration is distinctly portrayed through the visual depiction. The images we acquired suggest that the parameters set for electrospinning have been successful, considering there are no major signs of necking in the FESEM analysis conducted. On the other hand, a frozen section image is captured to confirm the internal presence of the nanotubes. For this purpose, a small portion of the web is collected and rapidly frozen using liquid nitrogen to maintain its structural integrity. Subsequently, a microtome designed for frozen samples is employed to slice the frozen sample into thin sections (Figure 1D). This image reveals that the Halloysite clay nanotubes are moderately evenly distributed within the fibrous network, with minor clustering observed in select regions. The nanotubes retain their tubular structure and remain intact, with no significant deformation visible. There is clear evidence of close interaction between the cellulose fibers and the nanotubes, suggesting good integration within the composite structure. The fibers exhibit consistent diameters and smooth surfaces, indicative of uniform electrospinning conditions.

XRD analysis

Figure 2 shows the XRD pattern of the sample. The XRD pattern shows that the electrospinning process successfully integrates kaolin clay nanotubes and cellulose into a composite material. Both components retain their distinct crystalline characteristics while forming a stable physical mixture. The chart indicates a high potential for the material's use in applications requiring a hybrid of strength, adsorption, and biodegradability. Here's a detailed analysis of the chart:

Kaolin clay peaks: A sharp peak at approximately 12° 2θ, indicative of kaolinite’s basal plane reflections. A moderate peak at around 20° 2θ, associated with higher-order reflections from kaolin. A distinct peak near 25° 2θ, commonly attributed to structural lattice planes of kaolinite. A broad peak at 35° 2θ, characteristic of less intense but significant kaolinite reflections. A sharp peak at 62° 2θ, a higher-angle reflection related to kaolinite's crystalline structure.

Cellulose peaks: A smaller but noticeable peak at 15° 2θ, corresponding to the amorphous phase of cellulose. A strong and sharp peak at 22° 2θ, the most prominent cellulose peak, associated with the crystalline plane (200) of cellulose I. A weaker but evident peak at 34° 2θ, related to less prominent crystalline planes in cellulose.

The XRD diagram reveals a composite structure where kaolin nanotubes and cellulose retain their distinct crystalline and amorphous characteristics, enabling synergistic interactions that enhance electrical conductivity. The sharp peaks of kaolin indicate its ordered nanotube structure, which acts as a scaffold for charge transfer, while the crystalline and amorphous regions of cellulose contribute mechanical flexibility and ionic mobility, respectively. The uniform dispersion of kaolin within the cellulose matrix, facilitated by the electrospinning process, minimizes resistance and creates interconnected pathways for electron and ion transport. This combination of

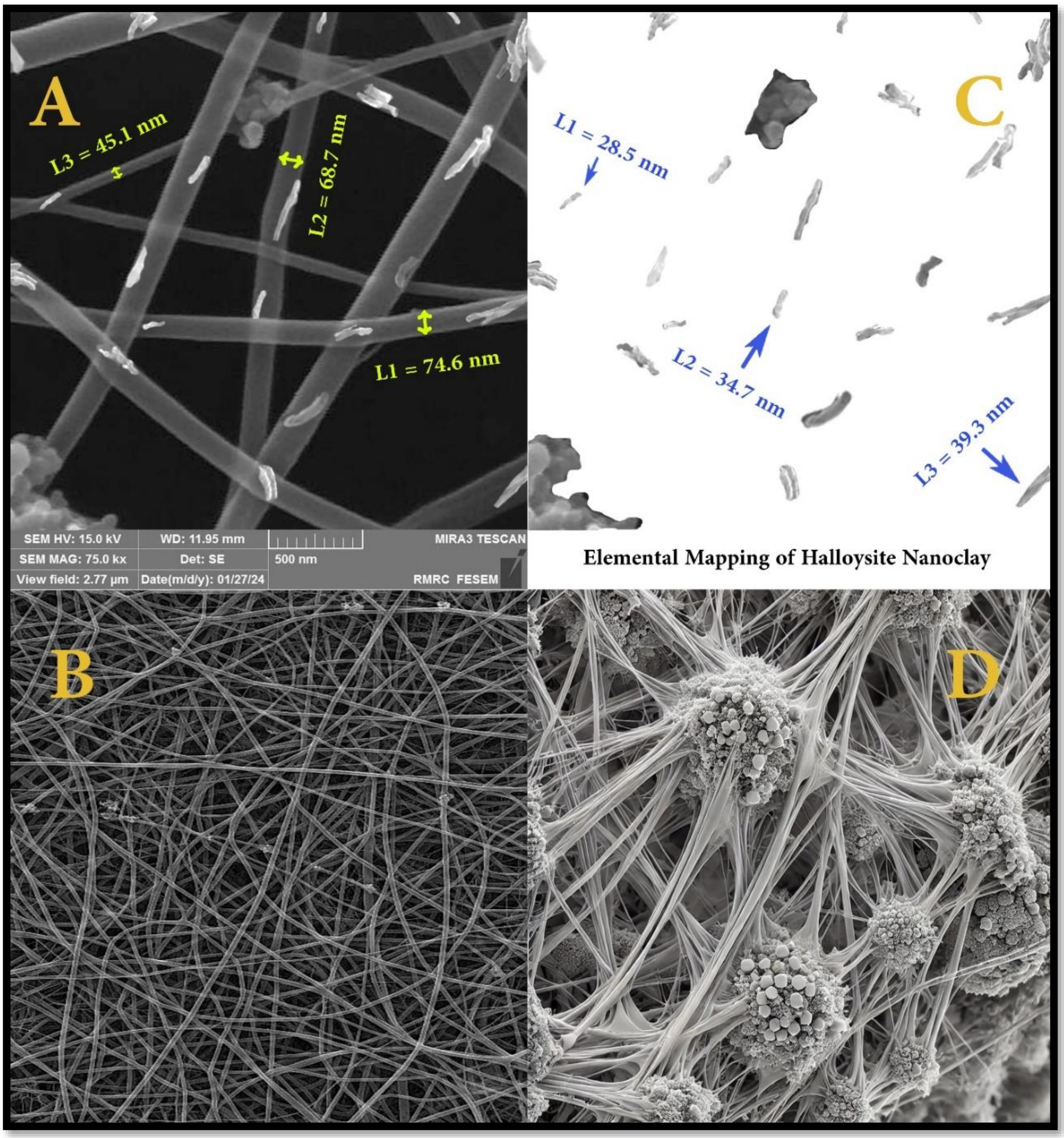

Figure 1. FESEM of: (A, B) Electrospun sample, (C) Elemental map, and (D) Frozen section.

structural order, physical interaction, and charge mobility results in a composite with improved electrical conductivity compared to its components.

The conductive network in the composite is formed despite the uneven distribution of clay nanotubes due to percolation theory, where sufficient connectivity among nanotubes enables electron or ion transport. The high aspect ratio of the nanotubes ensures overlapping conductive pathways, while the cellulose matrix supports ionic mobility in regions with fewer nanotubes. Localized zones of higher nanotube concentration compensate for less dense areas, allowing the composite to maintain conductivity.

The enhanced interface between the clay nanotubes and cellulose nanofibers arises from the electrospinning process, which embeds the nanotubes into the matrix and promotes strong interfacial adhesion through hydrogen bonding. The alignment of cellulose chains around the nanotubes during spinning and potential surface functionalization of the clay further improve compatibility and charge transfer. Together, these factors create a hybrid structure that balances conductivity with mechanical stability, even with non-uniform nanotube distribution.

The enhanced interface between Halloysite nano clay (HNTs) and the electrospun cellulose matrix is primarily attributed to specific chemical and physical interactions that improve adhesion, dispersion stability, and charge transfer. One of the dominant mechanisms is “hydrogen bonding”, where hydroxyl (-OH) groups on both Halloysite and cellulose form strong intermolecular bonds, ensuring a stable interface and uniform dispersion. Additionally, “van der Waals forces” contribute to stabilizing the nanotube dispersion within the matrix, preventing agglomeration. The electrospinning process further enhances interfacial interaction through “mechanical interlocking”, where the high shear forces align cellulose chains around the nanotubes, creating a physically integrated structure that improves stress transfer. If the nanotubes undergo “chemical functionalization”, such as Silane coupling or carboxylation, “covalent bonding” can be introduced, forming a more permanent attachment to the cellulose matrix, which further strengthens mechanical integrity and charge transfer. Moreover, “ionic interactions” may occur if functionalized nanotubes carry opposite charges to the cellulose, enhancing dispersion stability and conductivity. These interactions collectively improve the composite’s performance by reducing nanotube aggregation, increasing mechanical strength, and optimizing charge mobility.

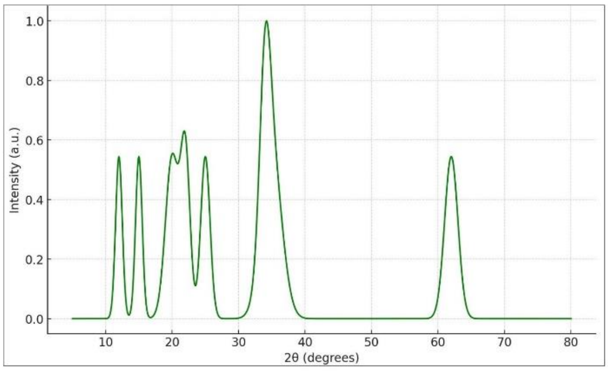

Figure 2. XRD pattern of sample.

Abrasion and strength properties

Throughout their existence, nanocomposites such as nano-webs experience a range of pressures and strains. Known for their minuscule size and remarkable resilience, nano-webs have instigated considerable transformations across various sectors. To assess the effects of wear and tear, a friction test involving 10 cycles was carried out to calculate the shift in the sample's mass pre and post-test. As depicted in Table 2, all processed samples show outstanding resistance against wear and tear. Even post 10 friction cycles, they uphold a resistance rate above 91%. When we contrast samples A, B, C, and D, there's a marked disparity in their resistance to wear. Sample A, employed as a control specimen, showed zero resistance, while the remaining samples exhibited maximum resistance. This difference can be credited to the increased interfacial interactions within the webs, enabled by Halloysite clay nanotubes. These interactions result in superior load distribution and resistance to deformation. The large surface area and distinct surface chemistry of Halloysite clay nanotubes foster robust bonding with the nearby polymer matrix, contributing to this occurrence.

Sample C's remarkable sturdiness can be attributed to the inclusion of Halloysite clay nanotubes and a 3500 rpm vibrational treatment. Elevating the rpm results in enhanced resilience and strength. Nevertheless, surpassing 3500 rpm results in a minor decline in these characteristics. This happens due to excessive power causing an increase in heat, which could adversely affect the polymer solution or solvent involved in the electrospinning process.

To evaluate the durability of the samples, tension tests were performed on the produced nanofibers. The results showed that the treated specimens displayed impressive lastingness. This is a significant observation since the robustness of these nano-webs exceeds that of the control sample. The exceptional toughness of these webs is due to their unique molecular structure and makeup. Comprised of extended chains of organic molecules closely packed, the webs form a compact and sturdy material. This particular configuration allows the nano-webs to withstand considerable stress and strain without showing signs of cracks or distortions. Additionally, the nanowebs display an exceptional ability to resist wear and tear, demonstrating their potential to endure degradation from friction.

Table 2. Abrasion resistance, tensile strength, and crease recovery angle of samples.

Sample	Web weight before abrasion (g)	Web weight after abrasion (g)	Abrasion resistance (%)	Tensile strength(MPa)	Crease recovery angle(deg)
A	3.186	1.707	53.57	0.865	144
B	3.466	3.158	91.11	1.903	167
C	3.599	3.374	93.74	2.751	179
D	3.605	3.369	93.45	2.699	177

Crease recovery property

Crease recovery properties refer to the resilience of a rectangular fiber piece when it's subjected to a certain load and folded for a specific timeframe. This property measures the fiber's ability to bounce back to its original state without wrinkles. This is gauged by the angle created between the halves before it was folded, commonly known as the crease recovery angle. During this experiment, samples measuring 40*15mm were trimmed and evaluated to determine crease recovery.

The ultimate recorded value of the crease recovery angle represents an average of five separate measurements.

Table 2 shows the influence of different finishing conditions on the crease recovery characteristic of the nanoweb at various vibration speeds. Clearly, the processed samples showed a substantial rise of more than 13% in the angle of crease recovery. In particular, sample C revealed the greatest enhancement, with an increase of around 19%, while sample D showcased a significant rise of nearly 18%. A key factor for this improved crease recovery in nanofibers that contain clay nanotubes is their unique formation. Clay nanotubes are known for their high aspect ratio and hollow tubular design, which grants them the ability to give mechanical support to the nanofibers. Having these clay nanotubes within the nanofiber matrix amplifies the total rigidity and structural soundness of the material, thereby boosting its capability to bounce back from creases. Moreover, clay nanotubes also have a high surface area enabling them to create robust interfacial bonds with the polymer matrix of the nanofibers. The robust bonding at the interface of the clay nanotubes and the polymer matrix aids in efficiently spreading and relieving mechanical strains, thus avoiding lasting distortion of the substance.

Detailed scrutiny of the results reveals a minor reduction in crease recovery as the vibration speed surpasses 3500 rpm. This phenomenon is likely caused by potential instabilities in the electrospinning device when operating at higher speeds. On the flip side, an overuse of power can lead to increased heat production, which might adversely affect the polymer solution or solvent used during the electrospinning procedure.

Electrical conductivity analysis

The electrical conductivity or resistance of nanowebs is a crucial feature that is frequently taken into account. Incorporating Halloysite clay nanotubes into the final web leads to an enhancement in electrical conductivity. Thorough analysis and comparison were conducted on all samples. The inclusion of nanomaterial at various vibration speeds greatly improved their conductivity. The findings demonstrate that samples B, C, and D exhibited conductivities of 10^{-8}, 10^{-6}, and 10^{-7} Ω/square, respectively. To put it simply, increasing the vibration speed does not have a significant impact on the electrical conductivity.

The findings align with the percolation theory, a theoretical framework used to improve the electrical conductivity of composites that include Halloysite clay nanotubes. This theory elucidates the formation of conductive pathways within the composite material by examining the connectivity and arrangement of the conductive Halloysite clay nanotube particles.

The introduction of clay nanotubes into the nanoweb structure enhances its electrical conductivity properties. These cylindrical nanoparticles consist of layered structures that offer excellent electrical conduction pathways. When integrated into the nanoweb matrix, these clay nanotubes establish a conductive network throughout the material. This network facilitates the movement of electrons, resulting in heightened electrical conductivity.

According to this theory, the achievement of a certain quantity of conductive particles leads to the creation of a continuous network that enhances electrical conductivity. By adjusting the amount and arrangement of particles made from Halloysite clay nanotubes in the composite material, we can regulate electrical conductivity to fulfill specific application requirements. By examining the variables influencing conductivity, scientists can customize the characteristics of nanowebs to meet particular needs. Additionally, the analysis of electrical conductivity offers valuable insights into the fundamental behavior of these materials at the nanoscale level. In summary, the analysis of electrical conductivity in nanowebs that contain clay nanotubes is an essential area of research. It grants us the ability to comprehend and manipulate the electrical properties of these materials for diverse applications.

UV-transmission property

The investigation examined how UV radiation is transmitted within the wavelength range of 200 to 400 nm. The graphs in Figure 3 depict the transmission of UV rays through the nanowebs. The data clearly indicates that the raw samples allow for greater UV transmission compared to the other samples, suggesting a significant distinction. Samples B–D, which contained nanoparticles, showed a decrease in UV transmission when compared to the control sample, indicating that the nanocomposite possessed UV-blocking properties. Conversely, the incorporation of nanoparticles into the nanoweb resulted in improved UV-blocking capabilities compared to the raw sample. This improvement can be attributed to the combined UV absorption of Halloysite clay nanotubes, as well as their ability to scatter and reflect UV radiation, thus preventing it from penetrating the skin and causing harm.

The ability of Halloysite clay nanotube webs to block UV radiation can be explained by multiple factors. Firstly, the distinct structure of Halloysite clay nanotubes enables them to efficiently scatter and absorb UV rays. The cylindrical shape of the nanotubes offers a significant surface area for interaction with UV photons, thereby enhancing the likelihood of absorption. Furthermore, the internal hollow space of the nanotubes serves as a pathway for UV radiation, facilitating effective absorption and scattering across the entire web.

Moreover, the UV-blocking properties of Halloysite clay are also attributed to its chemical composition. Halloysite clay primarily consists of alumina and silica, both of which have demonstrated the ability to absorb UV radiation. Particularly, alumina possesses a high refractive index, enabling it to scatter and reflect UV rays. This scattering and reflection mechanism effectively prevents UV radiation from reaching the skin or any underlying materials beneath the nanotube webs. Additionally, the porous structure of Halloysite clay nanotube webs contributes to their UV-blocking capability. The presence of pores within the nanotube structure enhances light scattering and absorption, creating multiple interfaces for interaction with UV radiation. As a result, the likelihood of UV rays being absorbed or reflected before they can pass through the web is significantly increased.

The ability of Halloysite clay nanotube webs to block UV radiation is primarily due to their distinct structure, chemical composition, and porous characteristics. These attributes enable effective dispersion, reflection, and absorption of UV rays, safeguarding against their detrimental impacts. As a result, Halloysite clay nanotube webs hold great potential for use in products like sunscreens, protective clothing, and coatings for surfaces in need of UV protection.

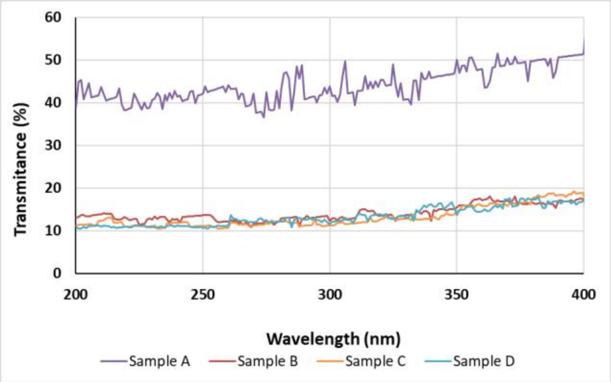

Figure 3. UV transmission diagram.

CONCLUSION

The findings presented in this study suggest that varying the speed of vibration has an impact on the characteristics of the final nanowebs product. Moreover, combining the method of composite fabrication with the use of Halloysite clay nanotubes can improve both the chemical and physical properties. The presence of Halloysite clay nanotube ions in the crystal lattice leads to an increase in the electrical conductivity of the produced samples. These ions can move easily within the lattice, facilitating the flow of electric current. Doping Halloysite clay nanotubes also enhances the crease recovery ability of the samples up to 24%, although there is a slight decrease in crease recovery when the vibration speed exceeds 3500 rpm. This decrease may be attributed to potential instabilities in the electrospinning apparatus at higher speeds. Additionally, the nanocomposite exhibits superior UV-blocking capability compared to the raw samples due to its larger surface area-to-volume ratio (about 75%). Furthermore, the generated samples exhibited enhanced durability and resistance to wear, especially under the influence of a vibration speed reaching 3500 rpm. This research not only provides valuable knowledge and understanding to the textile production industry but also deepens our comprehension of how various treatments can fundamentally modify the properties of nonwoven composites. Future research could explore the integration of Halloysite clay nanotubes with other functional additives to enhance multi-functional properties, such as thermal insulation or flame resistance, in textiles and composites. Additionally, optimizing vibration speeds and treatment methods could lead to tailored applications in smart fabrics, UV-protective clothing, and high-performance composite materials for aerospace or automotive industries.

ACKNOWLEDGEMENTS

This work was supported by the Islamic Azad University-Yazd Branch (Award No.: 1403-01).

REFERENCES

[1] M. Mirjalili, S. Zohoori, J. Nanostruct. Chem. 6 (2016) 207. https://doi.org/10.1007/s40097-016-0189-y.

[2] S. Zohoori, M. Latifi, A. Davodiroknabadi, M. Mirjalili, Pol. J. Chem. Technol. 19 (2017) 56. https://doi.org/10.1515/pjct-2017-0049.

[3] A.S. Lebedev, A.V. Suzdal'tsev, V.N. Anfilogov, A.S. Farlenkov, N.M. Porotnikova, E.G. Vovkotrub, L.A. Akashev, Inorg. Mater. 56 (2020) 20. https://doi.org/10.1134/s0020168520010094.

[4] Y.V. Suvorova, S.I. Alekseeva, M.A. Fronya, I.V. Viktorova, Inorg. Mater. 49 (2013) 1357. https://doi.org/10.1134/s0020168513150089.

[5] A. Al-Attabi, M.A. Abdulhadi, L.R. Al-Ameer, M.D.N. Hussein, S.J. Abdulameer, R.S. Zabibah, A. Fadhil, Int. J.

Mater. Res. 115 (2024) 162. https://doi.org/10.1515/ijmr-2023-0125.

[6] A. Davodiroknabadi, S. Zohoori, R. Talebikatieklahijany, F. Mohammadisaghand, S. Shahsavari, R. Mohammadisaghand, P. Zangeneh, Appl. Biochem. Biotechnol. (2024). https://doi.org/10.1007/s12010-024-04967-7.

[7] G. Esenoğlu, M. Barisik, M. Tanoğlu, M. Yeke, C. Türkdoğan, H. İplikçi, S. Martin, K. Nuhoğlu, E. Aktaş, S. Dehneliler, M.E. İriş, J. Compos. Mater. 56 (2022) 4449. https://doi.org/10.1177/00219983221133478.

[8] N. Sultana, R. Rahman, Emergent Mater. 5 (2022) 145. https://doi.org/10.1007/s42247-021-00326-y.

[9] D. Regmi, J. Choi, J. Xu, ECS Adv. 3 (2024) 4101. https://doi.org/10.1149/2754-2734/ad86cc.

[10] Y. Ghiasi, A. Davodiroknabadi, S. Zohoori, Bull. Mater. Sci. 44 (2021) 89. https://doi.org/10.1007/s12034-021-02406-5.

[11] S. Zohoori, S. Shahsavari, M. Sabzali, S. A. Hosseini, R. Talebikatieklahijany, Z. Morshedzadeh, J. Nat. Fibers. 19 (2022) 8937. https://doi.org/10.1080/15440478.2021.1975600.

[12] M. Asakereh, S. Zohoori, F. Mohammadisaghand, M. Sabzali, R. Mohammadisaghand, B. Soltani, J. Nat. Fibers. 19 (2022) 15552. https://doi.org/10.1080/15440478.2022.2131024.

[13] M. Alghamdi, A. El-Zahhar, Chem. Ind. Chem. Eng. Q. 27 (2021) 35. https://doi.org/10.2298/ciceq200128022a.

[14] R. Subramaniam, A. Eswaran, G. Sivasubramanian, A. Gurusamy, Emergent Mater. 6 (2023) 261. https://doi.org/10.1007/s42247-022-00434-3.

[15] S.M.U. Krithika, K. Mani, S.K. Thangavelu, C.M. Bharathi, K. Saravanan, C. Prakash, AATCC J. Res. 9 (2022) 213. https://doi.org/10.1177/24723444221103675.

[16] E.G. Il'in, A.S. Parshakov, S.Y. Kottsov, M.I. Razumov, D.Y. Gryzlov, Inorg. Mater. 58 (2022) 1130. https://doi.org/10.1134/s002016852211005x.

[17] V. Şimşek, M.O. Çağlayan, Int. J. Mater. Res. 114 (2023) 1047. https://doi.org/doi:10.1515/ijmr-2022-0491.

[18] A. Momeni, A. Ghadi, R. Fazaeli, M. Khavarpour, Int. J. Mater. Res. 114 (2023) 753. https://doi.org/doi:10.1515/ijmr-2021-8516.

[19] H. Salimimofrad, A. Rahbarranji, H. Saghafi, J. Compos. Mater. 58 (2024) 441. https://doi.org/10.1177/00219983231226277.

[20] N. Gupta, R. Maharsia, Appl. Compos. Mater. 12 (2005) 247. https://doi.org/10.1007/s10443-005-1130-6.

[21] S. Zohoori, N. Torabi, E. Gholami, F. Rastgoo, M. Rad, R. Pourheidari, Discover Mater. 4 (2024) 92. https://doi.org/10.1007/s43939-024-00164-9.

[22] O. Josephgbadeyan, T.P. Mohan, K. Kanny, Mater. Today: Proc. 87 (2023) 252. https://doi.org/10.1016/j.matpr.2023.05.352.

[23] S. Zohoori, M. Dolatshahi, M. Pourahmadi, M. Hajisafari, Fiber Integr. Opt. 38 (2019) 1. https://doi.org/10.1080/01468030.2019.1567871.

[24] R. Soltanisarvestani, S. Zohoori, A. Soltanisarvestani, Int. J. Electron. 107 (2020) 444. https://doi.org/10.1080/00207217.2019.1661027.

[25] S. Shamchi, X. Yi, P.M.G.P. Moreira, Appl. Compos. Mater. 30 (2023) 1. https://doi.org/10.1007/s10443-022-10070-z.

[26] N. Rac-Rumijowska, H. Teterycz, Mater. 16 (2023) 3085. https://doi.org/10.3390/ma16083085.

[27] A. Chanda, S.K. Sinha, N. Datla, Composites, Part A. 149 (2021) 106543. https://doi.org/10.1016/j.compositesa.2021.106543.

BEHROOZ SEDIGHI[1]
ABOLFAZL DAVODIROKNABADI[2]
MOHAMMAD SHAHVAZIYAN[1]
MOHAMMADALI SHIRGHOLAMI[1]

[1]Department of Textile Engineering, Yazd Branch, Islamic Azad University, Yazd, Iran

[2]Department of Design and Clothing, Yazd Branch, Islamic Azad University, Yazd, Iran

NAUČNI RAD

UTICAJ BRZINE VIBRACIJE NA NANOKOMPOZIT HALOIZITNIH GLINENIH NANOCEVI

U ovom radu su istraživana nanomreže dobijene tehnikom elektropredenja, uključivanjem nanocevi od haloizitne gline. Glavni fokus je bio na razumevanju kako različite brzine vibracija utiču na karakteristike nanomreže. Korišćenje FESEM-a i mapiranje elemenata, potvrdili su da su nanocevi od haloizitne gline prisutne i dali vredan uvid u strukturu uzoraka. Rezultati u vezi sa električnom provodljivošću su bili izvanredni i pokazali da su tretirani uzorci imali bolja svojstva obnavljanja nabora u odnosu na neobrađene (više od 24%), zahvaljujući prisustvu nanocevi od haloizitne gline i različitim primenjenim brzinama vibracije. Pored toga, uzorci su pokazali poboljšanu sposobnost UV blokiranja do oko 75%, kao i izuzetnu čvrstoću (~33%) i otpornost na habanje (~93%). Sve u svemu, nanokompozitne mreže su pokazale dobra svojstva koja bi se mogla primeniti u različitim industrijama.

Ključne reči: glinene nanocevi; brzina vibracije; elektropredenje; nanomreža.

CI&CEQ
Chemical Industry & Chemical Engineering Quarterly

Available online at
Association of the Chemical Engineers of Serbia *AChE*
www.ache.org.rs/CICEQ

Chem. Ind. Chem. Eng. Q. 31 (4) 325–333 (2025) CI&CEQ

DUŠICA P. ILIĆ[1]
DRAGAN Z. TROTER[1]
JELENA S. STANOJEVIĆ[1]
DRAGAN J. CVETKOVIĆ[1]
IVAN S. RISTIĆ[2]

[1]University of Niš, Faculty of Technology, Leskovac, Serbia

[2]University of Novi Sad, Faculty of Technology, Novi Sad, Serbia

SCIENTIFIC PAPER

UDC 582.794.1:665.52:66.061.3

INTENSIFIED MICROWAVE-ASSISTED HYDRODISTILLATION PRODUCES *TRANS*-ANETHOLE-RICH FENNEL (*FOENICULUM VULGARE* MILL.) FRUIT ESSENTIAL OIL

Article Highlights

- The MWHD isolation technique used was less time-consuming and resulted in a higher oil yield
- *Trans*-anethole-rich and estragole-poor oil expressed better antimicrobial activity
- Produced *Foeniculi aetheroleum* is promising for different industrial applications

Abstract

Fennel fruit (Foeniculim vulgare Mill.) essential oil (FFEO) was isolated from disintegrated plant material by intensified microwave-assisted hydrodistillation approach (MWHD). Isolated FFEO, rich in trans-anethole and low in estragol, was obtained with a 30% higher yield after only 10 min compared to the FFEOs isolated via traditional hydrodistillation (HD). Besides significant differences in the chemical composition, the MWHD-obtained FFEO demonstrated superior antibacterial activity, while its anticandidal activity remained unchanged and identical to HD-obtained FFEOs. MWHD technique also required almost 18 times less electricity consumption and emitted less CO_2 *than the conventional HD, suggesting this approach is more viable for FFEO production on an industrial level. According to these results, the MWHD-obtained FFEO has the potential to be used in the food industry and packaging, for the production of nutraceuticals, biopharmaceuticals, bioherbicides, and cosmetics.*

Keywords: antimicrobial activity; essential oil; fennel fruit; Foeniculi aetheroleum; grinding; microwave-assisted hydrodistillation.

Due to increased consumers' concerns regarding the safety of synthetic chemicals present in various foods and pharmaceutical products, a major shift in industrial research is focused on the replacement of these chemicals with "greener" and natural alternatives. Nowadays, one of these alternatives are essential oils (EOs) derived from different aromatic plants due to their various beneficial biological activities [1]. One example of a commercially valuable EO-bearing industrial crop is fennel (*Foeniculum vulgare* Mill., family Apiaceae). Although native to the Mediterranean and southern Europe, it is cultivated worldwide as a crop with great industrial and economic value, especially in the food and pharmaceutical industries [1]. Fennel is a traditionally highly-valued spice and medicinal herb; some of its reported biological activities include antibacterial, antifungal, anti-inflammatory, analgesic, anti-parasitic, antioxidant, antithrombotic, antidiabetic, antiulcer, antiseptic, antispasmodic, carminative, hepatoprotective and mosquito-repellent [2–6]. Mature fennel fruits (colloquially called seeds) are especially attractive and are extensively investigated as a valuable material in food products, cosmetic, pharmaceutical formulations, culinary additives, flavoring agents, insect- and pest-repellent products, perfumes, beverages, and confectionery [1,4,7]. Their unique aroma, characteristic flavor, and numerous biological activities are attributed to the isolated EOs,

---

Correspondence: D.P. Ilić, University of Niš, Faculty of Technology, Bulevar Oslobođenja 124, 16000 Leskovac, Serbia.
E-mail: dusica.aleksandar@gmail.com

Paper received: 7 August, 2024
Paper revised: 11 October, 2024
Paper accepted: 13 February, 2025

https://doi.org/10.2298/CICEQ240807004I

which have been shown to have antimicrobial, antioxidant, anti-inflammatory, antispasmodic, cytotoxic, and hepatoprotective activities [1,3,4,8–10]. Consequently, fennel fruit essential oil (FFEO), *i.e. Foeniculi aetheroleum* is widely used in many industrial areas (food, cosmetic, and pharmaceutical engineering) and is a promising safe and environmentally friendly bioherbicidal agent [11]; therefore demanding a need to design improved method for its extraction, utilization and global commercialization. FFEOs major compounds include *trans*-anethole, estragole, fenchone, limonene, α-pinene and α-phellandrene [9,12]. Remarkable differences in both the yield and constituents of FFEOs are ascribed to the factors related to the type of cultivated fennel plant (origin, genotype, development stage), cultivation conditions (location, climate, environmental conditions, agricultural practices), plant material pretreatment (powder size, soaking in solvent) and the extraction technique applied [4,7,13].

A crucial step in EO isolation is the selection of an adequate extraction technique that maximizes EO yield while minimizing changes in its functional properties [4]. Traditional, conventional, and most commonly employed EO isolation methods are hydrodistillation (HD), steam distillation, maceration, and expression [4]. However, these methods have some disadvantages: higher energy and solvent consumption, longer duration, lower EO extraction efficiency, yield, and even quality [14,15]. Moreover, some volatile constituents may be degraded due to prolonged extraction times, resulting in their loss and reducing the value of the obtained EO [5,14,15]. Employed toxic solvents that contaminate both the EO and the residual material are environmentally problematic [5,14]; their removal makes the technological process more expensive. Therefore, the focus of researchers is shifted towards the development of new and improved "greener" techniques to enhance the EO extraction efficiency, enable the acquirement of higher-quality EO, and overcome the listed disadvantages.

Microwave-assisted hydrodistillation (MWHD) for EO isolation as a "greener" technique offers numerous advantages compared to classical HD. MWHD is faster, more efficient, cost-effective, environmentally friendly, and surpasses direct plant material/heat source contact, thus ensuring faster and more effective heating, providing higher-quality EO [4,5]. The use of MWHD prevents the thermal decomposition of thermally labile and easily hydrolyzable EO components while improving EO separation [1,3]. Both distilled and indigenous water originating from the plant material serve as heat-transfer fluids [16]. Thanks to the mechanism of MWHD, one of the principal limiting steps regarding sample treatment in classical methods has been overcome. In classical methods, the EO extraction implies transferring the compounds into boiling water and their azeotropic distillation, thus requesting prolonged heating and stirring in boiling water. On the other side, MWHD is based on *in situ* water heating, causing the rupture of oil-containing cellular glands and easier EO release. This microwave superheating phenomenon *via* plant cell distension enables quicker EO liberation, compared to conventional steam distillation [16].

Many factors affect MWHD, *i.e.* quality, moisture content and particle size of raw plant material, nature and amount of solvent, pH, extraction duration, temperature, and microwave power [4]. Among these factors, the importance of milling is frequently addressed, since uncrushed plant material is less prone to EO release in higher yield. The particle size of the EO-bearing plant material reduced *via* physical milling (disintegration) results in increased surface area and enhances HD efficiency [9]. Milling provides a dual benefit regarding MWHD: solvent diffusion into the cells is enhanced, while cells' rupture under microwave irradiation maximizes the extracted EO yield and enables the release of desired targeted components [1].

Among the main FFEO constituents, the dangers of specific alkenylbenzenes must be addressed, as their presence in larger quantities is considered both undesirable and problematic. Daily ingestion of plant-based supplements and products containing alkenylbenzenes, proven genotoxic and carcinogenic in animal studies, must be taken as a serious concern for human health and is, therefore, a high priority for risk management [17]. For instance, phenylpropanoid estragole (synonyms: 1-allyl-4-methoxybenzene; 1-methoxy-4-(2-propenyl)benzene; chavicyl methyl ether; estragon; isoanethole; methyl chavicol, *p*-allylanisole) stirred some controversies due to its genotoxic and carcinogenic effects on animal models [18], specifically as a weak hepatocarcinogenicity inducer in rodents [16]. Excessive FFEO heating causes isomerization of *trans*-anethole into estragole; some MWHD-obtained FFEOs had 5.5% higher estragole content [19]. Moreover, hepatotoxicity of several monoterpenes including camphor and limonene (also detected in FFEOs) was reported [20]. In a toxicological sense, high(er) intake of products containing mentioned compounds must be restricted, while their frequent ingestion in smaller amounts is still under controversial debate [18].

Due to increased global awareness, some consumers especially refuse to buy and consume estragole-containing products. Therefore, it is necessary to design estragol-free FFEOs' isolation processes, while simultaneously ensuring maximization of their yield and minimization of both time and power consumption.

In this work, the following steps are covered: (a) proposition of the "greener" intensified MWHD technique for obtaining *trans*-anethole-rich and estragole-poor FFEO; (b) chemical characterization of the isolated FFEO; (c) comparison of energy consumption, economic and environmental impacts of the proposed MWHD and traditional HD technique and (d) evaluation of the MWHD-obtained FFEO's antimicrobial activity, with comparison to those reported for FFEOs isolated *via* traditional HD.

MATERIALS AND METHODS

Plant material and chemicals

Raw and non-processed mature fennel fruits were picked and collected from the mountain field in Stara Planina, Serbia (43°22′10″N 22°36′32″E, collection period July 2023) and kept in a paper bag before usage at laboratory temperature (20 °C). The plant material was ground in an electric grinder (laboratory coffee mill Gorenje, Slovenia) for 60 s and sieved on a sieve shaker (0.5 mm fraction). Figure S1 (Supplementary materials) represents the visual comparison between raw and powdered fennel fruits. The moisture content of the raw and powdered fennel fruits was determined by drying in an oven at 105 °C to constant mass. The pulverized material was poured into a sealed dark glass flask (previously twice disinfected with 70% ethanol) and refrigerated at 4 °C in the dark. The pulverized samples were stored for 24 h.

Ethanol (70%, Zorka Pharma, Šabac, Serbia) and commercial distilled water (DCP Hemigal, Leskovac, Serbia) were used. Dimethylsulfoxide, diethyl ether, and anhydrous Na_2SO_4 (both ≥99%) were purchased from Sigma-Aldrich (Munich, Germany), while a sterile saline solution was from Hemofarm A.D. (Vršac, Serbia).

MWHD procedure

In a round-bottom one-necked glass flask 50 g of pulverized fennel fruit was mixed with 500 cm^3 of distilled water, attached to a Clevenger-type apparatus with a condenser, and subjected to microwave irradiation in a "Discover" microwave reactor (CEM, Matthews, North Carolina, USA). The total duration of the process was 20 min at 100 °C (operating frequency 2.45 GHz, power 500 W). Temperature control was performed by using an infrared mass measurement system and maintained constant during the process. The obtained FFEO was dehydrated with anhydrous Na_2SO_4, collected in a dark bottle, sealed, and stored at 4 °C prior to analyses. The FFEO yield was expressed in g of oil per 100 g of the plant material (g FFEO/100 g p.m.). The determination was performed three times and the data were expressed as mean ± standard deviation.

Identification of components

The qualitative and quantitative analyses (GC-MS: gas chromatography-mass spectrometry) and GC-FID: gas chromatography-flame ionization detection) conditions were identical to those described in Ilić et al. [9]. The determination was triplicated and the data were expressed as mean ± standard deviation.

Evaluation of energy demands and environmental impacts

Energy consumption during the MWHD process was calculated by equation:

$$E = P \cdot t \tag{1}$$

where E, P, and t denote the energy consumption, the applied power, and MWHD duration, respectively. The estimated quantity of the emitted CO_2 during MWHD was provided by the equation:

$$E_{CO_2} = 800 \cdot E = 800 \cdot P \cdot t \tag{1}$$

where E_{CO2} is CO_2 mass.

Antimicrobial tests

Antibacterial activity was tested against Gram(+) (*Staphylococcus aureus* ATCC 25923, *Listeria monocytogenes* ATCC 19118, *Bacillus subtilis* ATTC 6633) and Gram(-) bacteria (*Proteus vulgaris* ATCC 8427, *Escherichia coli* ATCC 25922, *Klebsiella pneumoniae* ATCC 700603, *Pseudomonas aeruginosa* ATTC 2785, *Salmonella typhimurium* CICC 10420). Anticandidal activity was evaluated against *Candida albicans* (ATCC 2091). The details of both the disc diffusion method and conditions used for minimal inhibitory concentration (MIC) determination were identical and detailed in Ilić *et al.* [9]. Tests were triplicated and the results were given as mean ± standard deviation.

Statistical analysis

The SPSS 23.0 (IBM, USA) software performed the analysis of variance (ANOVA) combined with Tukey's multiple comparison test (the significance level $p < 0.05$).

RESULTS AND DISCUSSION

FFEO yield, qualitative and quantitative composition

The determined moisture content of the raw and powdered fennel fruits was 5.43 ± 0.01 % and 5.33 ± 0.01 %, respectively.

During the first 10 min of MWHD, the FFEO yield rose exponentially, achieving 5.2 ± 0.01 g/100 g of plant material after 10 min. Further prolongation of the process had no significant impact on the FFEO yield, with a maximum value of 5.21 g/100 g of plant material after 20 min; therefore, 10 min was taken as the optimal time. MWHD-obtained FFEO yield after 10 min was 30% and 44.4% higher than the FFEO yield obtained by Clevenger-type HD from disintegrated and non-disintegrated fennel fruits after 3 h in our previous study [9]. MWHD enhances FFEO yield dually. Microwaves decrease the degree of oxidation and hydrolyzation by speeding the process and requiring lower solvent quantity while in the plant material heat is transferred from the center to the outside, causing higher pressure into the FFEO-bearing cells, resulting in their quick rupture [13].

By applying different modified MWHD methods, it is clear that a combination of different factors (the nature and origin of the fennel fruit, milling, moisture content, microwave power, solid-to-liquid ratio, and duration of the process) are crucial factors that determine the improvement in terms of the FFEOs yield, as well as their chemical compositions [1,3–5,13–16,21]. After pulverization, the smaller particle size of crushed fennel seed provides a higher surface area, thus more FFEO-bearing secretory canals are exposed [1,3–5,13]. The optimal moisture content of the raw material is especially beneficial. Higher moisture content leads to an increased dielectric heating rate, so FFEO release into the solvent is easier. The residual water contained in the fennel seeds evaporates rapidly, ensuring FFEO is extracted more quickly [4,13,14,21]. Microwaves make polar compounds in fennel fruits (including water) prone to ion conduction and dipole rotation, resulting in heating that disintegrates the plant cell membranes and FFEO release [4,13,14,21]. Precautions regarding excessive microwave power must be taken seriously since thermal degradation of the fennel fruits decreases the MWHD efficiency, FFEO yield, and quality [13,14,16]. An adequate solid-to-liquid ratio ensures the highest FFEO yield due to the appropriate dielectric heating of the solvent. Higher liquid quantity prolongs MWHD and produces unnecessary waste, while insufficient liquid poses a risk in raw material combustion and reduces the MWHD efficiency [13–16]. Sufficient MWHD duration is inevitable for the completion of the process and optimal release of each FFEO component, while prolonged irradiation decreases the FFEO yield and MWHD efficiency [1,4,13–16,21].

GC-MS and GC-FID chromatograms of FFEO isolated by MWHD are given in Figures S2 and Figure S3, respectively. Although the qualitative composition of FFEOs was identical, significant differences regarding the quantitative composition are noticed (Table 1).

Table 1. Comparison of FFEOs chemical composition (area %) isolated by MWHD and HD.

No.	Retention time, min	Compound	Type of compound	MWHD	HD, disintegrated fennel fruit [9]	HD, non-disintegrated fennel fruit [9]
1	4.90	α-Pinene	Monoterpene, bicyclic	<0.05 cG	2.04 ± 0.13 aE	0.51 ± 0.05 bE
2	5.10	Camphene	Monoterpene, bicyclic	<0.05 bG	0.16 ± 0.04 aI	0.05 ± 0.04 bF
3	5.36	Sabinene	Monoterpene, bicyclic	<0.05 aG	0.09 ± 0.04 aI	<0.05 aF
4	5.49	β-Myrcene	Monoterpene, acyclic	<0.05 cG	1.03 ± 0.04 aF	0.41 ± 0.04 bE
5	5.74	α-Phellandrene	Monoterpene, monocyclic	<0.05 cG	0.36 ± 0.04 aH	0.15 ± 0.04 bF
6	5.99	*p*-Cymene	Monoterpene, aromatic	<0.05 aG	0.10 ± 0.04 aI	0.09 ± 0.05 aF
7	6.06	Limonene	Monoterpene, monocyclic	3.08 ± 0.07 aC	2.32 ± 0.07 bD	1.09 ± 0.04 cD
8	6.45	γ-Terpinene	Monoterpene, monocyclic	0.75 ± 0.11 aE	0.72 ± 0.06 aG	0.38 ± 0.03 bE
9	6.91	Fenchone	Oxygenated monoterpene, bicyclic ketone	4.71 ± 0.06 cB	23.14 ± 0.06 aB	22.59 ± 0.05 bB
10	7.72	Camphor	Oxygenated monoterpene, bicyclic ketone	<0.05 bG	0.50 ± 0.07 aH	0.51 ± 0.04 aE
11	8.36	Estragole	Phenylpropanoid	<0.05 bG	2.58 ± 0.05 aC	2.67 ± 0.1 aC
12	9.09	*cis*-Anethole	Phenylpropanoid	0.99 ± 0.05 aD	0.12 ± 0.05 bI	0.18 ± 0.06 bF
13	9.15	*p*-Anisaldehyde	Phenylpropanoid	0.39 ± 0.05 aF	0.14 ± 0.06 bI	0.36 ± 0.04 aE
14	9.58	*trans*-Anethole	Phenylpropanoid	90.06 ± 0.06 aA	64.87 ± 0.07 cA	69.89 ± 0.06 bA
			Monoterpenes (1-8)	3.81 ± 0.108 bC	6.82 ± 0.366 aC	2.68 ± 0.231 cC
			Oxygenated Monoterpenes (9, 10)	4.71 ± 0.06 cB	23.64 ± 0.113 aB	23.1 ± 0.09 bB
			Phenylpropanoids (11-14)	91.4 ± 0.13 aA	67.71 ± 0.21 cA	73.1 ± 0.26 bA
			Total	99.92 ± 0.02 a	98.17 ± 0.68 b	98.88 ± 0.58 a,b

Different letters indicate statistically different ($p < 0.05$) values in the same row (lower case letters) and in the same column (upper case letters) by Tukey's multiple range test.

Almost the total amount of MWHD-obtained FFEO was constituted of 14 volatile components, with *trans*-anethole as the most abundant (90%). Five minor components (less than 10% of FFEO) were in this order: fenchone > limonene > *cis*-anethole > *γ*-terpinene > *p*-anisaldehyde, while eight compounds were detected in traces (*α*-pinene, camphene, sabinene, myrcene, *α*-phellandrene, *p*-cymene, camphor and estragole). MWHD-obtained FFEO contained more *trans*-anethole, *cis*-anethole, and limonene, while fenchone was present in a lower quantity. As in the case regarding the FFEO yield, the nature and origin of the fennel fruit play a key role in many total compounds constituting the FFEO (Table 2).

Table 2. Literature review of the yield, MWHD conditions, and chemical composition of the main FFEO compounds from different origins.

Origin	Pretreatment method	Isolation method*	Operating conditions	Yield, %	Time, min	Number of components	Abundant compounds (%)	Reference
Serbia	Milling	MWHD	500 W, 0.5 mm particle size, liquid/solid ratio 10 mL/g, 100 °C	5.2±0.1	10	14	*Trans*-anethole (90.06 ± 0.06), fenchone (4.71 ± 0.06), limonene (3.08 ± 0.07), *cis*-anethole (0.99 ± 0.05), *γ*-terpinene (0.75 ± 0.11), *p*-anisaldehyde (0.39 ± 0.05)	This paper
Algeria	Freeze-drying, 48 h or raw seeds, milling	MWHD	305.9282 W, raw non-dryed seeds, 333.4673 µm particle size, water pH 6, liquid/solid ratio 6.77 mL/g	0.8999±0.02	20	19	*Trans*-anethole (88.7 ± 0.02), camphor (4.1 ± 0.03), estragole (2.9 ± 0.03), anisketone (0.6 ± 0.02), limonene (0.2 ± 0.01), fenchone (0.2 ± 0.01)	[4]
Medite-rranean Region	Milling	MWHD	800 W, 10 min + 500 W, 50 min	2.8	60	4	*Cis*-anethol (65), fenchone (28), limonene (2.2), pinene (1.5)	[5]
Turkey	Grinding	MWHD	10 min, 800 W, 100 °C + 50 min, 500 W, 100 °C	1.6	60	34	*Trans*-anethole (85.2), estragole (4.7), limonene (4.1), α-fenchone (1.5), anisaldehyde (1.5), carvone (1)	[16]
	None			1.2	60	34	*Trans*-anethole (85.7), estragole (4.9), limonene (2.2), α-fenchone (1.4), anisaldehyde (2.4), carvone (1.8)	
China	Drying at room temperature, milling, soaking in water	DCMAHD	576 W, soaking time 1.82 h, 60-80 mesh particle size, liquid/solid ratio 8.69 mL/g	2.82±0.09	34	27	*Trans*-anethole (88.28), estragole (4.25), *D*-limonene (2.04), fenchone (2.03)	[1]
India	Drying	Coaxial MWHD	500 W, 9 min, 250 rpm + 300 W, 120 min, liquid/solid ratio 5 mL/g	0.83	120	17	*Trans*-anethole (79), fenchone (10.9), estragole (4.2), limonene (3.2)	[21]
Tunisia	Drying, milling, soaking in water at room temperature	ESFME	600 W, soaking time 20 min, particle size <2 mm, liquid/solid ratio 5 mL/g	0.48	30	9	*Cis*-anethole (83.07), *α*-terpinolene (10.9) eucalyptol (2.95), *γ*-terpinene (2.11)	[3]
		SFME		0.46	37	7	*Cis*-anethole (83.63), *α*-terpinolene (11.42), γ-terpinene (2.17), eucalyptol (2.12)	
China	Soaking in 73.2% [C$_4$MIM]Br, 240 W, 6 min	MILT-HD	240 W, liquid/solid ratio 6 mL/g, 100 ℃	0.0363 mL/g	76.2	11	Anethole (48.29), estragole (28.71), *D*-Limonene (8.32), fenchone (1.82), γ-terpinene (1.53), α-pinene (1.25), anisic aldehyde (0.83)	[15]
North Gujarat	Milling, soaking in water	IMAE	140 W, 0.4 mm particle size, 500 g material + 20 g carbonyl Fe powder (99.16% Fe content, 3.5 µm)	0.5	25	9	*Cis*-anethole (70), *L*-fenchone (6), α-limonene (3.1), myrcene (1.3), methyl chevicol (1.2), γ-terpenene (1.1), anisic aldehyde (1), caprinone (0.9)	[14]
China	Milling, drying at 40 ℃ for 48 h	DCME	600 W, 40-75 mesh particle size, liquid/solid ratio 5.6 mL/g	1.172±0.011	27	25	Estragole (64.25), limonene (10.11), fenchone (5.15), *trans*-anethole (3.98), *D*-carvone (1.75), fenchyl acetate (1.01)	[13]
	Milling, soaking in water for 8 min	SCME	600 W, liquid/solid ratio 5.6 mL/g	1.068±0.011	27	26	Estragole (58.61), limonene (13.06), fenchone (5.08), *trans*-anethole (4.84), *D*-carvone (1.77), fenchyl acetate (1.27)	

*MWHD, microwave-assisted hydrodistillation; DCMAHD, double-condensed microwave-assisted hydrodistillation; Coaxial MWHD, coaxial microwave-assisted hydrodistillation. * ESFME, enhanced solvent-free microwave extraction using double walled microwave reactor; SFME, solvent-free microwave extraction using the single-walled reactor; MILT-HD, microwave-assisted ionic liquids treatment followed by hydrodistillation; IMAE, improved microwave-assisted extraction; DCME, dual-cooled microwave extraction; SCME, single-cooled microwave extraction.

The applied MWHD approach was selective for producing phenylpropanoid-rich FFEO, followed by oxygenated monoterpenes and lastly monoterpenes. This is explained by differences in their dipolar moments. Phenylpropanoids and oxygen-containing constituents have higher dipolar moments than monoterpene hydrocarbons, causing more vigorous interaction with microwaves and facilitating their isolation *via* microwave extraction [3,4]. In that sense, *trans*-anethole, as an oxygenated compound with a higher dipolar moment, was extracted more easily, as a consequence of the MWHD-specific heating mechanism. Since the microwaves' electromagnetic energy is converted into heat through two mechanisms (ionic conduction and dipole rotation), alignment of the molecules with a dipole moment in the electric field causes frequent changes of direction, leading to particles' collisions and resulting in the liberation of heat energy. This ultimately causes the enhanced breakdown of hydrogen bonds by the dipole rotation of the molecule, enhancing the extraction process [22]. Regarding MWHD, the application of water as a microwave irradiation absorber is crucial, since inadequate or insufficient water content cannot reduce or prevent undesirable and harmful chemical reactions (such as hydrolyzation, oxidation, and degradation of volatile compounds), which do not occur during conventional hydrodistillation [3].

From the industrial point of view, phenylpropanoids and oxygen-containing constituents are more valuable and desirable since these compounds are more fragrant and beneficial for the production of EOs that are more olfactively appealing to consumers [3,4,13,16]. MWHD was found especially beneficial for extracting larger quantities of flavourful and fragrant fenchone, whose presence in EOs, and nutritional, cosmetic, and pharmaceutical products increases their market value [21]. The amount of fenchone, bicyclic ketone, was shown to increase with the MWHD duration time, therefore its amount in FFEO produced after 120 min is much higher [21] than in our study. Therefore, strict control regarding MWHD time consumption is crucial for obtaining FFEO rich in specific compounds (phenylpropanoids or oxygenated monoterpenes). According to Koşar et al. [16] crushed fennel fruits were found to be limonene-richer than raw fruits; however, contrary to this study, the applied "shock-and-treat" MWHD technique enabled adequate microwave energy intensity for limonene extraction from the plant matrix.

Some Mediterranean [5], Indian [14], Tunisian [3], and Chinese [15] MWHD-obtained FFEOs had fewer compounds than the isolated Serbian FFEO, while some FFEOs from India [21], Algeria [4], China [1,13] and Turkey [16] were composed of more substances. *Trans*-anethole was also the most prevalent constituent, as well as containing fewer amounts of estragole, in MWHD-obtained FFEOs from Algeria [4], China [1], Turkey [16], and India [21]. *Cis*-anethole was the most prevalent in Tunisian [3], Indian [14], and Mediterranean [5] MWHD-obtained FFEOs, while the Chinese FFEOs contained high amounts of estragole [13,15].

Estimation of the energy and environmental impact of the proposed MWHD technique

To estimate the possibility of applying the proposed MWHD technique on an industrial level, factors regarding energy demands and environmental impact are presented in Table 3.

Table 3. Comparison of the proposed methodology.

Factor	Unit	MWHD	HD, disintegrated fennel fruit	HD, non-disintegrated fennel fruit
Electric power	W	500	500	500
Temperature	K	373.15	373.15	373.15
Thermal conductance	kW/K	0.00134	0.00134	0.00134
Duration	min	10	180	180
Liquid-to-solid ratio	mL/g	10	10	10
Electricity consumption	kW·h	0.0835	1.5	1.5
E_{CO2}	g CO_2	66.8	1200	1200
Heat capacity	kW·h/K	0.000224	0.00402	0.00402
Mass of water per g p.m.	kg	0.01	0.01	0.01
Specific heat capacity	kW·h/kg·K	0.0224	0.402	0.402
FFEO yield	g/100 g d.w.	5.2 ± 0.1 a	4 ± 0.2 b	3.6 ± 0.3 b
FFEO yield per kW·h	g/100 g d.w./kW·h	62.275 ± 1.2 a	2.67 ± 0.13 b	2.4 ± 0.2 b
FFEO yield per kW·h·K	g/100 g d.w./kW·h·K	0.167 ± 0.0032 a	0.00715 ± 0.00036 b	0.0064 ± 0.00054 b

Row values (different small letters) are significantly different ($p < 0.05$) by Tukey's multiple range tests.

Considering that microwave heating is uniform and quicker compared to classical heating, combined with the fact that the cellular heating is caused by the moisture present in the plant tissue (thus produced vapor pressure disrupts the cellular walls), it can be concluded that the extraction of the components is both facilitated and accelerated. Reduction in solvent consumption and extraction time, together with lower energy consumption, are undoubtedly environmental advantages, establishing the MWHD as a "green" extraction technique [22,23]. Besides the fact that water is one of the most suitable solvents for microwave extraction, the potential of parameters' (time, power, and temperature) control, the possibilities of stirring and high-temperature application, and excluding the need for adding drying agents (since water absorbs microwaves) are also additional advantages worth mentioning [22,23]. So, the reduced cost of the proposed MWHD technique is beneficial in terms of time, energetic demands, and environmental impacts. MWHD technique provided a higher FFEO yield after only 10 min, compared to the 3 h required for conventional HD. MWHD technique also required almost 18 times less electricity consumption than the conventional HD; thus emitted less CO_2. For 1 kW·h 23.3 times more FFEO yield was produced via the MWHD technique, concluding this method is fast, cleaner, and promising for the production of *trans*-anethole-rich and estragole-poor FFEO on a larger industrial scale. The isolated FFEO has great potential regarding its utilization as a natural antimicrobial agent. It can be used to prolong the shelf life of meat since commercial fennel EOs have already been proven as natural antimicrobial agents [24]. The combination of EOs isolated from plants of different origins and the synergistic activity of their main and minor compounds is very interesting, opening a wide research field focused on utilizing FFEO as a potential natural preservative for different types of food. FFEOs' broader spectrum of potential application has been addressed, more specifically as an anticorrosive agent in the metallurgy, machine, automobile, and similar industrial branches, since these oils suppress corrosion of the steel plates [25].

Besides valuable FFEO, the suggested process also generates condensed residual herbal water and solid plant residual material, both of which can be further valorized into market-desirable products. Since residual water contains non-volatile organic bio-components, it can be considered aromatic water, thus applicable in various industries [26]; left-over plant material, constituted of insoluble cellulose-based components, represents biomass feedstock for the production of different chemicals, energy, animal food, and biofertilizers [27]. In this manner, the whole technological process can be scaled up on an industrial level, making it more profitable.

Antimicrobial activities

C. albicans was the most sensitive microorganism because it was completely cleared from a petri dish after treatment with the MWHD-obtained FFEO. Identical results were reported for previously HD-obtained FFEOs [9]. However, the MWHD-obtained FFEO showed better antibacterial activity compared to HD-obtained FFEOs (Table 4). Among Gram(+) bacteria, *B. subtilis* was the most sensitive, while the inhibition zone values for *S. aureus* and *L. monocytogenes* were similar. Some Gram(-) bacteria were also sensitive, namely *S. typhimurium*, *E. coli* and *P. vulgaris*. The lowest sensitivities were reported for *P. aeruginosa* and *K. pneumoniae*.

Table 4. Zones of bacterial growth inhibition (mm) caused by FFEOs isolated by MWHD and HD.

Microorganism	MWHD	HD, disintegrated fennel fruit [9]	HD, non-disintegrated fennel fruit [9]
S. aureus	28 ± 0.8 a C,D	23 ± 0.5 b B,C	19 ± 0.8 c B
L. monocytogenes	29 ± 0.9 a C	24 ± 1.1 b B	18 ± 1.0 c B,C
B. subtilis	34 ± 0.9 a A	32 ± 1.1 a A	28 ± 0.9 b A
P. vulgaris	28 ± 1.3 a C,D	23 ± 0.8 b B,C	19 ± 1.3 c B
E. coli	30 ± 0.6 a B,C	20 ± 1.1 b D,E	18 ± 0.6 b B,C
K. pneumoniae	26 ± 0.5 a D,E	21 ± 1.4 b C,D,E	19 ± 0.5 b B
P. aeruginosa	25 ± 1.0 a E	19 ± 0.7 b E	16 ± 1.0 c C
S. typhimurium	32 ± 0.5 a A,B	22 ± 0.8 b B,C,D	16 ± 0.8 c C

Different letters indicate statistically different ($p < 0.05$) values in the same row (lower case letters) and in the same column (upper case letters) by Tukey's multiple range test.

The lowest MIC values for *C. albicans*, *B. subtilis*, and *S. typhimurium* reflect the highest susceptibility of these pathogens, followed by *S. aureus* and *P. vulgaris* (Table 5). When MWHD-obtained FFEO was used, all MIC values were lower than those reported for previously HD-obtained FFEOs [9]. According to these results, MWHD-obtained FFEO can be utilized as a safer additive in food products, beverages, pharmaceuticals, nutriceuticals, and cosmetic formulations, preventing microbial growth, spoilage, and oxidative deterioration.

FFEO was previously reported as antifungal against *C. albicans* [28], *C. gloeosporioides*, *P. capsici*, *S. sclerotiorum,* and *F. fujikuroi* [1] and antibacterial against *S. typhimurium*, *E. coli*, *L. monocytogenes* and *S. aureus* [13]. FFEOs' constituents that are both of lower lipophilicity and mass penetrate the fungal cell membrane more easily, resulting in its disintegration; this explains FFEOs' prominent and diverse fungicidal activities [1]. Contrary to Gram-positive bacteria, weaker FFEO's antibacterial activity against Gram-negative bacteria is ascribed to their protective lipopolysaccharide-containing external membrane [29]. MWHD-obtained FFEO's improved antimicrobial activity can be ascribed to its specific chemical composition. The most abundant *trans*-anethole and minor-present fenchone, limonene, estragole, and *α*-pinene in their pure form were established as excellent antimicrobials [12,29]. In addition, synergistic effects occurring among *trans*-anethole and minor components may contribute to FFEO's better antimicrobial activity.

Table 5. MIC values (µg/ml) for FFEOs isolated by MWHD and HD.

Microorganism	MWHD	HD, disintegrated fennel fruit [9]	HD, non-disintegrated fennel fruit [9]
S. aureus	20 aB	50 bC	75 cC
L. monocytogenes	50 aE	90 bE	Non-treated
B. subtilis	15 aA	25 bA	25 bA
P. vulgaris	30 aC	50 bC	50 bB
E. coli	40 aD	75 bD	100 cD
K. pneumoniae	50 aE	75 bD	100 cD
P. aeruginosa	75 aF	>100 bF	>100 bE
S. typhimurium	15 aA	30 bB	Non-treated
C. albicans	15 aA	25 bA	25 bA

Different letters indicate statistically different ($p < 0.05$) values in the same row (lower case letters) and in the same column (upper case letters) by Tukey's multiple range test.

CONCLUSION

MWHD technique at 500 W power for 10 min (intensified "shock-and-treat" approach) resulted in obtaining *trans*-anethole-rich and estragole-poor FFEO from disintegrated fennel fruits while demanding less energy. Considering grouped compounds, FFEO contained more than 90% phenylpropanoids, less than 5% oxygenated monoterpenes, and close to 4% monoterpene hydrocarbons. Besides retaining its anticandidal potency, MWHD-obtained FFEO showed better antibacterial activity against *B. subtilis*, *S. aureus*, *L. monocytogenes*, *S. typhimurium*, *E. coli*, *P. vulgaris*, *P. aeruginosa*, and *K. pneumoniae*, compared to HD-obtained FFEOs. These results suggest that the MWHD-obtained FFEO may be considered as safer antimicrobial and spoilage-preventive additive for different industrial products. Moreover, the proposed technique is "green", safe, cheap, simple, effective, quick, and selective, thus promising for EO isolation from other aromatic plants.

ACKNOWLEDGEMENTS

This work was supported by the Republic of Serbia - Ministry of Science, Technological Development and Innovation (Programs for financing scientific research: 451-03-65/2024-03/200133 and 451-03-66/2024-03/200133 assigned to the University of Niš, Faculty of Technology, Leskovac, and 451-03-47/2023-01/200134 assigned to the University of Novi Sad, Faculty of Technology).

LIST OF SYMBOLS AND ABBREVIATIONS

Coaxial MWHD	coaxial microwave-assisted hydrodistillation
DCMAHD	double-condensed microwave-assisted hydrodistillation
DCME	dual-cooled microwave extraction
EO	essential oil
ESFME	enhanced solvent-free microwave extraction using a double-walled microwave reactor
FFEO	fennel fruit essential oil
HD	hydrodistillation
IMAE	improved microwave-assisted extraction
MIC	minimal inhibitory concentration
MILT-HD	microwave-assisted ionic liquids treatment followed by hydrodistillation
MWHD	microwave-assisted hydrodistillation
SCME	single-cooled microwave extraction
SFME	solvent-free microwave extraction using the single-walled reactor

REFERENCES

[1] F. Chen, Y. Guo, J. Kang, X. Yang, Z. Zhao, S. Liu, Y. Ma, W. Gao, D. Luo, Ind. Crops Prod. 144 (2020) 112052. https://doi.org/10.1016/j.indcrop.2019.112052.

[2] M. Akhbari, R. Kord, S.J. Nodooshan, S. Hamedi, Nat. Prod. Res. 33(11) (2019) 1629–1632. https://doi.org/10.1080/14786419.2017.1423310.

[3] H. Benmoussa, A. Farhat, M. Romdhane, J. Bouajila, Arabian J. Chem. 12(8) (2019) 3863–3870. https://doi.org/10.1016/j.arabjc.2016.02.010.

[4] H. Boudraa, N. Kadri, L. Mouni, K. Madani, J. Appl. Res. Med. Aromat. Plants 23 (2021) 100307. https://doi.org/10.1016/j.jarmap.2021.100307.

[5] F.M. Hammouda, M.A. Saleh, N.S. Abdel-Azim, K.A. Shams, S.I. Ismail, A.A. Shahat, I.A. Saleh, Afr. J. Tradit., Complementary Altern. Med. 11(2) (2014) 277–279. http://doi.org/10.4314/ajtcam.v11i2.8.

[6] M.M. Khaleil, M.M. Alnoman, E.S.A. Elrazik, H. Zagloul, A.M.A. Khalil, Biology 10(8) (2021) 696. https://doi.org/10.3390/biology10080696.

[7] I. Telci, I. Demirtas, A. Sahin, Ind. Crops Prod. 30(1) (2009) 126–130. https://doi.org/10.1016/j.indcrop.2009.02.010.

[8] A. Ghasemian, A.H. Al-Marzoqi, S.K.S. Mostafavi, Y.K. Alghanimi, M. Teimouri, J. Gastrointest. Cancer 51(1) (2020) 260–266. https://doi.org/10.1007/s12029-019-00241-w.

[9] D.P. Ilić, L.P. Stanojević, D.Z. Troter, J.S. Stanojević, B.R. Danilović, V.D. Nikolić, L.B. Nikolić, Ind. Crops Prod. 142 (2019) 111854. https://doi.org/10.1016/j.indcrop.2019.111854.

[10] M. Khazaei, D. Dastan, A. Ebadi, Food Biosci. 41 (2021) 100972. https://doi.org/10.1016/j.fbio.2021.100972.

[11] P. Kaur, S. Gupta, K. Kaur, N. Kaur, R. Kumar, M.S. Bhullar, Ind. Crops Prod. 168 (2021) 113601. https://doi.org/10.1016/j.indcrop.2021.113601.

[12] F. Kalleli, I.B. Rebey, W.A. Wannes, F. Boughalleb, M. Hammami, M. Saidani Tounsi, M. M'hamdi, J. Food Biochem. 43(8) (2019) e12935. https://doi.org/10.1111/jfbc.12935.

[13] L.J. Dong, X.-.Y. Huang, Z.-.F., Wei, B.-.S. Zhao, H.-.Y. Yang, Flavour Fragrance J. 37(7) (2022) 154–162.

https://doi.org/10.1002/ffj.3691.

[14] J.B. Patel, B. Patel, R.K. Patel, B.H. Patel, J. Pharm. Sci. Biosci. Res. 2(4) (2012) 176–178. http://www.jpsbr.org/index_htm_files/4_JPSBR12RS100.pdf.

[15] G. Shi, L. Lin, Y. Liu, G. Chen, A. Yang, Y. Wu, Y. Zhou, H. Li, Molecules 26(11) (2021) 3169. https://doi.org/10.3390/molecules26113169.

[16] M. Koşar, T. Özek, M. Kürkçüoglu, K.H.C. Başer, J. Essent. Oil Res. 19(5) (2007) 426–429. https://doi.org/10.1080/10412905.2007.9699943.

[17] S.J.P.L. van den Berg, P. Restani, M.G. Boersma, L. Delmulle, I.M.C.M. Rietjens, Food Nutr. Sci. 2(9) (2011) 989–1010. http://doi.org/10.4236/fns.2011.29134.

[18] A. Eisenreich, M.E Götz, B. Sachse, B.H. Monien, K. Herrmann, B. Schäfer, Foods 10(9) (2021) 2139. https://doi.org/10.3390/foods10092139.

[19] Á. Kapás, C.D. András, T.Gh. Dobre, E. Vass, G. Székely, M. Stroescu, S. Lányi, B. Ábrahám, UPB Sci. Bull., Ser. B 73(4) (2011) 113–120. https://www.scientificbulletin.upb.ro/rev_docs_arhiva/full69807.pdf.

[20] T. Zárybnický, I. Boušová, M. Ambrož, L. Skálová, Arch. Toxicol. 92(1) (2018) 1–13. https://doi.org/10.1007/s00204-017-2062-2.

[21] J. González-Rivera, C. Duce, D. Falconieri, C. Ferrari, L. Ghezzi, A. Piras, M.R. Tine, Innovative Food Sci. Emerging Technol. 33 (2016) 308–318. http://doi.org/10.1016/j.ifset.2015.12.011.

[22] M.S. Uddin, S. Ferdosh, M.J.H. Akanda, K. Ghafoor, A.H. Rukshana, M.E. Ali, B.Y. Kamaruzzaman, M.B. Fauzi, S. Hadijah, S. Shaarani, M.Z.I. Sarker, Separation Sci. Technol. 53 (2018) 2206–2223. https://doi.org/10.1080/01496395.2018.1454472.

[23] M. Llompart, M. Celeiro, T. Dagnac, TrAC Trends Anal. Chem. 116 (2019) 136–150. https://doi.org/10.1016/j.trac.2019.04.029.

[24] S.D. Đurović, D. Micić, M. Jovanović, B. Dojčinović, D. Mitić Ćulafić, Y.A. Smyatskaya, P. Riabov, R. Božović, Food Biosci. 61 (2024) 104901. https://doi.org/10.1016/j.fbio.2024.104901.

[25] M. Pencheva, M. Nikolova, S. Damianova, M. Dushkova, N. Menkov, A. Stoyanova, Appl. Sci. 14 (2024) 7240. https://doi.org/10.3390/app14167240.

[26] L. Petigny, S. Périno, M. Minuti, F. Visinoni, J. Wajsman, F. Chemat, Int. J. Mol. Sci. 15(5) (2014) 7183–7198. http://doi.org/10.3390/ijms15057183.

[27] N. Rombaut, A.S. Tixier, A. Bily, F. Chemat, Biofuels, Bioprod. Biorefin. 8(4) (2014) 530–544. https://doi.org/10.1002/bbb.1486.

[28] R.H. Bassyouni, I.E. Wali, Z. Kamel, M.F. Kassim, J. Herb. Med. 15 (2019) 100227. http://dx.doi.org/10.1016/j.hermed.2018.08.002.

[29] M.H. Farjam, F. Barzegari, Nat. Prod. 10(2) (2014) 44–48. https://www.tsijournals.com/articles/comparison-of-chemical-composition-and-antibactrial-activity-of-essential-oils-extracted-by-microwaveassisted-hydrodisti.pdf.

DUŠICA P. ILIĆ[1]
DRAGAN Z. TROTER[1]
JELENA S. STANOJEVIĆ[1]
DRAGAN J. CVETKOVIĆ[1]
IVAN S. RISTIĆ[2]

[1]University of Niš, Faculty of Technology, Leskovac, Serbia

[2]University of Novi Sad, Faculty of Technology, Novi Sad, Serbia

NAUČNI RAD

INTENZIVNIJA MIKROTALASNA HIDRODESTILACIJA U PROIZVODNJI ETARSKOG ULJA PLODA KOMORAČA (*Foeniculum vulgare* Mill.) VISOKOG SADRŽAJA *TRANS*-ANETOLA

Etarsko ulje ploda komorača (Foeniculim vulgare Mill.) izolovano je iz samlevenog biljnog materijala postupkom intenzivne mikrotalasne hidrodestilacije. Ovim postupkom izolovano ulje, visokog sadžaja trans-anetola i manjeg sadržaja estragola, dobijeno je nakon samo 10 minuta i u prinosu većem za 30% u odnosu na prinos ulja dobijeno postupkom konvencionalne hidrodestilacije. Pored značajnih razlika u hemijskom sastavu, ulje dobijeno mikrotalasnom hidrodestilacijom pokazalo je snažniju antibakterijsku aktivnost od ulja dobijenog konvencionalnom hidrodestilacijom, dok je antikandidijalna aktivnost ostala nepromenjena. Postupkom intenzivne mikrotalasne hidrodestilacije zabeležena je oko 18 puta manja potrošnja električne energije, kao i manja emisija CO_2 *u poređenju sa postupkom konvencionalne hidrodestilacije, što ukazuje da je ovaj postupak prihvatljiviji za proizvodnju etarskog ulja na industrijskom nivou. Prema ovim rezultatima, etarsko ulje komorača izolovano postupkom intenzivne mikrotalasne hidrodestilacije se može koristiti u prehrambenoj industriji i pakovanju, za proizvodnju nutraceutika, biofarmaceutika, bioherbicida i kozmetičkih preparata.*

Ključne reči: antimikrobna aktivnost; etarsko ulje; plod komorača; Foeniculi aetheroleum, mlevenje; mikrotalasna hidrodestilacija.

Journal of the
Association of Chemical Engineers of
Serbia, Belgrade, Serbia

Chemical Industry &
Chemical Engineering
CI&CE Quarterly

CI&CEQ Vol. 31 Contents: Issues 1–4 YEAR 2025

No. 1

No. 2

No. 3

No. 4

Journal of the
Association of Chemical Engineers,
Belgrade, Serbia

Chemical Industry &
Chemical Engineering
CI&CEQuarterly

CI&CEQ Vol. 31 Author Index YEAR 2025